

**Calculation of the Forced Response of a Turbine Bladed
Disk with Underplatform Dampers**

BY

EMANUELE GROSSI
B.S., Politecnico di Torino, Turin, Italy, 2014

THESIS

Submitted as partial fulfillment of the requirements
for the degree of Master of Science in Mechanical Engineering
in the Graduate College of the
University of Illinois at Chicago, 2016

Chicago, Illinois

Defense Committee:

Piergiorgio Uslenghi, Chair and Advisor

Ahmed Shabana

Teresa Berruti, Politecnico di Torino

This thesis is dedicated to my family, without whom it would never have been accomplished.

TABLE OF CONTENTS

<u>CHAPTER</u>		<u>PAGE</u>
1	INTRODUCTION.....	1
	1.1 State of the arts	1
	1.2 Cyclic symmetry properties of bladed disks.....	5
	1.3 Blade displacement phase shift.....	7
	1.4 Contact forces phase shift.....	9
	1.5 Bladed disk mode shapes.....	10
2	THE TEST RIG.....	14
	2.1 Static and rotating configurations	14
	2.2 The Octopus test rig.....	14
	2.3 The excitation system.....	16
	2.4 Response measurement system.....	17
	2.5 Presentation of the experimental results.....	18
3	FINITE ELEMENT MODEL OF THE BLADED DISK	23
	3.1 Generation of the CAD model on Solidworks.....	23
	3.2 Generation of the FE model on Ansys Mechanical APDL	24
	3.3 Loads application.....	26
	3.4 Cyclic symmetry properties on Ansys Mechanical APDL.....	26
4	MODAL ANALYSIS OF THE BLADED DISK WITHOUT UNDERPLATFORM DAMPERS	29
	4.1 Block Lanczos mode extraction method	29
	4.2 Cyclic symmetry modal analysis	29
	4.3 Linear vibration of the Octopus bladed disk without UPDs.....	30
	4.4 Graph f-ND of the FE disk model.....	31
5	TUNING THE FE MODEL.....	33
	5.1 The impact hammer test	33
	5.2 The tuning process.....	34

TABLE OF CONTENTS (continued)

<u>CHAPTER</u>		<u>PAGE</u>
	5.3	Comparison of the results before and after tuning 37
6	FINITE ELEMENT MODEL OF THE BLISK WITH CYLINDRICAL UNDERPLATFORM DAMPERS.....	39
	6.1	Modeling of the components in Solidworks..... 39
	6.2	Generation of the FE model..... 41
7	STIFFNESS OF THE DISK WITH 12 NODAL DIAMETERS.....	43
	7.1	The case of a single disk sector with lateral constraints 43
	7.2	Full disk and single constrained disk sector: comparison between their dynamic behavior 46
8	THE OCTOPUS NUMERICAL CODE.....	51
	8.1	General overview of the numerical code 51
	8.2	Input parameters required by Octopus numerical code 52
	8.3	Functioning principle of the numerical code..... 53
9	REDUCTION OF THE FINITE ELEMENT MODEL.....	56
	9.1	The Craig-Bampton method..... 56
	9.2	Reduction of the constrained disk sector..... 56
	9.3	Reduction of the full disk..... 58
10	MODAL ANALYSIS OF THE BLADED DISK WITH GLUED UNDERPLATFORM DAMPERS.....	63
	10.1	Calculation of the natural frequencies in Ansys..... 63
	10.2	Comparison with the experimental natural frequencies 65
11	CONTACT MODEL.....	67
	11.1	Two dimensional tangential relative displacement and variable normal load..... 67
	11.2	Scheme of the contact model 69
	11.3	The three contact conditions 70

TABLE OF CONTENTS (continued)

<u>CHAPTER</u>		<u>PAGE</u>
	11.4	Transition criteria for the contact condition 73
12	ESTIMATION OF THE NORMAL CONTACT STIFFNESS 77	
	12.1	Contact formulas for the calculation of the elastic approach 77
	12.2	Calculation of the normal contact stiffness..... 80
	12.3	Allowable static stress 82
13	FORCED RESPONSE CALCULATION METHOD 84	
	13.1	Bladed disk equilibrium equation 84
	13.2	Underplatform damper equilibrium equation 85
	13.3	Coordinate systems adopted..... 86
	13.4	Damper free body diagram 88
	13.5	Simplified damper equilibrium equation 89
	13.6	Solution method..... 91
	13.7	Jacobian matrix definition..... 92
14	ANALYTICAL CALCULATION OF THE JACOBIAN MATRIX 94	
	14.1	List of symbols used in the chapter..... 94
	14.2	Input of the existing numerical code..... 98
	14.3	Jacobian matrix of the damper..... 100
	14.4	Jacobian matrix of the blade 102
	14.5	Saving in computational time achieved with the implementation of the analytical Jacobian matrices 109
15	COMPARISON BETWEEN NUMERICAL AND EXPERIMENTAL RESULTS 112	
	15.1	Validation of the Octopus numerical code..... 112
16	CONCLUSION 117	
	16.1	Concluding remarks..... 117

TABLE OF CONTENTS (continued)

<u>CHAPTER</u>	<u>PAGE</u>
APPENDICES.....	120
Appendix A.....	121
Appendix B.....	122
Appendix C.....	126
Appendix D.....	127
CITED LITERATURE.....	128
VITA.....	131

LIST OF TABLES

<u>TABLE</u>		<u>PAGE</u>
I.	EXPERIMENTAL NATURAL FREQUENCIES MEASURED FOR NODAL DIAMETER 2-6 WITH AN HAMMER TEST.....	34
II.	COMPARISON BETWEEN EXPERIMENTAL AND NUMERICAL NATURAL FREQUENCIES.....	35
III.	FOUR DIFFERENT LOADING CONDITIONS OF THE DISK SECTOR.....	36
IV.	COMPARISON OF THE NATURAL FREQUENCIES OBTAINED BEFORE AND AFTER TUNING	38
V.	COMPARISON BETWEEN FULL DISK AND SINGLE DISK SECTOR: CASE 1	47
VI.	COMPARISON BETWEEN FULL DISK AND SINGLE DISK SECTOR: CASE 2	48
VII.	COMPARISON BETWEEN FULL DISK AND SINGLE DISK SECTOR: CASE 3	49
VIII.	INPUT PARAMETERS FOR THE OCTOPUS NUMERICAL CODE	52
IX.	COMPARISON BETWEEN NATURAL FREQUENCIES CALCULATED IN ANSYS AND MATLAB: ND=2	60
X.	COMPARISON BETWEEN NATURAL FREQUENCIES CALCULATED IN ANSYS AND MATLAB: ND=3	60
XI.	COMPARISON BETWEEN NATURAL FREQUENCIES CALCULATED IN ANSYS AND MATLAB: ND=4	61
XII.	COMPARISON BETWEEN NATURAL FREQUENCIES CALCULATED IN ANSYS AND MATLAB: ND=5	61
XIII.	COMPARISON BETWEEN NATURAL FREQUENCIES CALCULATED IN ANSYS AND MATLAB: ND=6	62

LIST OF TABLES (continued)

<u>TABLE</u>		<u>PAGE</u>
XIV.	COMPARISON BETWEEN EXPERIMENTAL AND NUMERICAL NATURAL FREQUENCIES IN THE STICK CONDITION	66
XV.	CALCULATION OF THE NORMAL CONTACT FORCES	80
XVI.	COMPARISON BETWEEN MAXIMUM PRESSURE GENERATED AND YIELD LIMIT	83

LIST OF FIGURES

<u>FIGURE</u>		<u>PAGE</u>
1.	Sketch of a rotationally cyclic symmetric structure.....	6
2.	Three contact points of two adjacent blades.....	8
3.	Three contact forces of two adjacent blades.	9
4.	Umbrella mode.....	12
5.	Mode shape for ND=2.	13
6.	The test rig Octopus.....	15
7.	Blade platforms for cylindrical UPDs.....	16
8.	The excitation apparatus.....	17
9.	Laser measurement system.....	18
10.	FRF of the 24 blades when $EO = 2$, $FE = 0.3N$, $F_{centr} = 15kg$, measure 2.	19
11.	FRF of the 24 blades when $EO = 2$, $FE = 0.3N$, $F_{centr} = 15kg$, measure 1.	19
12.	Repeatability for $EO = 2$, $FE = 0.3N$, $F_{centr} = 15kg$	20
13.	FRF of the disk in the free condition and with UPDs for increasing values of the excitation force. $EO = 2$, $F_{centr} = 15kg$ (measure 2).....	21
14.	CAD model of the blisk.	23
15.	FE model divided into sub-volumes.	25
16.	Single disk sector fully meshed.	25
17.	Loads applied to the disk.....	26
18.	Detail of the single disk segment mesh.....	27
19.	ANSYS output for cyclic symmetry status.....	28
20.	Modal analysis results.....	30

LIST OF FIGURES (continued)

<u>FIGURE</u>		<u>PAGE</u>
21.	Experimental graph f-ND for the first modal family.....	31
22.	Graph f-ND of the FE disk model.....	32
23.	Impact hammer test results.	33
24.	Nodes constrained on the tuned model.	37
25.	CAD model of the cylindrical underplatform damper.....	39
26.	Cylindrical damper and blade platforms.....	40
27.	CAD model of the bladed disk with UPDs.	41
28.	Nodes of UPD and blade platform along the contact line.....	42
29.	Single disk sector with lateral constraints.....	43
30.	Disk made of single sectors with lateral fixed constraints.	44
31.	Graph frequency-ND for the case of bladed disk made	45
32.	Damper center of mass.	51
33.	Platform versors.....	53
34.	Block diagram of the Octopus numerical code.	54
35.	Constrained degrees of freedom of the disk sector.....	57
36.	Contact nodes on the right platform.	58
37.	Cyclic symmetry constraints.	59
38.	UPDs glued to the blade platforms.	63
39.	Graph f-ND when the UPDs are glued to the disk.	64
40.	Sticking modal shape with 12 nodal diameters.	65
41.	Forces acting on the damper.....	67
42.	Influence of the damper mass on the system response.....	68

LIST OF FIGURES (continued)

<u>FIGURE</u>		<u>PAGE</u>
43.	Contact model for cylindrical underplatform damper.....	69
44.	Variation of the tangential force T during stick-slip.	71
45.	Stick-Slip transition for 1D case.....	73
46.	Transition criteria from the sticking condition.....	74
47.	Transition criteria from the slipping condition.....	75
48.	Transition criteria from the lift-off condition.....	76
49.	Elastic contact between damper and platform.....	78
50.	Graph elastic approach-contact force.	79
51.	Graphical representation of the normal contact stiffness.	81
52.	UPD coordinate systems.....	86
53.	Forces acting on the damper.....	89
54.	Forces acting on the damper.....	97
55.	UPD coordinate systems.....	97
56.	FRF in the sticking condition calculated with the analytical Jacobian matrices, ND=2.....	110
57.	Comparison between experimental and numerical FRFs; ND = 2, FE = 0.2N, Fcentr = 15kg.....	113
58.	Comparison between experimental and numerical FRFs; ND = 2, FE = 0.3N, Fcentr = 15kg.....	113
59.	Comparison between experimental and numerical FRFs; ND = 2, FE = 0.4N, Fcentr = 15kg.....	114
60.	Comparison between experimental and numerical FRFs; ND = 2, FE = 1N, Fcentr = 15kg.....	114
61.	Comparison between numerical FRFs.	115

LIST OF FIGURES (continued)

<u>FIGURE</u>		<u>PAGE</u>
62.	Application of the half power bandwidth method.	121

LIST OF ABBREVIATIONS

CAD	Computer Aided Design
DOF	Degree Of Freedom
EO	Engine Order
FE	Finite Element
FRF	Frequency Response Function
HBM	Harmonic Balance Method
ND	Nodal Diameter
UPD	Under Platform Damper

SUMMARY

The study of the dynamic behavior of turbine bladed disks is a topic of great importance. The fluid flowing through the vanes generates an excitation force whose frequency depends on the shaft rotational speed. In case of industrial turbines, the shaft can reach speed values of the order of 18000 rpm.

When the excitation frequency equals the natural frequency of the system, the high vibration amplitude generated can lead to high-cycle fatigue failure. In order to damp vibrations, an effective solution consists in introducing, between the blade platforms, small metal masses called underplatform dampers (UPD). Each damper is pressed against the blade platforms by the centrifugal force: when relative motion takes place at the contacts, the friction forces dissipate vibrational energy.

From an industrial point of view, it is fundamental to have effective tools for the design of turbine bladed disks with underplatform dampers. The nonlinear calculation of the bladed disk forced response cannot be computed by the existing commercial finite element codes like Ansys. As a consequence, numerical tools have been developed in MATLAB at Politecnico di Torino.

In principle, bladed disks were designed as if friction contacts were not present and only afterwards the change in the dynamic behavior due to the introduction of UPDs was analyzed. The numerical codes have then been optimized in order to take into account the presence of UPDs from the beginning of the design stage.

SUMMARY (continued)

A first version of a numerical code was developed on MATLAB at Politecnico di Torino to calculate the forced response of the *Octopus* bladed disk equipped with cylindrical underplatform dampers. The *Octopus* test rig consists of a static blisk with removable blade platforms which allow the introduction of UPDs of different geometry. A non-contact travelling excitation, produced by a set of electromagnets, simulates different engine orders.

In order to validate numerical codes, it is necessary to compare numerical results with experimental values. In 2011 an experimental study was carried out at the LAQ AERMEC laboratory of *Politecnico di Torino* on the *Octopus* test rig.

The aim of this thesis is threefold:

1. The numerical code was developed by considering only a single sector of the disk, constrained at its two lateral interfaces. This method neglected the disk compliance and allowed to take into account only the blades dynamic. A procedure was developed to allow extracting from Ansys the mass and stiffness matrices of the disk FE model in cyclic symmetry. As a consequence, it will be possible to examine the whole dynamic of the bladed disk.

SUMMARY (continued)

2. The code must be enhanced in order to calculate the forced response in a reasonable computational time. This improvement is fundamental because, once the numerical code is validated, it can be used to test underplatform dampers design. Using the analytical calculation of the Jacobian matrices for both the blades and the underplatform dampers, the computational time can be dramatically reduced.
3. The numerical code is validated by comparing the numerical and experimental results.

1 INTRODUCTION

1.1 State of the arts

There is more than 20 years of history of analysis and prediction of the dynamic behavior of turbine bladed disks. Many different friction devices have been designed to reduce blades vibration amplitude.

Jaiswal and Bhave (1994) experimentally tested on a rotating bladed disk different damping mechanisms, namely lacing wires, damping pins and damping wires. The latter turned out to be the most performant.

Cardona et al. (1994) presented a new approach, completely analytical, for the calculation of the Jacobian matrix of nonlinear algebraic problems. This method allows to solve nonlinear algebraic problems with high efficiency; it will be applied by Petrov and Ewins in 2003 to study the nonlinear forced response of bladed disks with underplatform dampers.

Yang and Menq (1998) presented a 3-dimensional friction contact model for the prediction of the frequency response of systems characterized by 3-dimensional frictional constraints. The relative motion between the surfaces of the two bodies is decomposed in a 2-dimensional in-plane tangential motion to take into account stick-slip transition and in a normal relative motion that, in an extreme condition, can lead to the damper lift off.

Berruti et al. (2002) developed a test rig for the vibration analysis of turbine bladed segments. Experimental results proved the ability of the test rig to reproduce and measure the behavior of this type of bladed assembly.

Jones and Cross (2003) developed a travelling wave excitation system for stationary bladed disks of different sizes and number of blades.

Petrov and Ewins (2003, p.371) developed a methodology aimed at the “analytical derivation of the force vector and stiffness matrix of a friction interface element [...] for the case of multi-harmonic vibration analysis”. As a result, the iteration process required for the calculation of the nonlinear response of bladed disks can converge faster without any loss of accuracy and stability.

Panning et al. (2004) investigated cylindrical and asymmetrical underplatform dampers: they compared results obtained with rotating gas turbines in the real working condition with the predictions resulted from their numerical model.

Berruti et al. (2005) tested an asymmetric underplatform damper in a test rig made of two adjacent real blades. As a result of a comparison of experimental and numerical results, it was proven that the damper model was accurate in predicting the blade response for out-of-phase blade modes.

Castanier and Pierre (2006) examined the literature on bladed disks vibration, “with an emphasis on key developments in the last decade that have enabled better prediction and understanding of the forced response of mistuned bladed disks” (Castanier and Pierre, 2006, p.384).

Zucca et al. (2006) described a method for the calculation of the forced response of bladed disks equipped with underplatform dampers. The disk finite element model is reduced through Component Mode Synthesis and the nodes degrees of freedom located at the interfaces are reduced introducing interface modes. The contact elements adopted in the code allow both tangential and normal relative displacements. Numerical calculations are carried out in order to assess the efficiency of the reduced model as well as of the underplatform damper model.

Borrajo et al. (2006) developed a numerical code for the calculation of the forced response of a bladed disk with wedge dampers. In particular, by using classical numerical finite difference schemes the calculation of the system Jacobian matrix requires a prohibitive computational time. For this reason, they applied a method that is completely analytical.

Koh and Griffin (2007) built a model to predict the behavior of friction dampers with spherical contacts. They found out that by using elasticity theory and contact mechanics, it is possible to predict with good accuracy the damper performance.

Petrov and Ewins (2007) developed structural dynamic models for dampers of different shape, namely “wedge” and “split” underplatform dampers. These new models were validated through numerical investigations of bladed disks.

Szwedowicz et al. (2008) presented numerical predictions of the forced response of shrouded turbine blades. They also studied the damping effectiveness of different shrouds configurations: slant shroud coupling turned out to be performant than zigzag coupling.

Sever et al. (2008) studied the forced response of a rotating bladed disk with “cottage-roof” dampers and validated reasonably well their numerical predictions.

Cigeroglu et al. (2009) developed a method to predict the forced response of a bladed disk coupled with friction dampers. In particular, numerical predictions were compared with experimental data for the case of a disk with wedge dampers and the results were in good agreement.

Baraa et al. (2011) analyzed the physical origin of the energy dissipation induced by underplatform dampers in turbomachines. According to the most common theory, vibrational energy is reduced because it is converted in heat resulting from relative motion between the bodies in contact. As a result of the study of a representative single degree of freedom system, they identified as main player for the peak flattening of the frequency response the change in boundary conditions due to stick-slip.

Firrone et al. (2011) proposed a new method for the calculation of the forced response of bladed disks with underplatform dampers. In particular, the static and dynamic equations of the system are coupled making unnecessary the preliminary static analysis at the contacts: the static loads are derived from the static relative displacements.

Berruti et al. (2011) presented the static test rig *Octopus*, developed at Politecnico di Torino, which allows to validate numerical models aimed at the calculation of the forced response of a blisk with underplatform dampers. In particular, a system was designed in order to generate a travelling wave under the blades and simulate different engine order excitations. Some experimental tests were eventually carried out to

calculate the frequency response function of the bladed disk with underplatform dampers.

1.2 Cyclic symmetry properties of bladed disks

Bladed disks can be considered either as a one single component or as a structure made of cyclically symmetric sectors. The second approach is computationally more efficient but more complicated to implement, because everything must be transformed to a system based on a single sector. Orris and Petit (1974), discussed wave propagation in periodic structures, i.e. structures containing a series of identical structural elements. What they found out is that the ratio between analogous nodal displacements in adjacent structures is equal to e^μ . The parameter μ is a complex propagation constant defined as

$$\mu = a + i\varphi \quad (1.2.1)$$

where a is the real part, called “attenuation constant”, φ is the imaginary part, called “interblade phase angle”. Hence, the nodal displacement on the right-hand boundary is related to the left one by

$$u_{right} = e^\mu \cdot u_{left} \quad (1.2.2)$$

Similarly, for the equilibrium between adjacent elements, the nodal forces and moments are related by

$$F_{right} = e^\mu \cdot F_{left} \quad (1.2.3)$$

Thomas (1974) and (1979), analyzed the particular case of cyclic symmetric structures, periodical structures made of a finite number N of identical sectors forming a closed ring (see Figure 1).

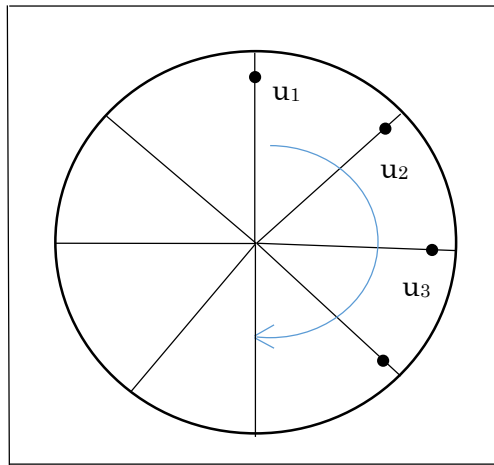


Figure 1. Sketch of a rotationally cyclic symmetric structure.

From equation (1.2.2) it follows that

$$u_2 = u_1 e^{\mu} \quad (1.2.4)$$

$$u_3 = u_2 e^{\mu} \quad (1.2.5)$$

hence

$$u_3 = u_1 e^{2\mu} \quad (1.2.6)$$

The general formula is

$$u_j = u_1 e^{(j-1)\mu} \quad (1.2.7)$$

In case of cyclic symmetry, the N^{th} sector is adjacent to the first one, consequently

$$u_{N+1} = u_1 e^{N\mu} = u_1 \quad (1.2.8)$$

hence

$$e^{N\mu} = e^{N(a+i\varphi)} = e^{Na+i2\pi} = 1 \rightarrow a = 0 \quad (1.2.9)$$

Therefore the real part of the propagation constant is null; (1.2.2) and (1.2.3) can be rewritten as

$$u_{right} = e^{i\varphi} \cdot u_{left} \quad (1.2.10)$$

$$F_{right} = e^{i\varphi} \cdot F_{left} \quad (1.2.11)$$

1.3 Blade displacement phase shift

Figure 2 shows three contact points belonging to two adjacent turbine blades with a cylindrical underplatform damper between them.

In particular, \mathbf{u}^* is the vector of components of the displacement of a platform contact point. It can be expressed as

$$\mathbf{u}^* = \begin{Bmatrix} \mathbf{u}^{*Real} \\ \mathbf{u}^{*Imag} \end{Bmatrix} = \begin{Bmatrix} u^{*Real} \\ v^{*Real} \\ w^{*Real} \\ u^{*Imag} \\ v^{*Imag} \\ w^{*Imag} \end{Bmatrix}_p \quad (1.3.1)$$

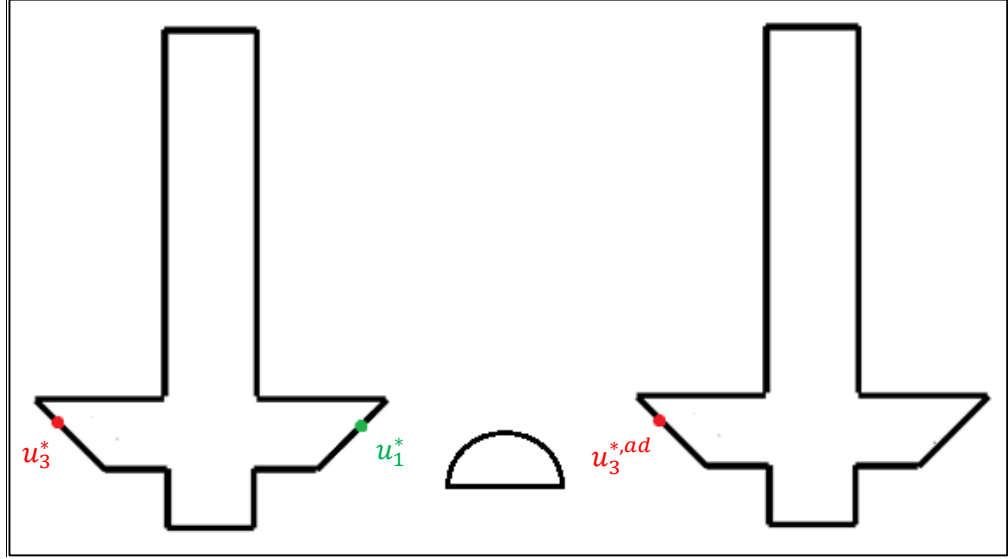


Figure 2. Three contact points of two adjacent blades.

The displacements \mathbf{u}_3^* and $\mathbf{u}_3^{*,ad}$ are linked through the phase shift φ existing between the adjacent sectors

$$\mathbf{u}_3^{*,ad} = \mathbf{u}_3^{*,ad,Real} + i\mathbf{u}_3^{*,ad,Im} \quad (1.3.2)$$

$$\mathbf{u}_3^{*,ad} = (\mathbf{u}_3^{*Real} + i\mathbf{u}_3^{*Im})e^{i\varphi} \quad (1.3.3)$$

$$\mathbf{u}_3^{*,ad} = \mathbf{u}_3^{*Real} \cos(\varphi) + i\mathbf{u}_3^{*Real} \sin(\varphi) + i\mathbf{u}_3^{*Im} \cos(\varphi) - \mathbf{u}_3^{*Im} \sin(\varphi) \quad (1.3.4)$$

The general relationship linking the displacements of two adjacent blades is

$$\mathbf{u}^{*,ad} = \phi \mathbf{u}^* \quad (1.3.5)$$

where ϕ is the phase shift matrix. It is a square matrix of dimension $N_{CP} \times 3 \times 2$.

1.4 Contact forces phase shift

As far as the contact forces are concerned, Figure 3 shows an exemplifying scheme of three forces developed at the contact nodes of two adjacent blades.

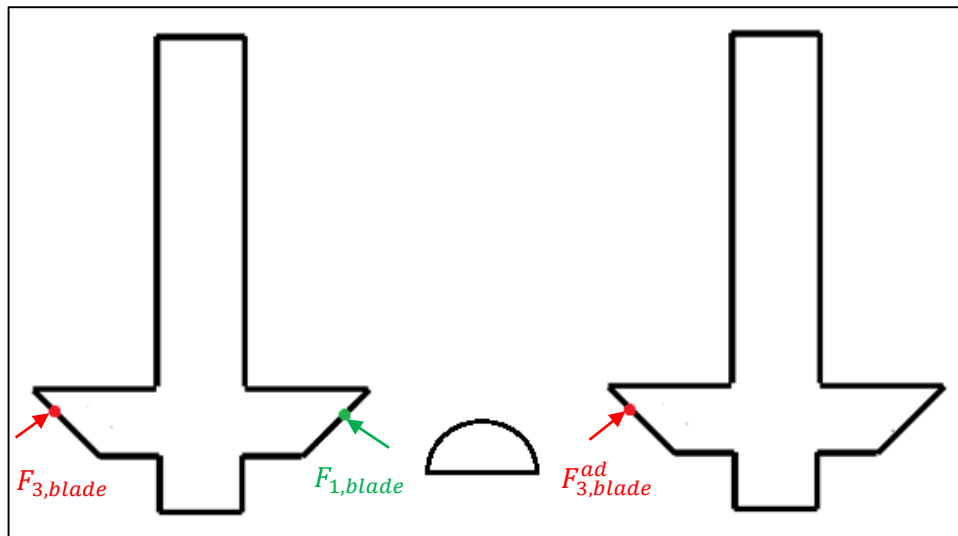


Figure 3. Three contact forces of two adjacent blades.

In particular, \mathbf{F}_{blade} is the vector of components of the contact force acting on the blade at a given contact point.

$$\mathbf{F}_{blade} = \begin{Bmatrix} \mathbf{F}_{blade}^R \\ \mathbf{F}_{blade}^{Im} \end{Bmatrix} = \begin{Bmatrix} F_{U,blade}^R \\ F_{V,blade}^R \\ F_{W,blade}^R \\ F_{U,blade}^{Im} \\ F_{V,blade}^{Im} \\ F_{W,blade}^{Im} \end{Bmatrix}_p \quad (1.4.1)$$

Forces $\mathbf{F}_{3,blade}$ and $\mathbf{F}_{3,blade}^{ad}$ are linked through the phase shift φ , namely

$$\mathbf{F}_{3,blade} = \mathbf{F}_{3,blade}^{Real} + i\mathbf{F}_{3,blade}^{Im} \quad (1.4.2)$$

$$\mathbf{F}_{3,blade} = (\mathbf{F}_{3,blade}^{ad,Real} + i\mathbf{F}_{3,blade}^{ad,Im})e^{-i\varphi} \quad (1.4.3)$$

$$\begin{aligned} \mathbf{F}_{3,blade} = & \mathbf{F}_{3,blade}^{ad,Real} \cos(\varphi) - i\mathbf{F}_{3,blade}^{ad,Real} \sin(\varphi) + i\mathbf{F}_{3,blade}^{ad,Im} \cos(\varphi) \\ & + \mathbf{F}_{3,blade}^{ad,Im} \sin(\varphi) \end{aligned} \quad (1.4.4)$$

Consequently, the general relationship between the contact forces developed on two adjacent blades is

$$\mathbf{F}_{blade} = \phi^T \mathbf{F}_{blade}^{ad} \quad (1.4.5)$$

where ϕ^T is the phase shift matrix, transposed.

1.5 Bladed disk mode shapes

A turbine bladed disk has many natural frequencies and related mode shapes. The main feature of disks mode shapes is the presence of lines of zero out-of-plane displacement, called nodal diameters (Hassan, 2008). The number of nodal diameters n is related to the number of sectors/blades N by

$$0 \leq n \leq \frac{N}{2} \text{ if } N \text{ is even} \quad (1.5.1)$$

$$0 \leq n \leq \frac{N-1}{2} \text{ if } N \text{ is odd} \quad (1.5.2)$$

The interblade phase angle φ can be expressed as a function of the number of nodal diameters or as a function the engine order (EO) value:

$$\varphi_n = \frac{2\pi}{N} \cdot n \quad (1.5.3)$$

or

$$\varphi_{EO} = \frac{2\pi}{N} \cdot EO \quad (1.5.4)$$

where the engine order EO can be defined as the number of times each blade is excited for each complete rotation of the disk. In particular, the excitation frequency ω is related to the disk rotational speed Ω through the EO as

$$\omega = EO \cdot \Omega \quad (1.5.5)$$

By comparing (1.5.3) and (1.5.4) it is evident that the value of EO excitation is equal to the number of the nodal diameters present in the structure.

If n is either 0 or $\frac{N}{2}$ the vibration mode is stationary and the solution is real. In particular, if $n = 0$ then $\varphi = 0$ hence all the blades oscillate with the same amplitude in phase (see Figure 4).

If $n = \frac{N}{2}$ then $\varphi = \pi$, hence all the blades oscillate with the same amplitude but out of phase.

In all the other cases the solution is complex (the term $i \cdot \sin(\varphi) \neq 0$) and the vibration mode is rotating. In detail, two orthogonal modes (null scalar product) correspond to each natural frequency value.

The reason of this double solution (the two complex modes are conjugate) is that at a given frequency, the mode shape can be rotated by any angle (Seinturier, 2007a).

Figure 5 shows the mode shape when two nodal diameters are present.

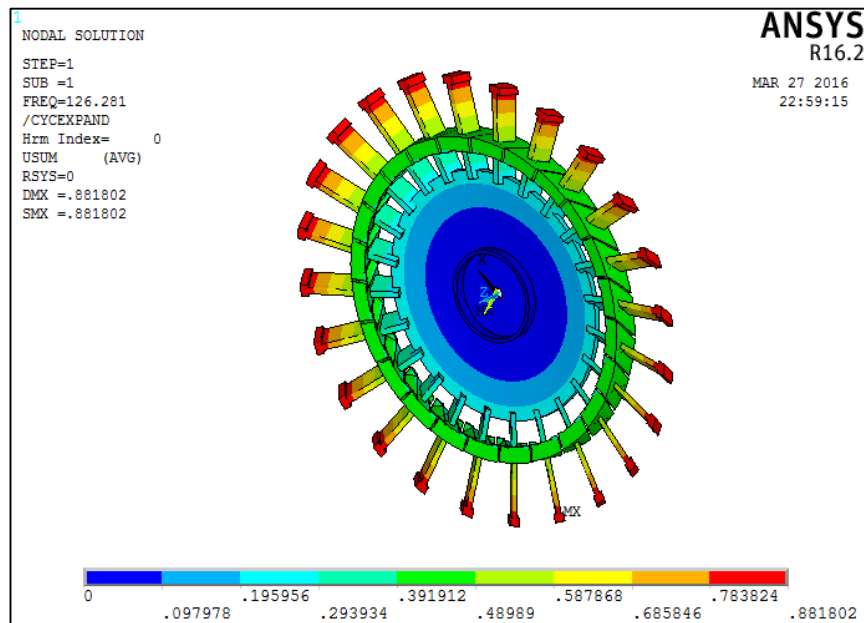


Figure 4. Umbrella mode.

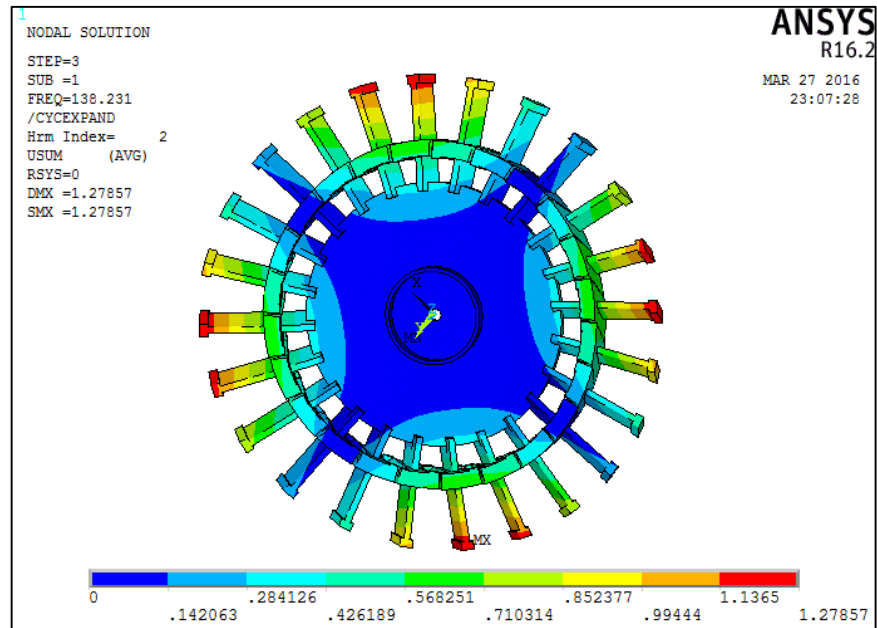


Figure 5. Mode shape for ND=2.

2 THE TEST RIG

2.1 Static and rotating configurations

An experimental test rig is of fundamental importance for the accurate measurement of the forced response of a turbine bladed disk with underplatform dampers. It is possible to make a distinction between two main types of test rigs: in the first case the disk rotates and the excitation source is fixed, in the second case the rotor is static and the excitation travels (Firrone and Berruti, 2012a).

For the case study considered in this thesis, a static test rig was used. Its main advantage is making the measurement activity easier thanks to a controlled excitation system and to the suppression of aerodynamic effects. Experimental data for the test case here studied were gathered from the test rig *Octopus*, which is located at Politecnico di Torino in the AERMEC laboratory.

2.2 The Octopus test rig

By looking at Figure 6, the integral bladed disk (1), also called blisk, consists of 24 blades. It is connected to a big inertial mass (2) of about 400kg by means of a cap closed by seven screws. The arm structures (3) present one pulley each, they are mounted on the external ring (4) equally spaced around the circumferential disk direction. The simulation of the centrifugal force on each underplatform damper is

obtained by keeping them in contact against the blade platforms by means of two wires (5), which pass over the arm and are connected through the pulley to a dead weight (6). Each pulley is coupled to a low friction ball bearing. The arms can be properly rotated in order to align the underplatform dampers wires along the centrifugal force radial direction (Berruti et al., 2011a). The “Octopus” test rig allows the investigation of different contact geometries thanks to the presence of removable blade platforms. The ones used for the case of cylindrical underplatform dampers are shown in Figure 7 (Berruti, 2011).

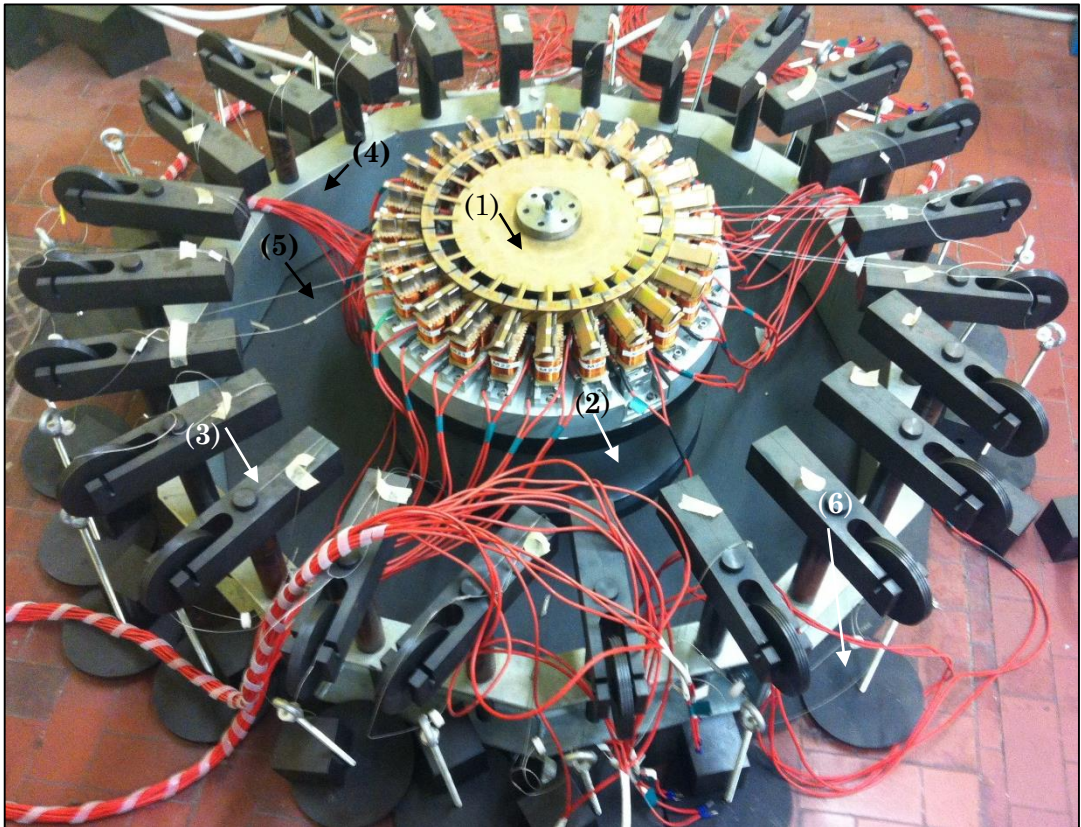


Figure 6. The test rig Octopus.

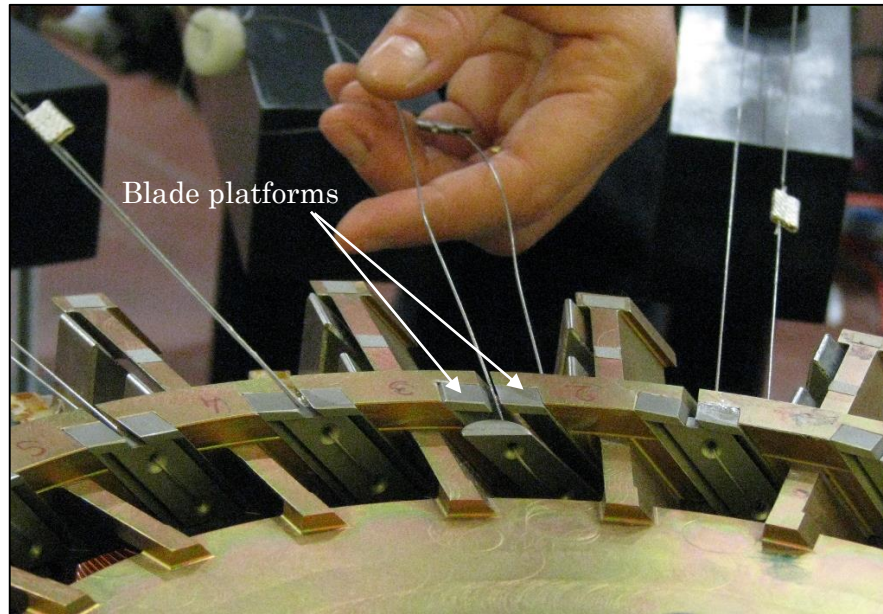


Figure 7. Blade platforms for cylindrical UPDs.

2.3 The excitation system

The excitation system for a static test rig can be either contacting or non-contacting. A control system has to be developed “in order to activate the exciters with a given phase shift in time to mimic the engine order force pattern.” (Firrone and Berruti, 2012b, p.80).

In the *Octopus* test rig, the non-contact travelling wave is generated by electromagnets located below each blade: the magnetic induction flux flows through the air gap and eventually reaches the blades (Firrone and Berruti, 2012c). In Figure 8 it is shown that each electromagnet (1) is mounted on an aluminum circular plate (2). This material does not interfere with the magnetic flux generated (Berruti et al., 2011b).

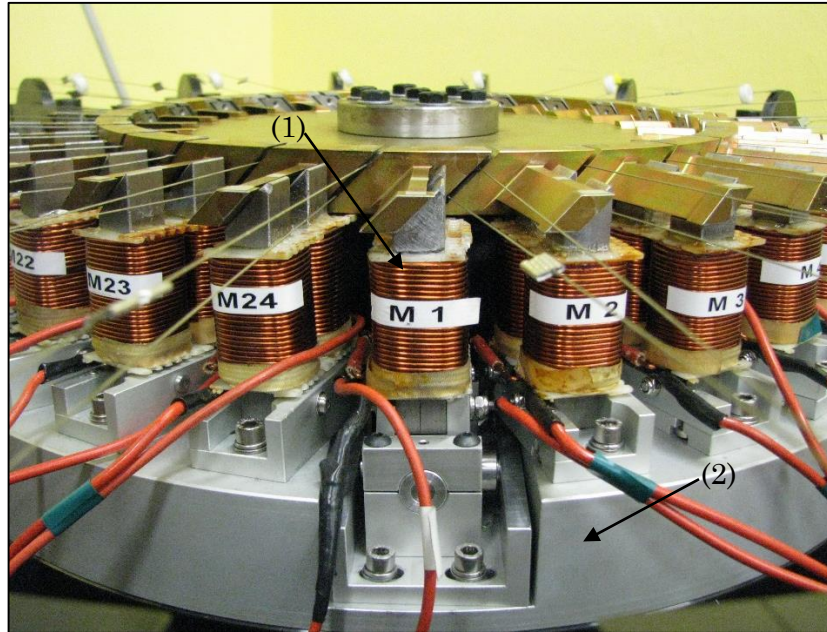


Figure 8. The excitation apparatus.

2.4 Response measurement system

Once the electromagnets are activated so as to generate a given engine order excitation, the dynamic response of the disk must be measured.

For the test rig *Octopus*, the measurements is carried out by means of a laser scanning vibrometer (see Figure 9). In detail, a special mirror built for laser applications located above the disk “reflects the laser beam along the perpendicular direction to the disk plane in order to detect the vibration component in the out-of-plane direction.” (Berruti et al., 2011c, p. 2-3). The number of points measured in the rotor plane is previously defined (Firrone and Berruti, 2012d).

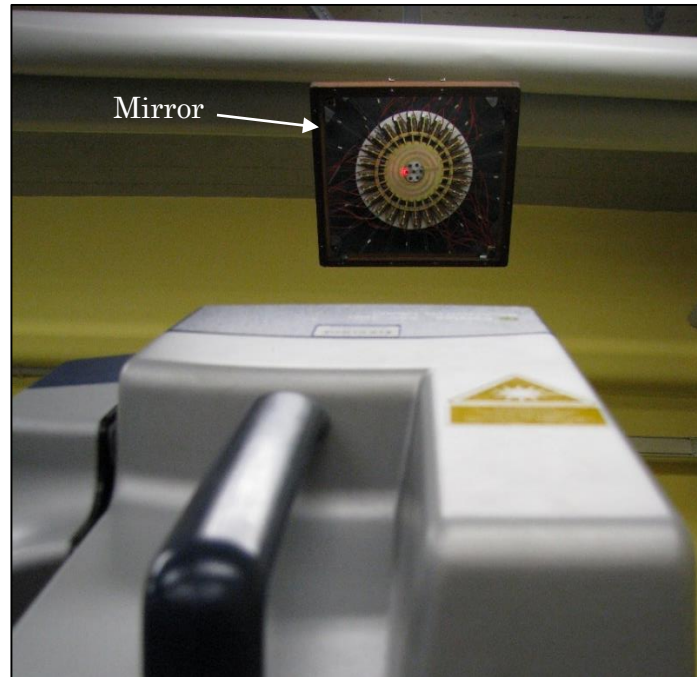


Figure 9. Laser measurement system.

2.5 Presentation of the experimental results

For a given engine order (EO), excitation force (F_E) and centrifugal force (F_{centr}) applied by the dead weights, the velocity of one point per blade along the disk axial direction is measured. The velocity values are normalized by the excitation force F_E . As an example, Figure 10 and Figure 11 show the FRFs of the 24 blades excited by $EO=2$, $F_E=0.3N$ and $F_{centr}=15kg$ in case of two different measurements.

Due to the presence of small mistuning, i.e. small variations between each sector, there is a difference between the FRFs of each blade (Castanier and Pierre, 2006a). The envelope of the maxima of the FRFs at every frequency is represented by the bold red and blue lines (Firrone and Berruti, 2012e), (Firrone et al., 2013).

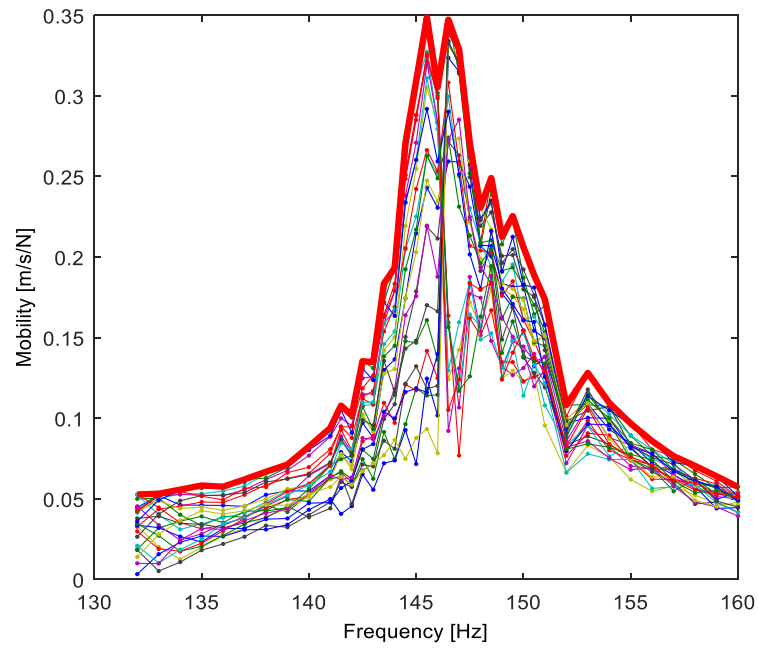


Figure 10. FRF of the 24 blades when $EO = 2$, $F_E = 0.3N$, $F_{centr} = 15kg$, measure 2.

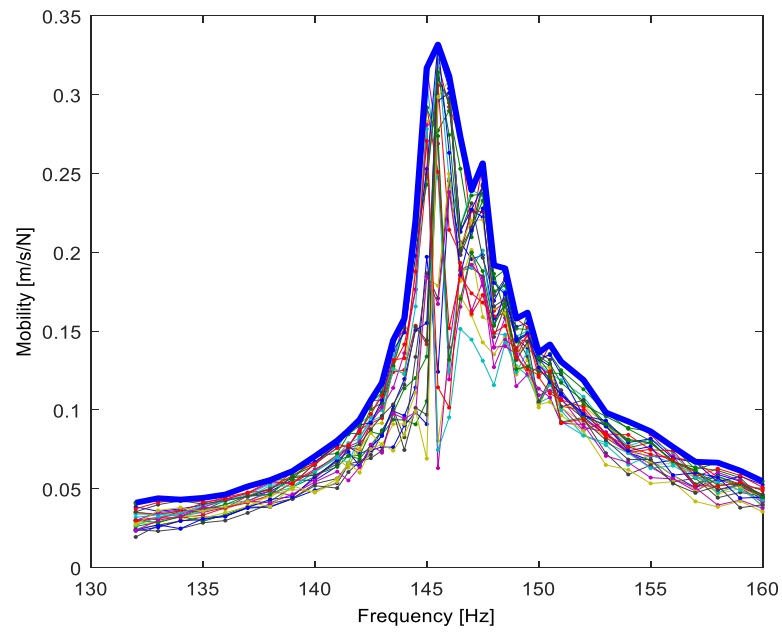


Figure 11. FRF of the 24 blades when $EO = 2$, $F_E = 0.3N$, $F_{centr} = 15kg$, measure 1.

Since the numerical code *Octopus* (see Chapter 8) developed to predict the nonlinear forced response of the disk does not take mistuning into account, the envelope of the maxima (which is the worst case working condition) is taken as a reference.

In order to analyze the repeatability of the results, two measurements were carried out keeping the same values of EO , centrifugal force and excitation force. The two envelopes corresponding to the first and second measurement in case of $EO = 2$, $F_E = 0.3N$, $F_{centr} = 15kg$ are shown in Figure 12. It is evident that the behavior of the UPDs is slightly different in the two cases.

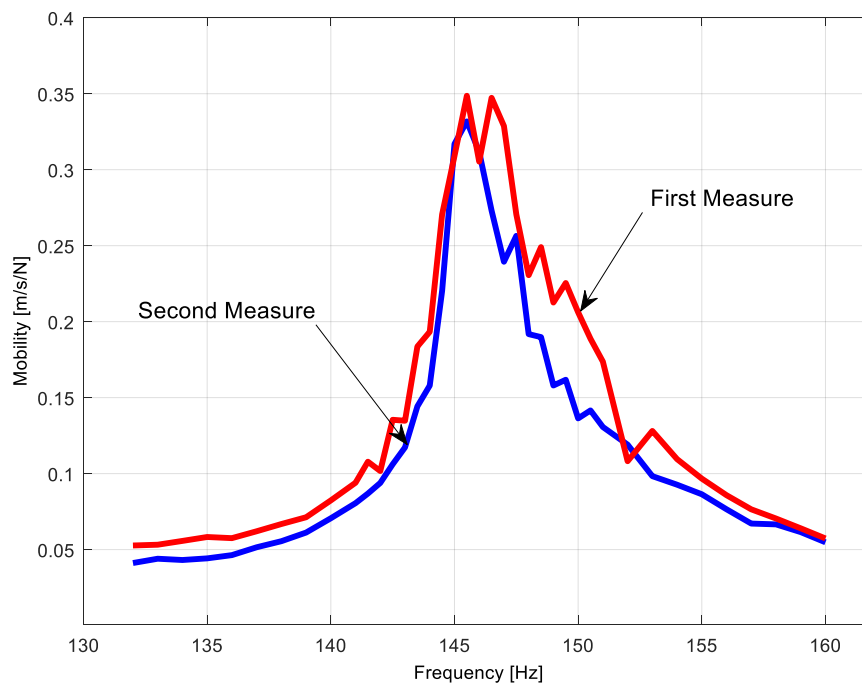


Figure 12. Repeatability for $EO = 2$, $F_E = 0.3N$, $F_{centr} = 15kg$.

By keeping the same values of EO and centrifugal force, the excitation force F_E is progressively increased. As an example, in case of $EO=2$ and $F_{centr}=15kg$, the envelopes obtained are plotted in Figure 13 (measure 2).

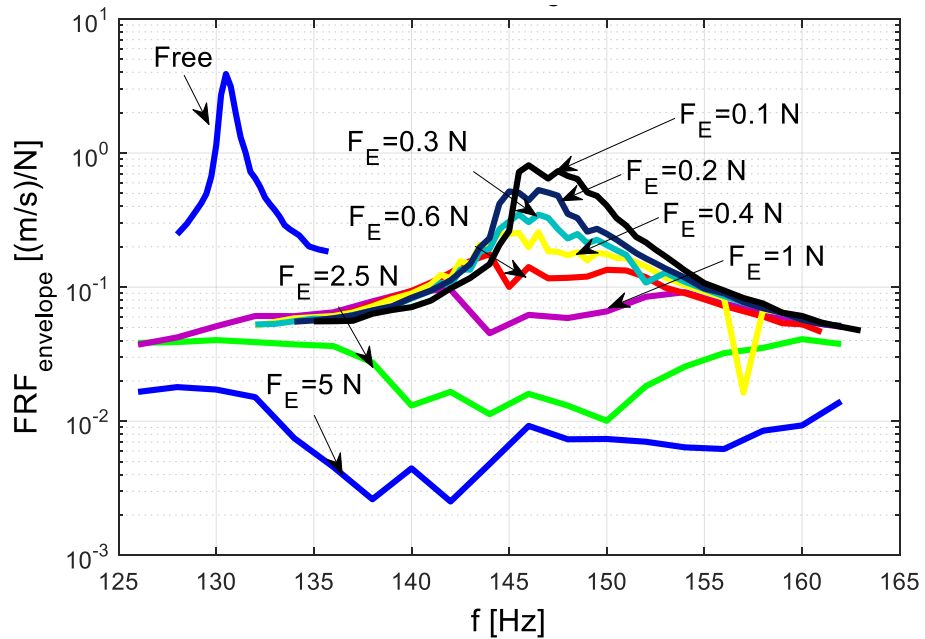


Figure 13. FRF of the disk in the free condition and with UPDs for increasing values of the excitation force. $EO = 2$, $F_{centr} = 15kg$ (measure 2).

It is evident that the amount of damping increases with the excitation force. When F_E is low ($F_E=0.1N-0.2N-0.3N$) the relative displacement between UPDs and platforms is not high enough to produce significant friction forces at the contacts.

At the same time the UPDs act as additional constraints and determine a stiffening of the system (higher resonance frequency). When F_E increases, the relative displacement at the contacts induces friction forces that dissipate more vibrational energy. The resonance frequency decreases because, being the damper mobility increased, the bladed disk stiffness decreases (Firrone and Berruti, 2012e).

3 FINITE ELEMENT MODEL OF THE BLADED DISK

3.1 Generation of the CAD model on Solidworks

By approximating the turbine bladed disk with a finite element model, it is possible to obtain a reduction in the number of degrees of freedom, which are infinite in case of a continuous structure. The first step to accomplish for the generation of the finite element model is the creation of a 3-D CAD model on Solidworks, as shown in Figure 14.

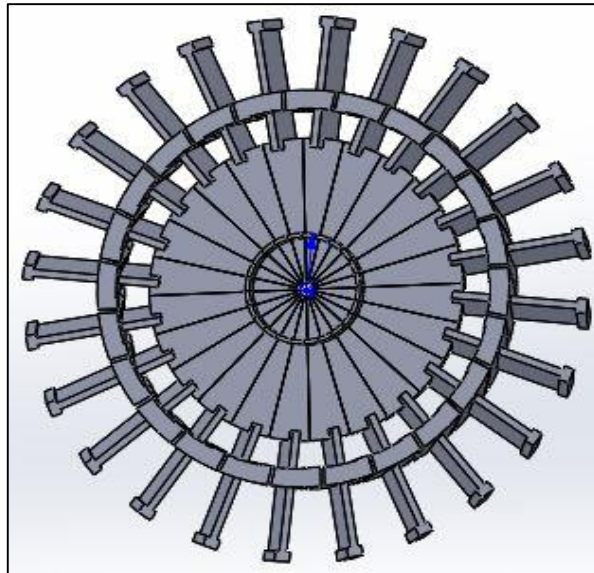


Figure 14. CAD model of the blisk.

3.2 Generation of the FE model on Ansys Mechanical APDL

The CAD model can be subsequently imported in Ansys Mechanical APDL in the Parasolid format. As far as the geometry is concerned, SOLID186 elements were selected: they are elements defined by 20 nodes with 3 DOFs each: translation in the nodal x, y and z directions (Ansys Inc., p.594-596, 2013).

The procedure was carried out for a single sector of the disk (one blade plus the correspondent disk segment) because Ansys allows the generation of a cyclical symmetric structure by replicating a single sector around a previously defined rotation axis. The main advantage of the cyclic symmetry Ansys feature is the saving in CPU time.

After the definition of the material properties, the structure was divided into sub-volumes (see Figure 15) in order to prepare the most favorable conditions for the mapped brick mesh, which is more elegant, homogeneous and guarantees a reduction of the computational time in the subsequent analyses. Unfortunately, depending on the geometry taken into account, it is not always possible to obtain sub-volumes eligible for a regular mapped mesh. As an example, when the volume is characterized by the presence of sharp edges, the tetrahedral free mesh is the most efficient solution. Given the geometry of the bladed disk, it was possible to obtain the mapped brick mesh for the whole structure, with the exception of a small portion of volume of the blade platform, subsequently covered with a tetrahedral mesh (see Figure 16).

The next steps consist in the introduction of external constraints acting as loads on the structure and on the application of the cyclic symmetry properties to the disk sector.

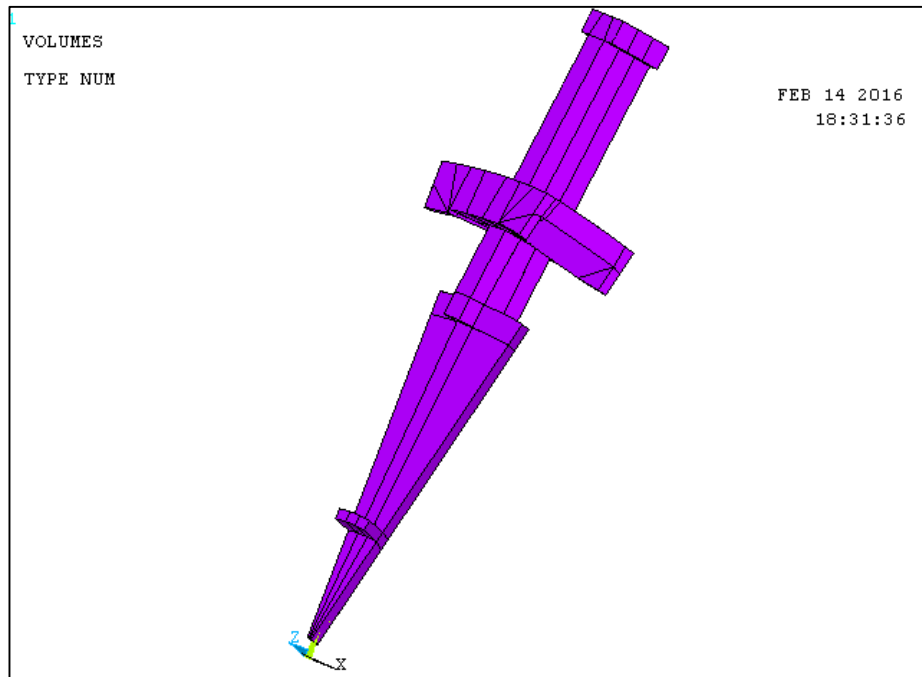


Figure 15. FE model divided into sub-volumes.

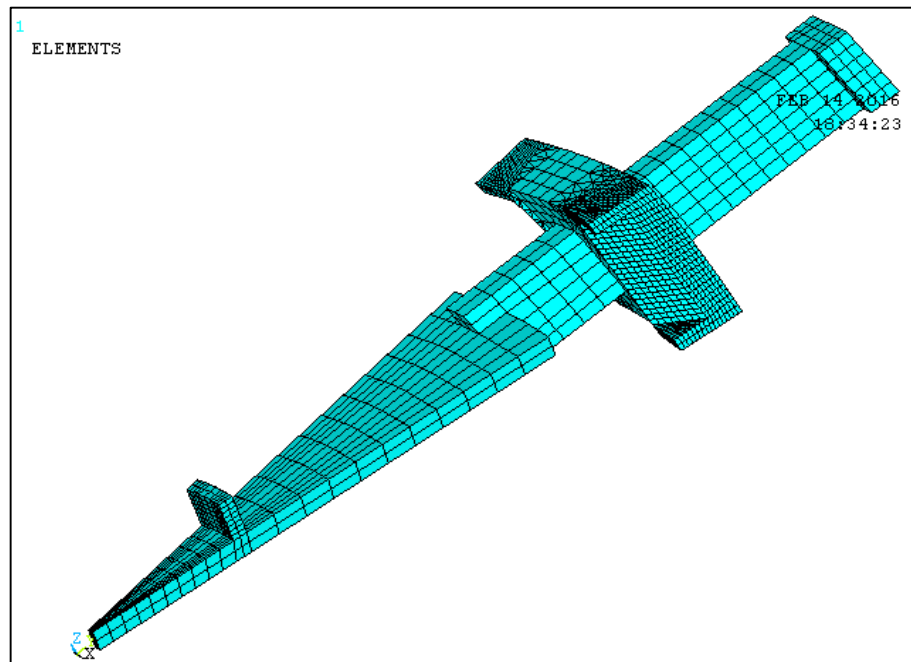


Figure 16. Single disk sector fully meshed.

3.3 Loads application

After the meshing operation, loads were introduced taking into account the actual working condition of the disk: Figure 17 shows that all DOFs were set to a value of zero displacement in the region where the disk is constrained to the central fixture.

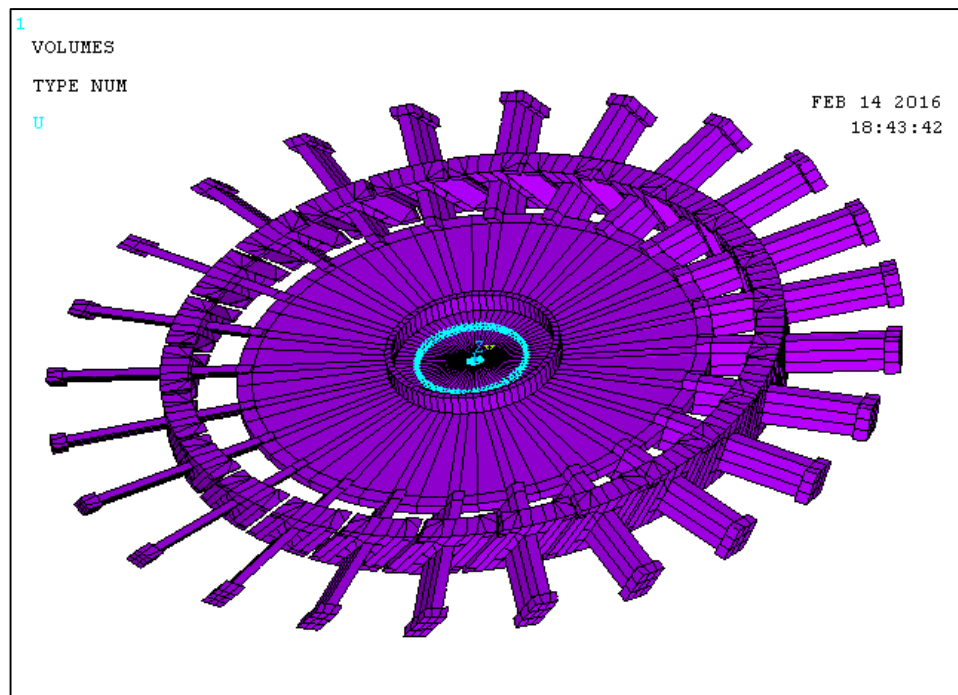


Figure 17. Loads applied to the disk.

3.4 Cyclic symmetry properties on Ansys Mechanical APDL

For the bladed disk taken into account in this thesis, since each sector counts for 15 degrees, 24 replications are required to complete the full disk. The application of the

cyclic symmetry properties in Ansys Mechanical APDL requires the mesh of the disk sector to respect one main feature: the two lateral faces of the single disk segment must be meshed so that, once the sector is replicated, each node on the left face finds the correspondent node on the right face. Figure 18 shows a detail of the lateral mesh of the single disk sector.

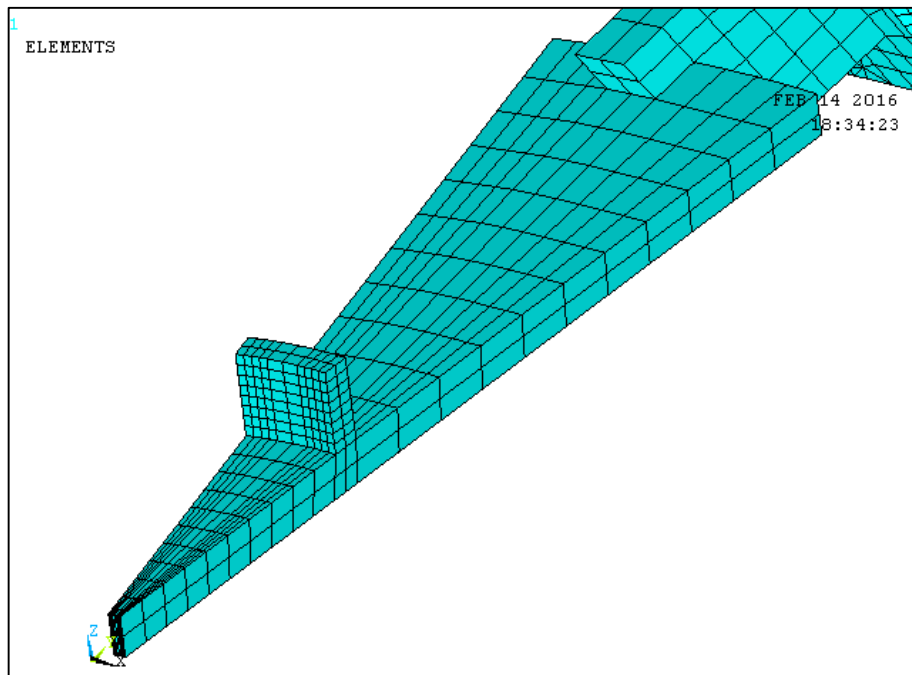


Figure 18. Detail of the single disk segment mesh.

If all the boundary conditions have been applied successfully, Ansys indicates that all sectors have been matched with each other, as shown in Figure 19.

```
LIST CYCLIC SYMMETRY STATUS
*****
***** CYCLIC SYMMETRY STORED QUANTITIES *****
*****
* NUMBER OF SECTORS =                24      *
* SECTOR ANGLE =                   15.000    *
* CYCLIC COORDINATE SYSTEM =          1      *
* COMPONENT NAME ROOT = CYCLIC            *
* LOW EDGE COMPONENT = CYCLIC_M01L      MATCHED *
* HIGH EDGE COMPONENT = CYCLIC_M01H      *
* DUPLICATE SECTOR NOT DEFINED          *
*****
```

Figure 19. ANSYS output for cyclic symmetry status.

4 MODAL ANALYSIS OF THE BLADED DISK WITHOUT UNDERPLATFORM DAMPERS

4.1 Block Lanczos mode extraction method

The finite element model is the starting point of the modal analysis. The mode extraction method chosen in Ansys Mechanical APDL was Block Lanczos, which is available for large symmetric eigenvalue problems. The block shifted Lanczos algorithm is a variation of the classical Lanczos algorithm, in which the iterations are done by means of a block of vectors (ANSYS Inc., p.765, 2013).

4.2 Cyclic symmetry modal analysis

The cyclic symmetry analysis options allow to define the first and the last values of the harmonic indexes to study: with N the number of disk blades, up to $\frac{N}{2}$ nodal diameters can be present in the structure (if N is even). For particular applications it is also possible to analyze only a previously defined range of frequency values. The amount of time required by Ansys to perform the calculation depends on the complexity of the structure in terms of mesh and geometry. When the analysis is completed, a list of frequency values for each harmonic index is shown as output (see Figure 20).

***** INDEX OF DATA SETS ON RESULTS FILE *****						
SET	TIME/FREQ	LOAD STEP	SUBSTEP	CUMULATIVE	HRM-INDEX	
21	124.67	2	1	21	1	
22	124.67	2	2	22	1	
1	126.28	1	1	1	0	
41	138.23	3	1	41	2	
42	138.23	3	2	42	2	
61	180.23	4	1	61	3	
62	180.23	4	2	62	3	
81	218.17	5	1	81	4	
82	218.17	5	2	82	4	
101	240.21	6	1	101	5	
102	240.21	6	2	102	5	
121	252.34	7	1	121	6	
122	252.34	7	2	122	6	
141	259.39	8	1	141	7	
142	259.39	8	2	142	7	
161	263.72	9	1	161	8	
162	263.72	9	2	162	8	
181	266.43	10	1	181	9	
182	266.43	10	2	182	9	

Figure 20. Modal analysis results.

4.3 Linear vibration of the Octopus bladed disk without UPDs

The linear vibration of a bladed disk without underplatform dampers has an important feature: “each system mode shape consists of identical motion in each sector except for a fixed sector-to-sector phase difference, which is called an interblade phase angle for bladed disks” (Castanier and Pierre, 2006b, p.385). Each mode shape features a certain number of nodal diameters that influence the stiffness of the system.

A significant graph frequently used to describe the behavior of bladed disks plots the natural frequencies as a function of the number of nodal diameters. The experimental graph, whose data were gathered only for the first modal family and for a number of nodal diameters that goes from 1 to 6, is shown in Figure 21.

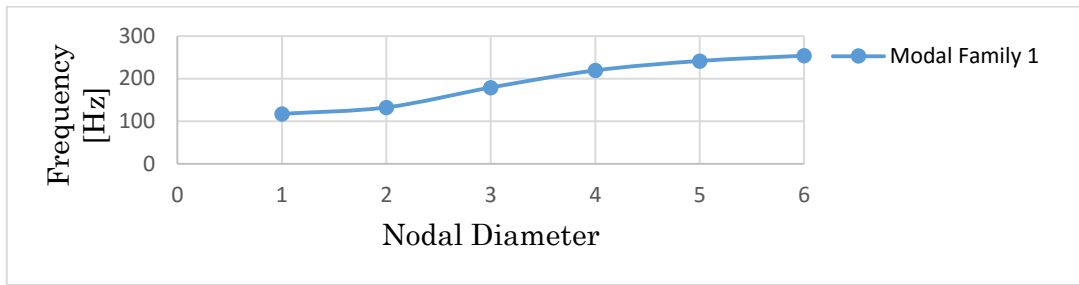


Figure 21. Experimental graph f-ND for the first modal family.

4.4 Graph f-ND of the FE disk model

Once the complete modal analysis has been performed in Ansys, the same graph of Figure 21 can be obtained for the FE model of the disk. The results are summarized in Figure 22. Each modal family is represented by a continuous line that connects a set of frequency values: the first modal family corresponds to the set of the first frequency values of each nodal diameter. In general, an infinite number of natural frequencies corresponds to each nodal diameter, in practice only the first modal families are taken into account.

By considering every modal family it can be noticed that for a low number of nodal diameters the frequency values progressively increase. On the other hand, if the number of nodal diameters is high, each line tend to assume an asymptotic behavior. The sloped part represents a disk-dominated mode: the disk segments undergo a deformation but the blades are almost undeformed. On the contrary, the horizontal lines are blade dominated modes because the disk segments are extremely rigid while the interblade coupling is weak (Castanier and Pierre, 2006c).

As far as the blade modes are concerned, they are usually classified as: bending or flexion, torsion, edgewise and complex modes (Seinturier, 2007b).

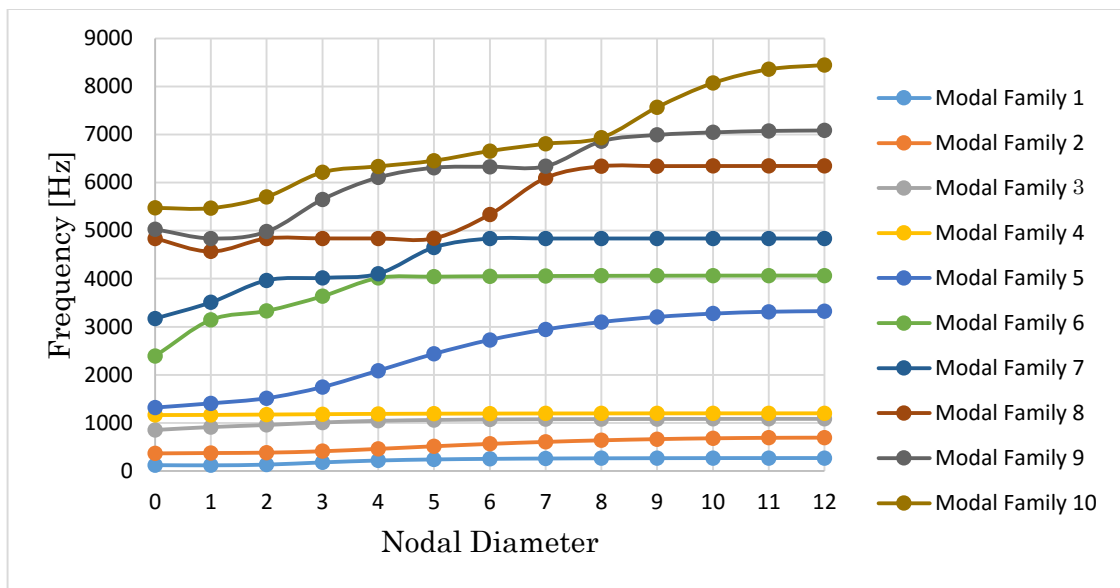


Figure 22. Graph f-ND of the FE disk model.

Moreover, there are regions called Veerings where the disk and the blade modes appear to veer away one from each other: the correspondent modes feature a mixed disk-blade motion (Castanier and Pierre, 2006d).

5 TUNING THE FE MODEL

5.1 The impact hammer test

An experimental study was carried out in 2011 on the *Octopus* test rig, located at the LAQ AERMEC laboratory of Politecnico di Torino. The bladed disk behavior was analyzed in different operating conditions. As an example, Figure 23 shows the experimental natural frequencies of the disk in the free condition, measured with an impact hammer test.

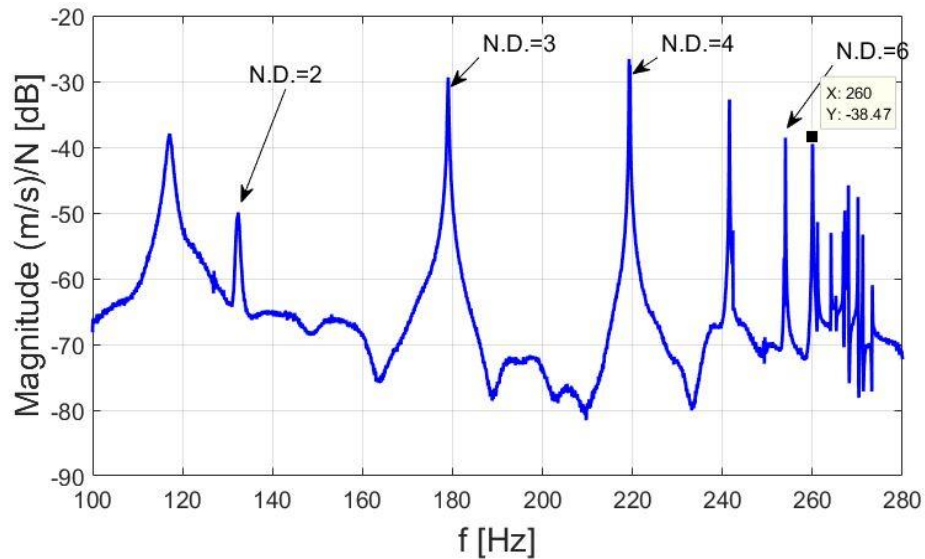


Figure 23. Impact hammer test results.

Results for the first modal family were gathered for the range of nodal diameters from 2 to 6. The values of natural frequencies associated with the number of nodal diameters are shown in TABLE I.

TABLE I

EXPERIMENTAL NATURAL FREQUENCIES MEASURED FOR NODAL DIAMETER 2-6 WITH AN HAMMER TEST

Nodal Diameter	Natural Frequency [Hz]
2	132.4
3	179.1
4	219.3
5	241.6
6	254.0

5.2 The tuning process

After the creation of the finite element model of the disk, it was important to make sure that the natural frequencies obtained with the modal analysis matched with the experimental ones. In order to guarantee the accuracy of the results it was necessary to perform a tuning of the finite element model.

First, the results obtained for the first modal family in Ansys did not find an equal experimental counterpart (see TABLE II). The main reason of the mismatch was due to a wrong loading configuration of the disk, as the one already presented in Figure 17.

TABLE II

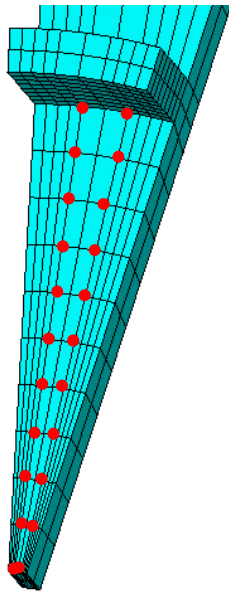
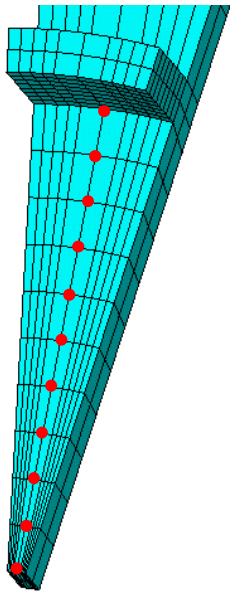
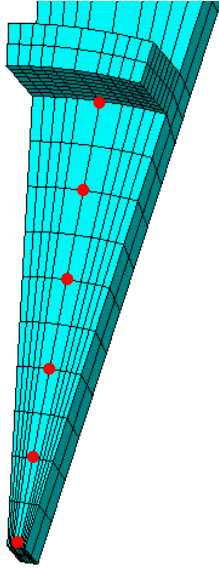
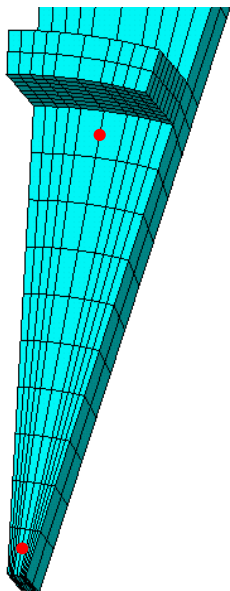
COMPARISON BETWEEN EXPERIMENTAL AND NUMERICAL NATURAL FREQUENCIES

Nodal Diameter	Natural Frequency in Ansys before tuning [Hz]	Experimental Natural Frequency [Hz]
2	138.23	132.4
3	180.23	179.1
4	218.17	219.3
5	240.21	241.6
6	252.34	254.0

In order to obtain frequency values as close as possible to the experimental ones, the tuning procedure was carried out by following an iterative scheme (see TABLE III).

TABLE III

FOUR DIFFERENT LOADING CONDITIONS OF THE DISK SECTOR

ND	f		ND	f	
2	135.90		2	135.07	
3	179.57		3	179.35	
4	218.10		4	218.09	
5	240.21		5	240.21	
6	252.34		6	252.34	
ND	f		ND	f	
2	134.64		2	132.39	
3	179.25		3	178.89	
4	218.08		4	218.06	
5	240.21		5	240.21	
6	252.34		6	252.34	

By changing the loading condition of the disk at each iteration it was possible to determine the number and the positions of the nodes to be constrained.

If the results of the Hammer test are taken as a reference, the final tuned loading condition is shown in Figure 24.

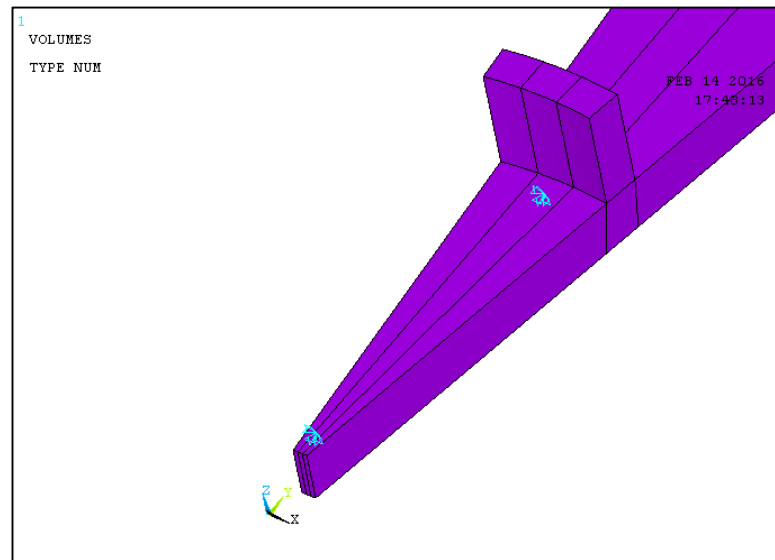


Figure 24. Nodes constrained on the tuned model.

5.3 Comparison of the results before and after tuning

Once the tuning procedure has been completed, it is interesting to summarize all the results in a single table (see TABLE IV). Thanks to the tuning procedure, the difference between experimental and numerical natural frequencies was reduced to an

average value of 0.3%. As a consequence, the FE model is able to reproduce the behavior of the *Octopus* bladed disk with high accuracy.

TABLE IV

COMPARISON OF THE NATURAL FREQUENCIES OBTAINED BEFORE AND AFTER TUNING

Nodal Diameter	Natural frequency in Ansys before tuning [Hz]	Experimental Natural Frequency [Hz]	Natural frequency in Ansys after tuning [Hz]
2	138.23	132.4	132.4
3	180.23	179.1	178.9
4	218.17	219.3	218.1
5	240.21	241.6	240.2
6	252.34	254.0	252.3

6 FINITE ELEMENT MODEL OF THE BLISK WITH CYLINDRICAL UNDERPLATFORM DAMPERS

6.1 Modeling of the components in Solidworks

The bladed disk studied in this thesis was equipped with cylindrical underplatform dampers, whose CAD model is shown in Figure 25.

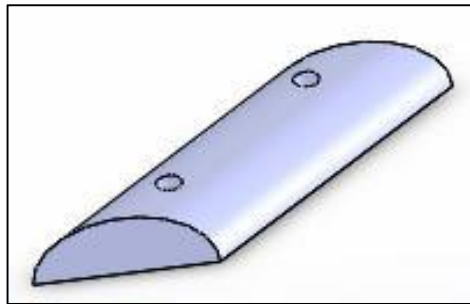


Figure 25. CAD model of the cylindrical underplatform damper.

This geometry can be obtained starting from a cylindrical shape and performing two cuts at 45 degrees. The two holes are necessary because, in case of a static test rig, wires are used to keep each damper in contact with the blades platforms. For a more detailed description of the working principle of the *Octopus* test rig, the reader is referred to the chapter focused on this topic.

The underplatform dampers are coupled to the blisk by means of properly designed removable blade platforms, whose CAD model is shown in Figure 26.

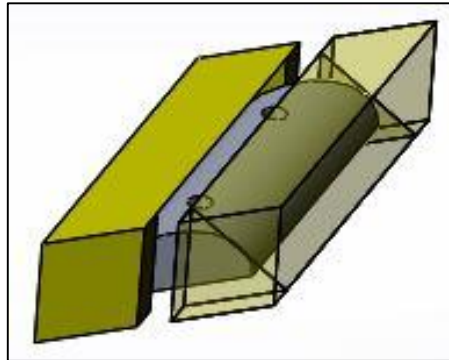


Figure 26. Cylindrical damper and blade platforms.

The different disk components can be assembled in Solidworks. A condition of tangency is imposed between damper and blade platforms, which are subsequently coupled to the disk. The final result is shown in Figure 27.

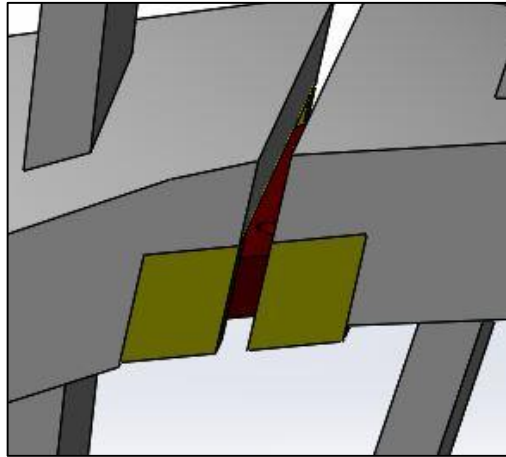


Figure 27. CAD model of the bladed disk with UPDs.

6.2 Generation of the FE model

The FE model was generated in Ansys Mechanical APDL. With respect to Solidworks, it is not possible to create the FE models of the single components and then perform the assembly operation. The complete model was imported to Ansys as a single piece, and was subsequently divided into sub-components.

In order to ensure a correct coupling between underplatform damper and blade platform, particular attention was dedicated to the meshing operation: the two bodies must have the same nodes along their contact line. The strategy adopted to fulfill this requirement was to divide the two bodies into smaller sub-volumes in order to control the meshing procedure with high accuracy. A detail of the complete FE model is shown in Figure 28.

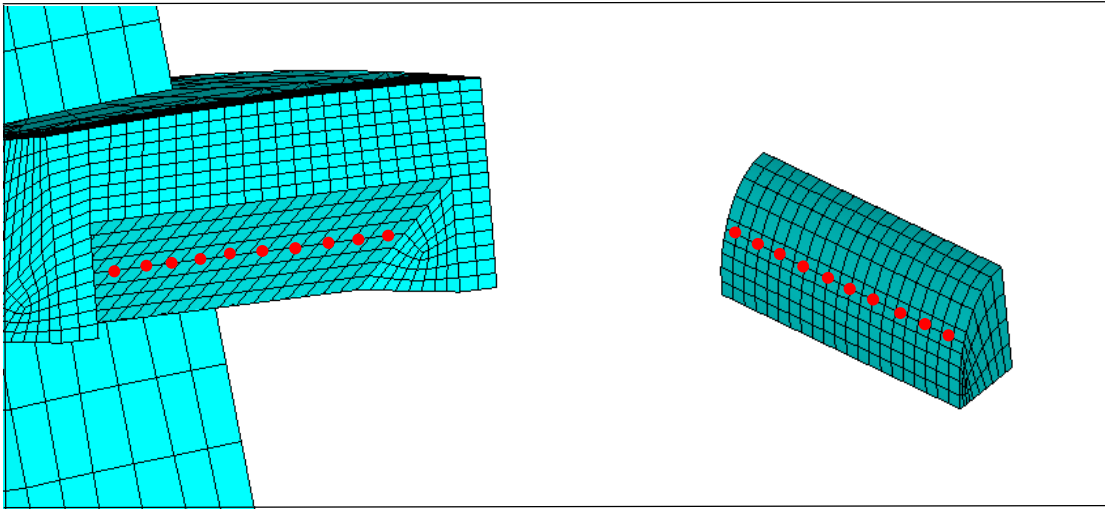


Figure 28. Nodes of UPD and blade platform along the contact line.

7 STIFFNESS OF THE DISK WITH 12 NODAL DIAMETERS

7.1 The case of a single disk sector with lateral constraints

Once the modal analysis of the bladed disk has been performed, it is interesting to make a comparison between its natural frequencies calculated in the working condition with 12 nodal diameters and the ones obtained for the reference case of a single disk sector whose lateral nodes have been constrained in the three directions (see Figure 29).

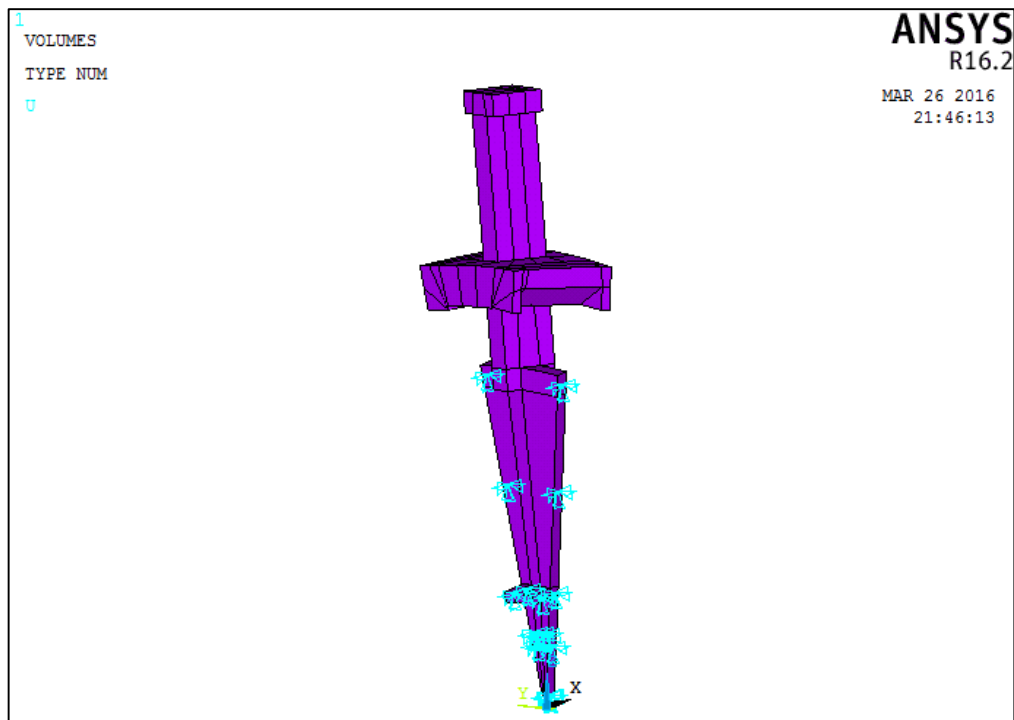


Figure 29. Single disk sector with lateral constraints.

A disk sector can be defined as “one blade plus the corresponding segment of the disk” (Castanier and Pierre, 2006, p.385). When the bladed disk is excited in such a way to present 12 nodal diameters, one for each blade, the stiffness of the system reaches its maximum. In this working condition, the main contribution to the disk dynamic response is given by the blades.

In case of a thick and rigid bladed disk, it is possible to approximate the dynamic behavior with 12 nodal diameters by replicating around the rotation axis a single disk sector whose nodes on the lateral interfaces have been given fixed constraints (see Figure 30) .

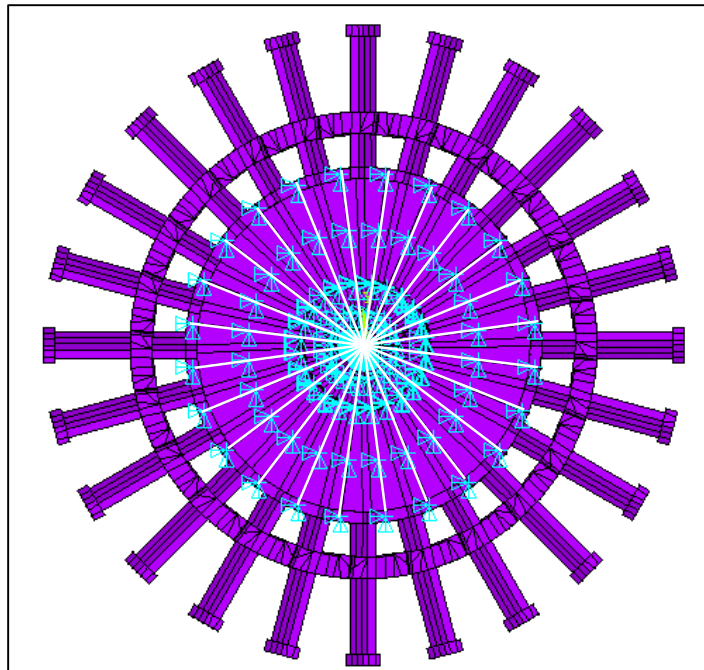


Figure 30. Disk made of single sectors with lateral fixed constraints.

By plotting the natural frequencies calculated for the reference case previously mentioned as a function of the number of nodal diameters, horizontal lines are obtained (see Figure 31).

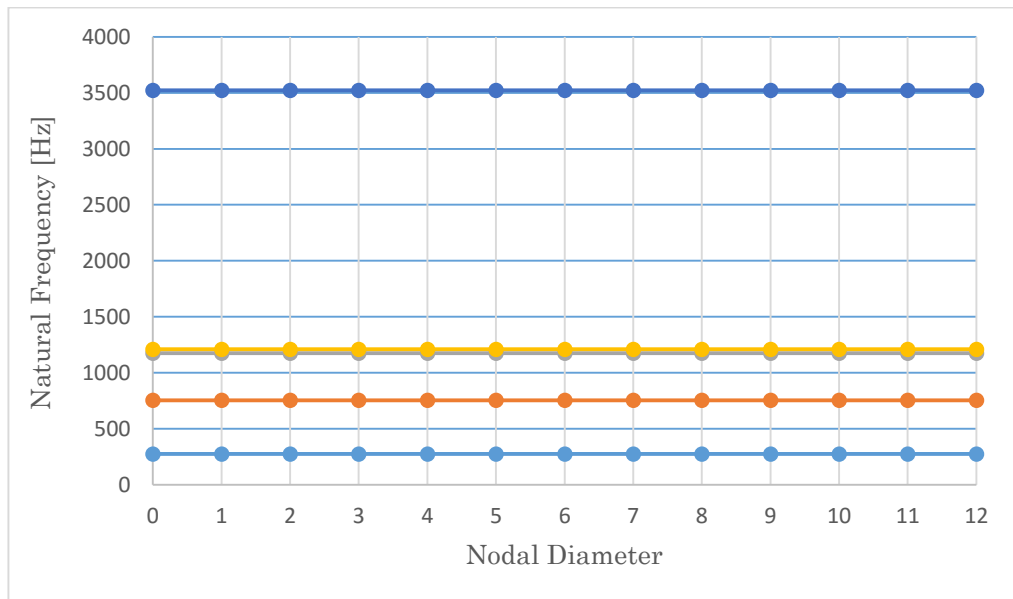


Figure 31. Graph frequency-ND for the case of bladed disk made of sectors constrained at the interfaces.

The lines are horizontal because, for each natural frequency value, the system reaches a configuration with maximum stiffness, i.e. with 12 nodal diameters. Given that for each natural frequency the disk segments are constrained in the three

directions, what changes from a given modal family with respect to the following one is the mode shape of the blades.

7.2 Full disk and single constrained disk sector: comparison between their dynamic behavior

In the following tables the results gathered from the modal analysis of both the full disk and the single disk sector with lateral constraints are compared. In particular, attention is focused on the first three modal families of the full disk and on the first three natural frequencies of the single disk sector. The blade mode shapes identified are first bending (1F), second bending (2F) and first torsion (1T) respectively. The nodal diameters are highlighted in red.

TABLE V

COMPARISON BETWEEN FULL DISK AND SINGLE DISK SECTOR: CASE 1

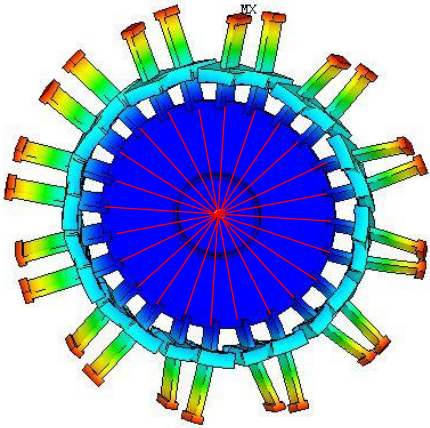
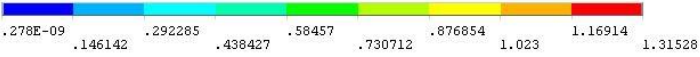
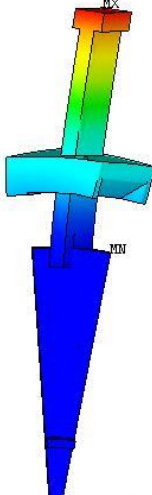
<p>ND=12</p>	<p>1 NODAL SOLUTION STEP=13 SUB =1 FREQ=269.286 /CYCEXPAND Hrm Index= 12 USUM (AVG) RSYS=0 DMX =1.31528 SMN =.278E-09 SMX =1.31528</p> <p style="text-align: right;">FEB 13 2016 17:08:36</p>
<p>Frequency=269.3 Hz</p>	
<p>First bending mode (1F) of the blade</p>	
<p>First frequency value</p>	<p>1 NODAL SOLUTION STEP=1 SUB =1 FREQ=274.155 USUM (AVG) RSYS=0 DMX =6.50005 SMX =6.50005</p> <p style="text-align: right;">FEB 13 2016 16:53:23</p>
<p>Frequency=274.2 Hz</p>	
<p>First bending mode (1F) of the blade</p>	

TABLE VI

COMPARISON BETWEEN FULL DISK AND SINGLE DISK SECTOR: CASE 2

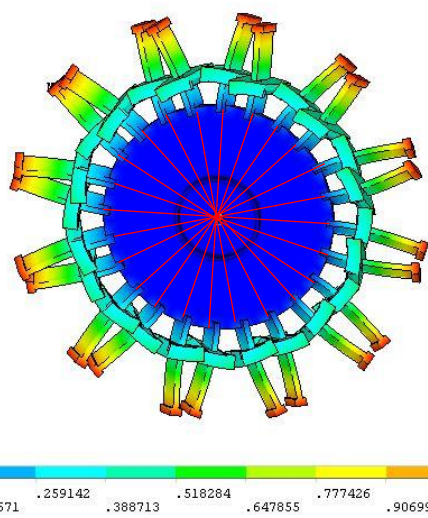
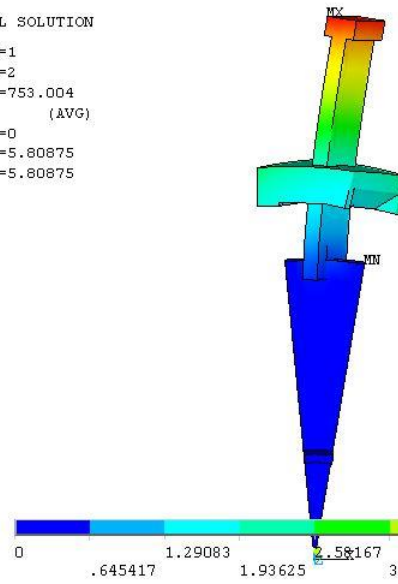
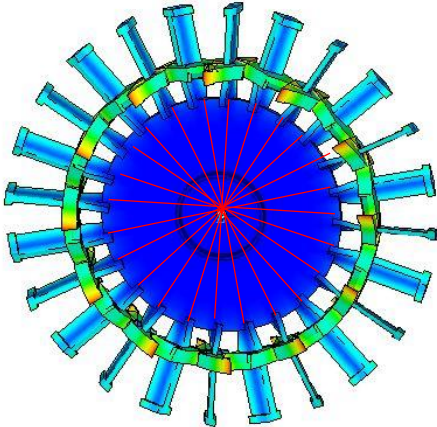
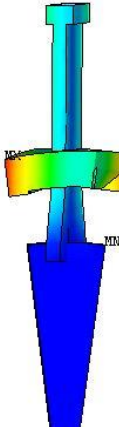
<p>ND=12</p>	<div data-bbox="606 515 766 750"> <p>1 NODAL SOLUTION STEP=13 SUB =2 FREQ=693.177 /CYCEXPAND Hrm Index= 12 USUM (AVG) RSYS=0 DMX =1.16614 SMN =.988E-09 SMX =1.16614</p> </div> <div data-bbox="1244 571 1364 616"> <p>FEB 13 2016 17:10:48</p> </div> 
<p>Frequency=693.2 Hz</p>	
<p>Second bending mode (2F) of the blade</p>	
<p>Second frequency value</p>	<div data-bbox="606 1164 766 1355"> <p>1 NODAL SOLUTION STEP=1 SUB =2 FREQ=753.004 USUM (AVG) RSYS=0 DMX =5.80875 SMX =5.80875</p> </div> <div data-bbox="1260 1220 1380 1265"> <p>FEB 13 2016 16:55:54</p> </div> 
<p>Frequency=753 Hz</p>	
<p>Second bending mode (2F) of the blade</p>	

TABLE VII

COMPARISON BETWEEN FULL DISK AND SINGLE DISK SECTOR: CASE 3

<p>ND=12</p>	<p>1 NODAL SOLUTION STEP=13 SUB =3 FREQ=1084.1 /CYCEXPAND Hrm Index= 12 USUM (AVG) RSYS=0 DMX =1.4869 SMN =.116E-08 SMX =1.4869</p> <p>FEB 13 2016 17:12:09</p>
<p>Frequency=1084 Hz</p>	
<p>First torsion mode (1T) of the blade</p>	
<p>Third frequency value</p>	<p>1 NODAL SOLUTION STEP=1 SUB =3 FREQ=1174.27 USUM (AVG) RSYS=0 DMX =7.29071 SMX =7.29071</p> <p>FEB 13 2016 16:57:34</p>
<p>Frequency=1174 Hz</p>	
<p>First torsion mode (1T) of the blade</p>	

By comparing the values of the natural frequencies, it is evident that the working condition of the full disk with 12 nodal diameters is less stiff than the one of the single disk sector constrained at its lateral interfaces. As a consequence, even when the maximum number of nodal diameters is present, each segment of the disk undergoes a deformation and contributes to the dynamic response.

8 THE OCTOPUS NUMERICAL CODE

8.1 General overview of the numerical code

A numerical code was developed in MATLAB environment to perform the calculation of the forced dynamic response of a turbine bladed disk with or without underplatform dampers.

The dynamic of the disk is introduced in MATLAB by uploading its reduced mass and stiffness matrices, extracted from Ansys using a reduction procedure. As far as the damper is concerned, a FE model is not necessary, it is enough to provide the values of its mass and inertia moments calculated with respect to its center of mass. The red dot in Figure 32 shows the position of the damper barycenter.

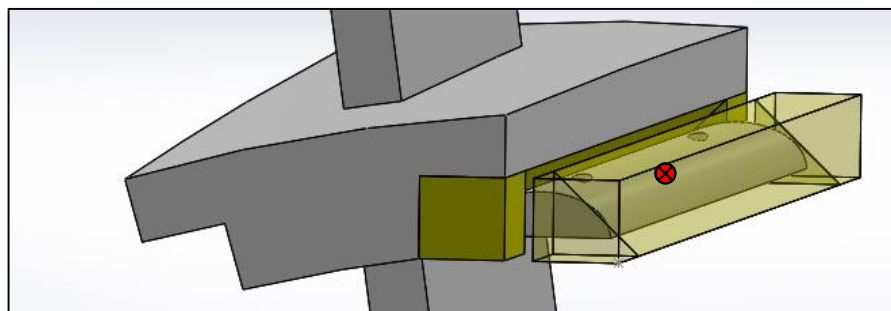


Figure 32. Damper center of mass.

8.2 Input parameters required by Octopus numerical code

A set of input parameters has to be introduced in the numerical code in order to perform the calculation of the turbine bladed disk response (see TABLE VIII).

TABLE VIII

INPUT PARAMETERS FOR THE OCTOPUS NUMERICAL CODE

Damper mass and moments of inertia	m_d, I_x, I_y, I_z
Damper and platform versors	$t_R, t_L, n_R, n_L, n_{Rad}, w$
Contact points coordinates with respect to the damper center of mass	X_L, X_R
Contact stiffnesses	k_n, k_t, k_{tz}
Friction coefficient	μ_R, μ_L
Stiffness and mass matrices of the blade	KM
Modal damping	$zita$
Centrifugal force	F_C
Coordinates of damper center of mass	x_m, y_m, z_m
Excitation force	F_{ext}

The values of the contact stiffnesses k_n, k_t, k_{tz} and of the friction coefficients μ_R, μ_L are obtained from analytical calculations and tuning procedures. The modal damping was evaluated through the *Half-Power Bandwidth Method* (see Appendix A). The directional cosines of each versor $t_R, t_L, n_R, n_L, n_{Rad}, w$, i.e. their Cartesian coordinates with respect to the global reference system, were calculated in Solidworks:

the starting point was the identification of the directions normal and parallel to the platform n and t and parallel to the damper axis w . The versors related to these three directions were generated: their Cartesian coordinates are the directional cosines required. The orientation of each versor normal to the blade platforms is shown in Figure 33.

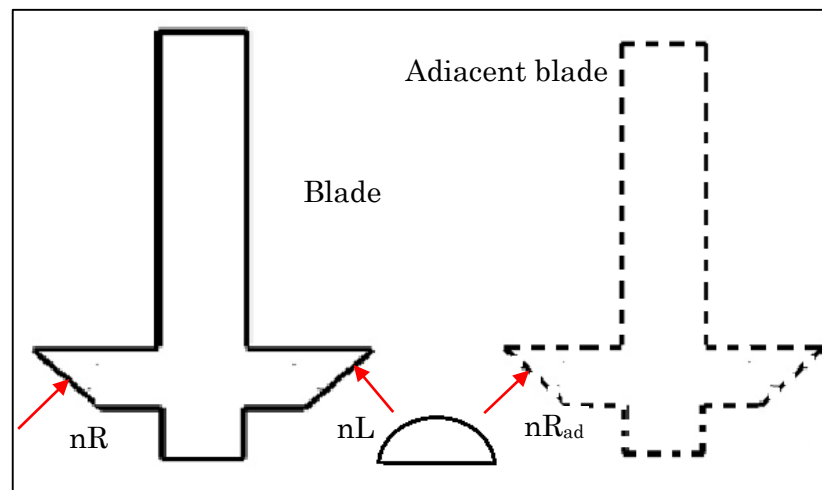


Figure 33. Platform versors.

8.3 Functioning principle of the numerical code

A general overview of the functioning principle of the Octopus numerical code is presented in Figure 34. Once the FE model of the disk has been generated, its mass and stiffness matrices are provided to the numerical code.

The nonlinear second order differential equilibrium equations of the disk and of the underplatform dampers can be solved with different techniques. A first approach consists in using a Direct Time Integration Method (i.e. Newmark- β) which, even if precise, requires a significant computational effort. If the solution is periodical, in order to reduce the computational time a frequency based method can be used.

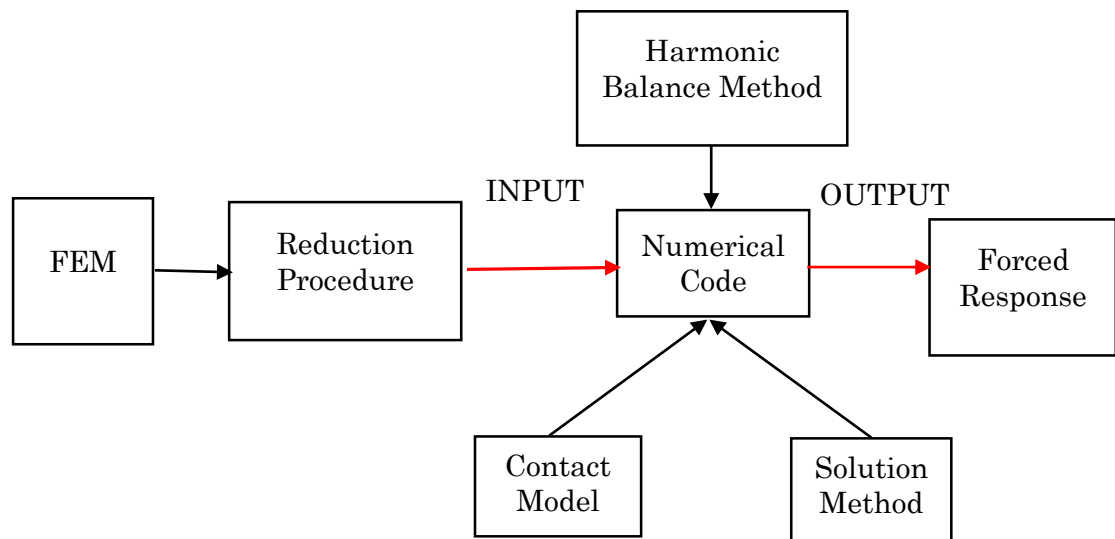


Figure 34. Block diagram of the Octopus numerical code.

As far as the case studied in this thesis is concerned, having periodical external excitation, leads to periodical displacements and non-linear forces at steady-state (Firrone and Zucca, 2011). The Harmonic Balance Method calculates the response at steady state in the frequency domain by decomposing the periodical response into a

Fourier series and turning a set of differential equations into a set of algebraic equations (Baraa et al., 2011).

After this first simplification it is necessary to identify a solution method for the system of non-linear algebraic equations previously obtained, like the Newton-Raphson iteration. In the *Octopus* numerical code, the non-linear system solver adopted is the MATLAB function *fsolve*, which uses as iterative scheme either *Trust region-Dogleg* or *Levenberg-Marquardt*.

The presence of friction requires introducing non-linear contact elements between dampers and platforms: sliding with friction in two orthogonal directions on the damper surfaces and the possible lift off can be simulated.

As output, the Octopus numerical code calculates the FRF of the disk in different working conditions, namely:

- Free working condition, i.e. without underplatform dampers.
- Stick working condition, when the dampers due to the centrifugal force are stuck between the blade platforms and do not dissipate energy by friction.
- Nonlinear working condition when the dampers, sliding with respect to the blade platforms, generate nonlinear friction forces.

9 REDUCTION OF THE FINITE ELEMENT MODEL

9.1 The Craig-Bampton method

The computational time required for the numerical calculation of the disk FE model can be dramatically reduced through a reduction method. In general, the reduction of the FE model is performed through a coordinate transformation:

$$\{x\} = [T]\{x_{red}\} \quad (9.1.1)$$

where T is a transformation matrix, calculated differently for every technique implemented in literature.

In case of nonlinear systems, like a turbine disk equipped with underplatform dampers, the Craig-Bampton method is the most convenient solution. According to this technique, the global system DOFs are divided into master and slave. The reduced model encompasses only the master DOFs and a set of modal shapes, which substitute the slave DOFs (Zucca et al., 2006).

9.2 Reduction of the constrained disk sector

The reduction procedure, developed in Ansys environment, was applied to the FE model of a single sector of the disk whose nodes on the two lateral faces are constrained in the three directions, as shown in Figure 35.

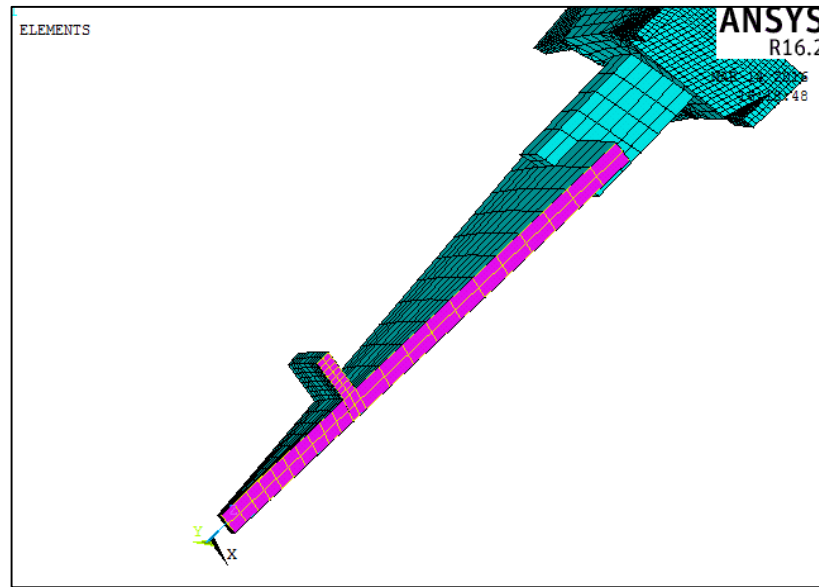


Figure 35. Constrained degrees of freedom of the disk sector.

The set of master nodes includes: the contact nodes on the two platform surfaces, the node where the excitation force is applied and the nodes where the system response is measured. Figure 36 shows the set of contact nodes chosen for the right platform.

As a result of the reduction procedure, the reduced mass and stiffness matrices of the disk sector were extracted and uploaded on the *Octopus* numerical code. Because of the fixed constraints assigned to the initial FE model, the cyclic symmetry properties in MATLAB are applied only to the blades and not to the disk segments. Consequently, when the modal analysis is performed, it does not consider the full disk dynamic but only the blades one. This kind of approximation can't be applied in general, it is acceptable only for the particular case of bladed disks with a high stiffness, i.e.

negligible disk compliance. A common example of this kind of configuration is represented by turbines for power generation whose disk is actually a drum.

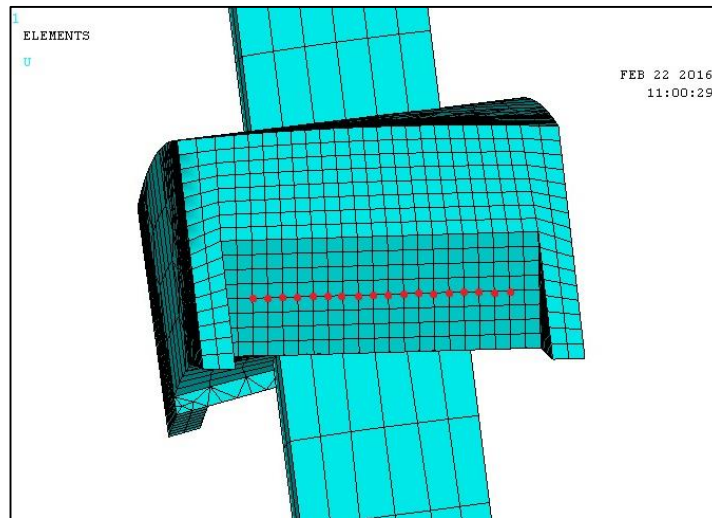


Figure 36. Contact nodes on the right platform.

9.3 Reduction of the full disk

It has been proven in Chapter 7 that, for the Octopus bladed disk, even when 12 nodal diameters are present in the structure the disk segments contribute to the disk dynamic; hence the reduction procedure previously described cannot be used.

A new reduction method developed in Ansys has been tailored to the disk analyzed in this thesis. The main difference with respect to the previous reduction procedure relies in the type of constraints applied to the disk sector, namely cyclic symmetry

constraints (see Figure 37): the displacement at the interfaces between each disk sector is allowed.

As a result, it is possible to extract the reduced mass and stiffness matrices of the whole disk, for a previously defined dynamic working condition, i.e. with a certain number of nodal diameters present in the structure.

Once the new matrices are loaded on the *Octopus* numerical code, for the free condition the natural frequencies obtained in MATLAB must be equal to the ones calculated in Ansys through the modal analysis of the tuned FE disk model (see from TABLE IX to TABLE XIII). The small differences in values, of around 0.1%, are justified by the fact that the reduction procedure, even if performed with high accuracy, leads to a loss of information. By looking at the results it is evident that with the new reduction procedure, the disk segments dynamic behavior is captured.

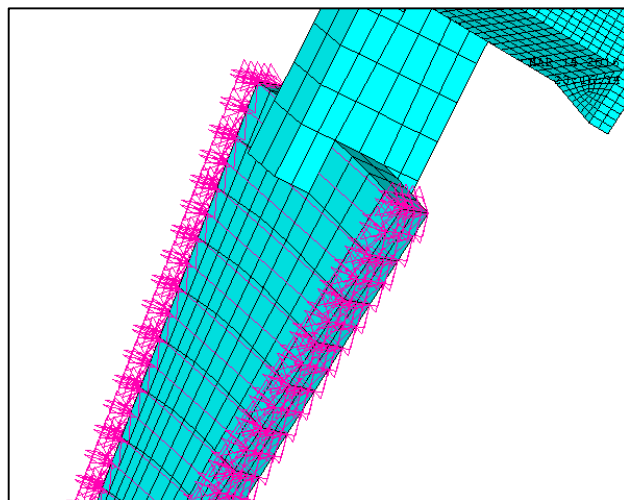


Figure 37. Cyclic symmetry constraints.

TABLE IX

COMPARISON BETWEEN NATURAL FREQUENCIES CALCULATED IN ANSYS
AND MATLAB: ND=2

Nodal Diameter 2	
Natural frequencies ANSYS [Hz]	Natural frequencies MATLAB [Hz]
132.39	132.50
381.34	382.15
956.73	958.94
1174.10	1175.70

TABLE X

COMPARISON BETWEEN NATURAL FREQUENCIES CALCULATED IN ANSYS
AND MATLAB: ND=3

Nodal Diameter 3	
Natural frequencies ANSYS [Hz]	Natural frequencies MATLAB [Hz]
178.89	179.24
410.50	411.19
1008.90	1011.72
1181.9	1182.08

TABLE XI

COMPARISON BETWEEN NATURAL FREQUENCIES CALCULATED IN ANSYS
AND MATLAB: ND=4

Nodal Diameter 4	
Natural frequencies ANSYS [Hz]	Natural frequencies MATLAB [Hz]
218.06	218.69
459.47	460.05
1043.30	1046.16
1187.90	1187.08

TABLE XII

COMPARISON BETWEEN NATURAL FREQUENCIES CALCULATED IN ANSYS
AND MATLAB: ND=5

Nodal Diameter 5	
Natural frequencies ANSYS [Hz]	Natural frequencies MATLAB [Hz]
240.21	241.02
513.83	514.41
1061.00	1064.24
1192.00	1190.40

TABLE XIII

COMPARISON BETWEEN NATURAL FREQUENCIES CALCULATED IN ANSYS
AND MATLAB: ND=6

Nodal Diameter 6	
Natural frequencies ANSYS [Hz]	Natural frequencies MATLAB [Hz]
252.34	253.26
2 563.57	564.22
1070.50	1074.26
1194.70	1192.54

10 MODAL ANALYSIS OF THE BLADED DISK WITH GLUED UNDERPLATFORM DAMPERS

10.1 Calculation of the natural frequencies in Ansys

As previously mentioned, the *Octopus* numerical code performs the calculation of the bladed disk natural frequencies also when the dampers are stuck between the blade platforms. The FE model of the blisk with UPDs, built in Ansys, represents the limit contact condition between platforms and dampers: they are glued as part of a unique body. Figure 38 shows a detail of the FE model with glued UPDs

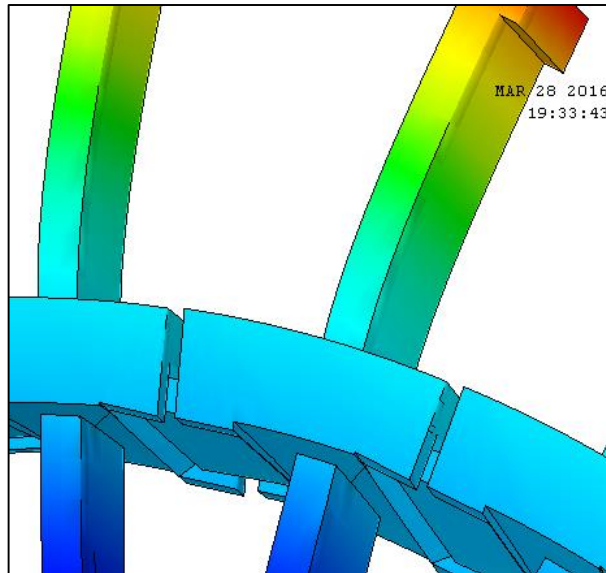


Figure 38. UPDs glued to the blade platforms.

By performing the modal analysis in Ansys, it is possible to compute the natural frequencies of the disk, and subsequently plot them as a function of the number of nodal diameters (see Figure 39).

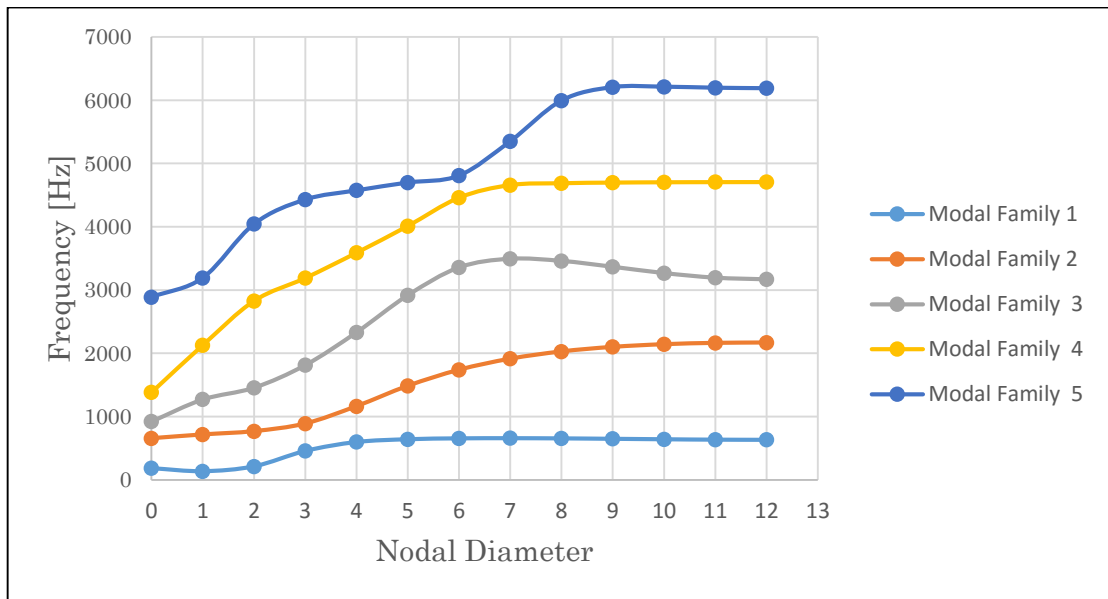


Figure 39. Graph f-ND when the UPDs are glued to the disk.

Figure 40 shows the working condition with 12 nodal diameters: all the blades oscillate out of phase with the same amplitude.

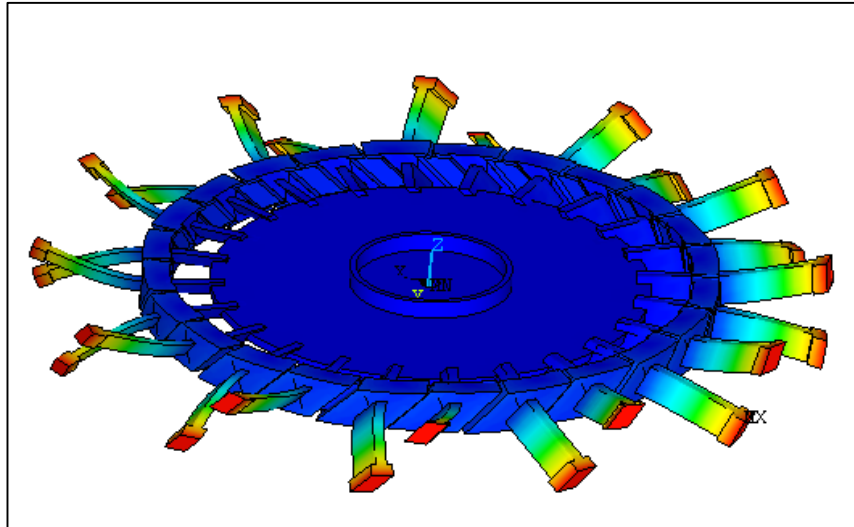


Figure 40. Sticking modal shape with 12 nodal diameters.

10.2 Comparison with the experimental natural frequencies

TABLE XIV compares the numerical natural frequencies calculated in Ansys with the experimental ones for the first modal family. The experimental results are obtained with an impact hammer test for the nodal diameters 2, 3 and 4 with the dampers in the sticking condition. It is evident that the experimental frequencies are definitely lower.

The aim of this analysis is only to provide an upper bound to each natural frequency value for each nodal diameter in the sticking condition. In order to obtain accurate results also in the numerical analyses it is necessary to introduce a contact model.

TABLE XIV

COMPARISON BETWEEN EXPERIMENTAL AND NUMERICAL NATURAL FREQUENCIES IN THE STICK CONDITION

ND	Experimental natural frequencies [Hz]	Numerical natural frequencies calculated in Ansys [Hz]
2	145,8	212.16
3	242	456.79
4	381,5	598.09

11 CONTACT MODEL

11.1 Two dimensional tangential relative displacement and variable normal load

The interaction between underplatform dampers and blade platforms must be addressed by selecting an efficient contact model. For the case studied in this thesis, the most advanced reference available in literature for modeling contacts with friction was chosen. It takes into account a 2 dimensional tangential relative displacement and a variable normal load (Yang and Menq, 1998).

Once the FE model of the damper has been generated, a finite number of contact nodes must be selected in order to model the behavior of friction contacts (Firrone and Zucca, 2011a). Figure 41 shows the forces acting on three contact nodes of a cylindrical underplatform damper

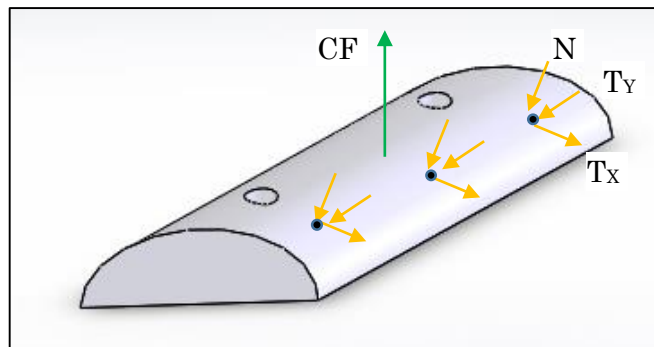


Figure 41. Forces acting on the damper.

where N is the normal load, T_x and T_y are the tangential friction forces, CF is the centrifugal force.

The normal load is directly related to the centrifugal force through the damper mass. Figure 42 explains the main relationship between these three parameters.

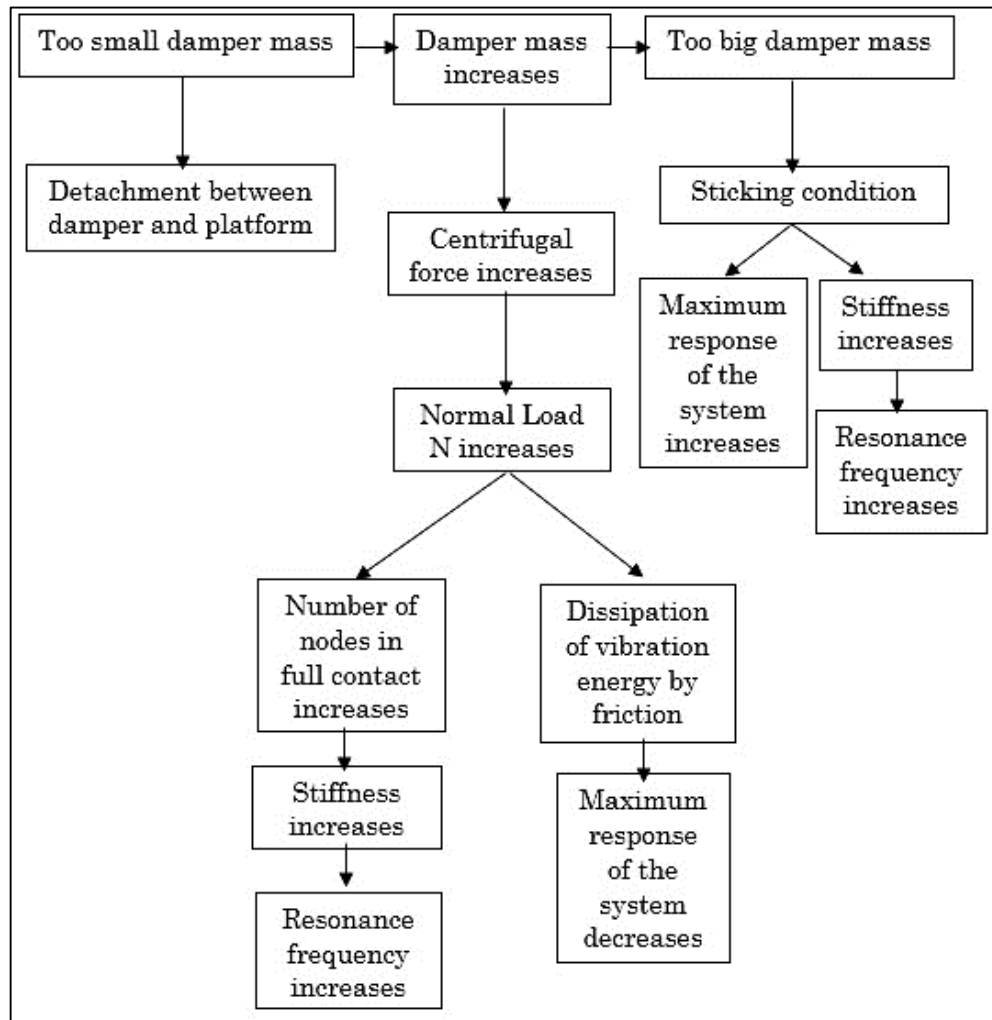


Figure 42. Influence of the damper mass on the system response.

11.2 Scheme of the contact model

A schematic of the contact model for the case of a cylindrical underplatform damper is shown in Figure 43. The contact between damper and platform occurs along the red line.

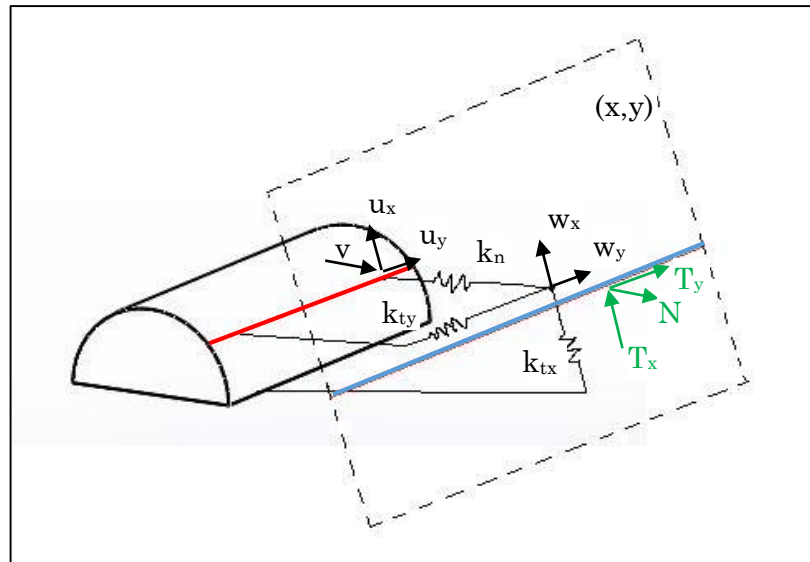


Figure 43. Contact model for cylindrical underplatform damper.

The plane (x, y) is tangent to the underplatform damper and represents the surface of the blade platform. The contact element defines by means of two springs the tangential contact stiffnesses k_{tx} and k_{ty} along the two orthogonal directions x and y . On the other hand, the normal contact stiffness is represented by k_n . The two parameters $u(t) = \{u_x(t); u_y(t)\}$ and $v(t)$ stand for the periodic relative displacements of the contact

nodes in the tangential and normal directions respectively. The parameter $w(t) = \{w_x(t); w_y(t)\}$ indicates the tangential slip amount occurring between the contact surfaces; μ is the friction coefficient (Firrone and Zucca, 2011b).

The variable normal load is defined as:

$$N = \max(N_0 + k_n v, 0) \quad (11.2.1)$$

where N_0 is the static normal pre-load obtained in a preliminary static analysis. It has been proved by Firrone et al. (2011a) that the static and dynamic equilibrium of the structure can be coupled by linking the static normal and tangential forces to the normal and tangential static relative displacements $u^{(0)}$ and $v^{(0)}$. As a consequence, (11.2.1) can be rewritten as:

$$N = \max[k_n v(t), 0] = \max[k_n v^{(0)} + k_n \mathbf{R}(v^{(n)} e^{in\omega t}), 0] \quad (11.2.2)$$

where n is the harmonic number of the Fourier series approximation and ω is the fundamental frequency of the excitation forces acting on the system.

11.3 The three contact conditions

In general three contact conditions are possible: stick, slip and separation. These three different possibilities can occur during each vibration period (Firrone and Zucca, 2011c). When the tangential relative motion is not sufficient to generate the slipping condition, the damper is stuck. For the simple case of a contact model with one dimensional tangential relative displacement, the tangential friction force can be computed as

$$T = k_t(u - w) \quad \text{with } \dot{w} = 0 \quad (11.3.1)$$

It must be underlined that in the sticking condition the contact is elastic and no slip occurs (Firrone and Zucca, 2011d). In the slipping condition the direction of T depends on the direction of the slipping velocity vector \dot{w} and the modulus is equal to the Coulomb limit value

$$T = \text{sign}(\dot{w})\mu N \quad (11.3.2)$$

Given that the relative displacement u is periodic, according to (11.3.1) also T varies in time with a periodic law. On the other hand, when the damper slips with respect to the platform, T assumes a value related to the one of the normal load N .

In general, as shown by (11.2.2), the value of the normal contact force N changes in time according to the variation of the relative normal displacement v . The particular working condition characterized by a constant value of N in each period is represented in Figure 44. Obviously, the portion of the graph where the tangential force T is constant (horizontal line) corresponds to the slipping condition.

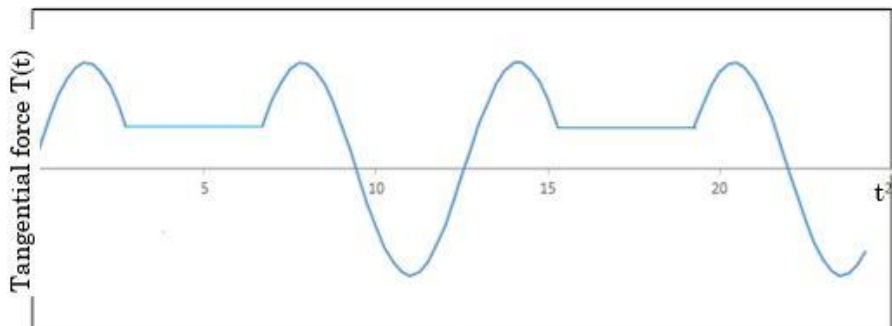


Figure 44. Variation of the tangential force T during stick-slip.

The stick-slip transition can be explained by introducing the concept of limit relative displacement. In general, if the value of the tangential relative displacement u is lower than the limit value u_{lim} , the damper is stuck. On the contrary, if $u \geq u_{lim}$ an alternation of stick and slip states occurs. The value of u_{lim} can be found by imposing that the tangential friction force T_{stick} in the slipping condition equals the value of T_{slip} in the sticking condition:

$$T_{stick} = k_t u \quad (11.3.3)$$

$$T_{slip} = \mu N \quad (11.3.4)$$

$$T_{stick} = T_{slip} = k_t u = \mu N \quad (11.3.5)$$

$$u_{lim} = \frac{\mu N}{k_t} \quad (11.3.6)$$

It is now evident that u_{lim} depends on the normal load N , on the tangential stiffness k_t and on the friction coefficient μ . If N is constant, u_{lim} can be plotted in time as an horizontal line. Figure 45 shows how the stick-slip transition occurs in terms of tangential relative displacement.

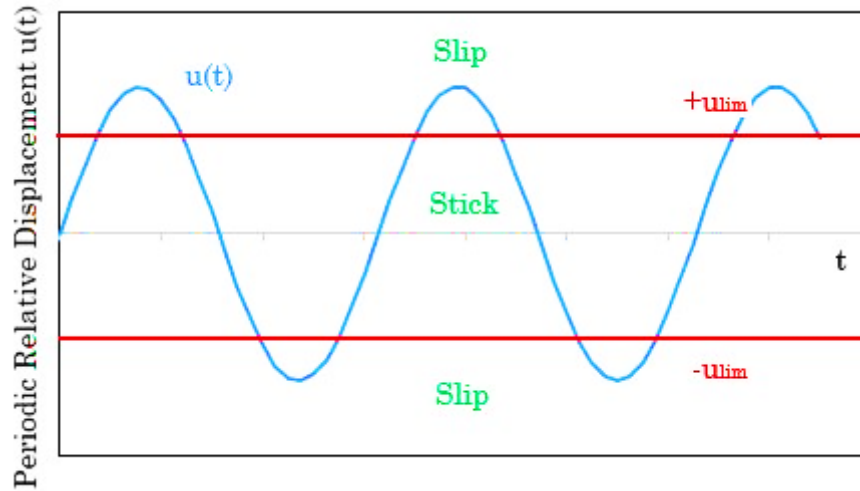


Figure 45. Stick-Slip transition for 1D case.

According to the contact model chosen in this thesis, the value of the two orthogonal friction forces in the sticking condition can be computed as:

$$\begin{Bmatrix} T_x \\ T_y \end{Bmatrix} = \begin{bmatrix} k_{tx} & 0 \\ 0 & k_{ty} \end{bmatrix} \left(\begin{Bmatrix} u_x \\ u_y \end{Bmatrix} - \begin{Bmatrix} w_x \\ w_y \end{Bmatrix} \right) \text{ with } \begin{Bmatrix} w_x \\ w_y \end{Bmatrix} = \begin{Bmatrix} 0 \\ 0 \end{Bmatrix} \text{ and } N \geq 0 \quad (11.3.7)$$

11.4 Transition criteria for the contact condition

It is important to summarize the conditions that cause the transition from a sticking working condition of the damper, to a possible lift off with respect to the platform or to the generation of slipping that dissipates vibrational energy. Figure 46 shows schematically how this process occurs.

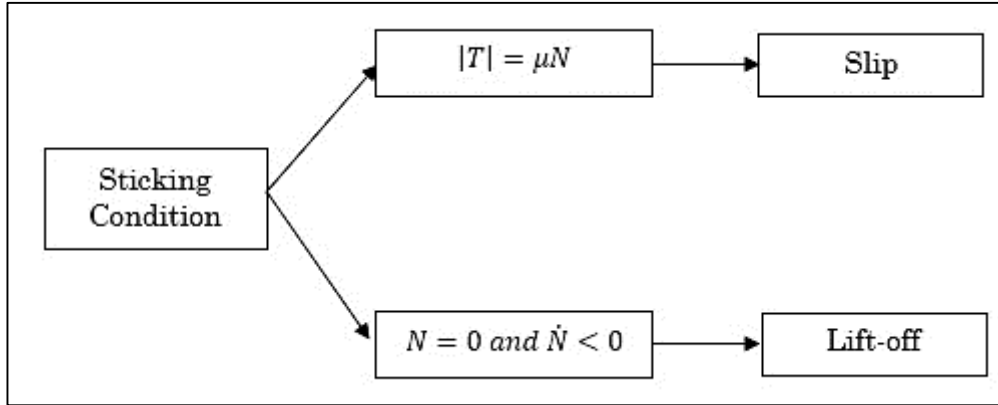


Figure 46. Transition criteria from the sticking condition.

In the slipping working condition the modulus of the tangential force assumes the Coulomb limit value. As far as the direction is concerned, it turns out to be parallel to the correspondent slip velocity vector \dot{w} (Firrone and Zucca, 2011e).

$$\sqrt{T_x^2 + T_y^2} = \mu N \quad (11.4.1)$$

$$\begin{Bmatrix} T_x \\ T_y \end{Bmatrix} = \frac{\mu N}{\|\dot{w}\|} \begin{Bmatrix} \dot{w}_x \\ \dot{w}_y \end{Bmatrix} \text{ with } \|\dot{w}\| = \sqrt{\dot{w}_x^2 + \dot{w}_y^2} \quad (11.4.2)$$

where

$$T_x = \frac{\mu N}{\sqrt{\dot{w}_x^2 + \dot{w}_y^2}} \|\dot{w}_x\| \hat{w}_y \quad (11.4.3)$$

$$T_y = \frac{\mu N}{\sqrt{\dot{w}_x^2 + \dot{w}_y^2}} \|\dot{w}_y\| \hat{w}_y \quad (11.4.4)$$

Figure 47 shows the transition criteria determining a change in the initial slip working condition.

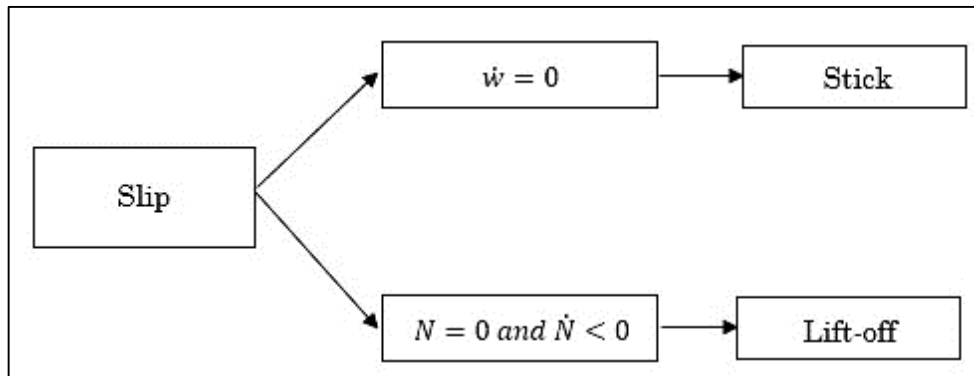


Figure 47. Transition criteria from the slipping condition.

Finally, if the contact points are separated from each other, both normal and tangential contact forces are null (Firrone and Zucca, 2011f). Figure 48 shows the transition criteria starting from the lift-off condition.

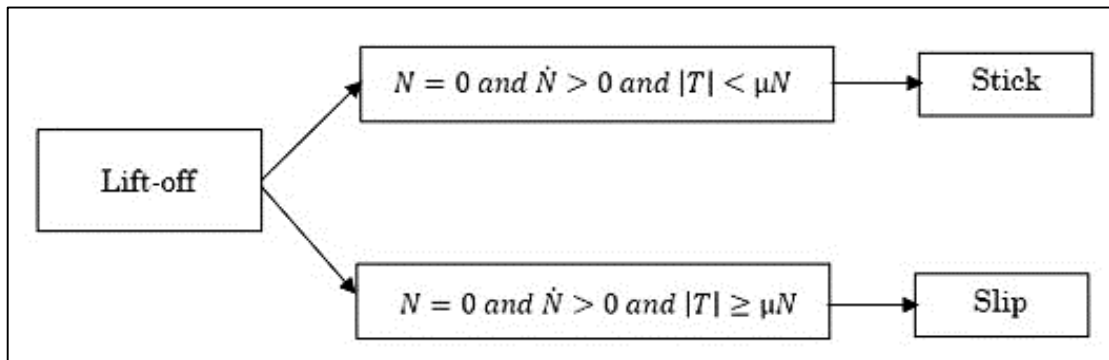


Figure 48. Transition criteria from the lift-off condition.

12 ESTIMATION OF THE NORMAL CONTACT STIFFNESS

12.1 Contact formulas for the calculation of the elastic approach

Each cylindrical underplatform damper is loaded against the blade platforms by the centrifugal force. As a consequence, a relative displacement, contact area and pressure distribution are generated at the contacts. Heinrich Rudolf Hertz (Feb. 22, 1857 – Jan., 1, 1894) studied the behavior of two bodies in point contact when pressed against each other. He found the relationship between contact force and pressure distribution, he proved that the contact area is elliptical and he wrote an expression for the elastic approach δ between the two bodies.

For the case of cylinder on a plane (line contact), Harris (1991) quotes the formula valid for the single contact in case of steel on steel, found empirically by Palmgren (1923)

$$\delta = 3,84 \cdot 10^{-5} \left(\frac{F}{L}\right)^{0.9} \cdot L^{0.1} \quad [F] = N, [L] = mm, [\delta] = mm \quad (12.1.1)$$

where F is the contact force and L is the length of the cylinder minus possible recesses.

A more recent formula was found by Brändlein (1999):

$$\delta = 4.05 \cdot 10^{-5} \frac{F^{0.925}}{L^{0.85}} \quad [F] = N, \quad [L] = mm, \quad [\delta] = mm \quad (12.1.2)$$

These empirical formulas were obtained by compressing a cylindrical roller between two flat parallel plates. For this reason, the total approach considered was 2δ .

However, for the case of a cylindrical underplatform damper loaded against the blade platforms, only the single approach δ has to be considered. Figure 49 shows a scheme of one cylindrical underplatform damper in contact with two adjacent blade platforms.

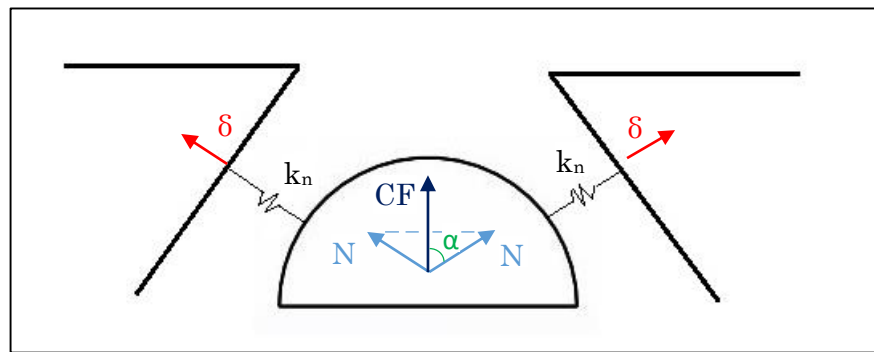


Figure 49. Elastic contact between damper and platform.

In detail, N_1 and N_2 are the two components of the centrifugal force CF along the normal directions to the blade platforms, k_n is the normal contact stiffness and δ is the approach. The equilibrium equation of the damper, neglecting its weight is:

$$CF = 2N\cos(\alpha) \quad (12.1.3)$$

hence, for the contact force it holds:

$$N = \frac{CF}{2\cos(\alpha)} \quad (12.1.4)$$

The value of the contact force N is directly related to the angle α formed by the direction of CF with the normal to the blade platform at the contact point. As previously shown by (12.1.1) and (12.1.2), the relationship between contact force and approach is not linear. In particular, (12.1.1) can be rewritten in the form:

$$F \cong k \delta^{1.1} \quad (12.1.5)$$

$$k = \left(\frac{L^{0.8}}{3,84 \cdot 10^{-5}} \right)^{\frac{10}{9}} \quad (12.1.6)$$

It can be observed that equation (12.1.5) is similar to the expression of the linear elastic force

$$F = kx \quad (12.1.7)$$

It is now interesting, according to (12.1.1), to plot the approach as a function of the contact force N producing it (see Figure 50).

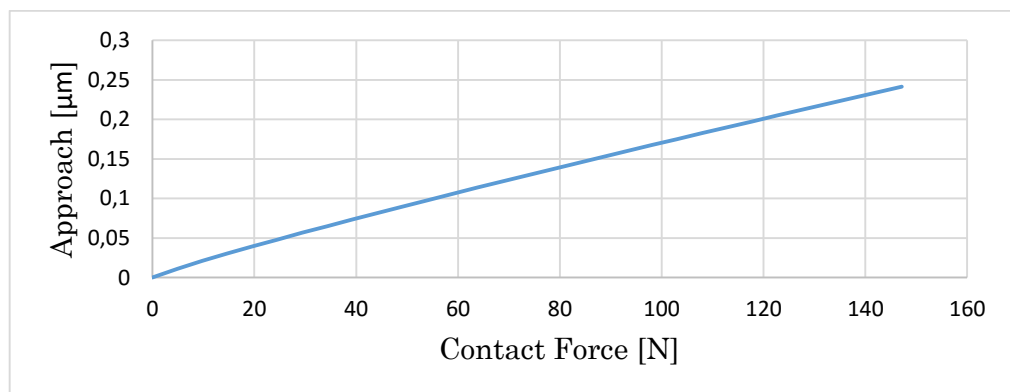


Figure 50. Graph elastic approach-contact force.

12.2 Calculation of the normal contact stiffness

During the experimental study, the centrifugal force was simulated through dead weights of either 5 or 15 kg. By multiplying the mass by the gravitational acceleration $g = 9.81m/s^2$, the centrifugal force can be evaluated. An estimation through (12.1.4) of the normal contact forces is presented in TABLE XV.

TABLE XV

CALCULATION OF THE NORMAL CONTACT FORCES

m [kg]	CF [N]	N [N]
5	49.05	34.68
15	147.15	104.05

The normal contact stiffness k_n in a first order of approximation can be calculated by linearizing the curve plotted in Figure 50 in the neighborhood of the value of the normal contact force N considered. By taking the derivative of the approach δ with respect to N and computing its value for a given N^* , the angular coefficient of the line tangent to the curve $\delta(N)$ at its point $(N^*, \delta(N^*))$ is calculated

$$\frac{1}{k_n} = \left(\frac{d\delta}{dN} \right)_{N=N^*} = \left(\frac{1}{k} \right)^{\frac{9}{10}} \cdot \frac{9}{10} \cdot N^{*-\frac{1}{10}} \quad (12.2.1)$$

If the curve is linearized in the neighborhood of N^* (see Figure 51), then the angular coefficient previously calculated assumes the meaning of the reciprocal of the normal contact stiffness.

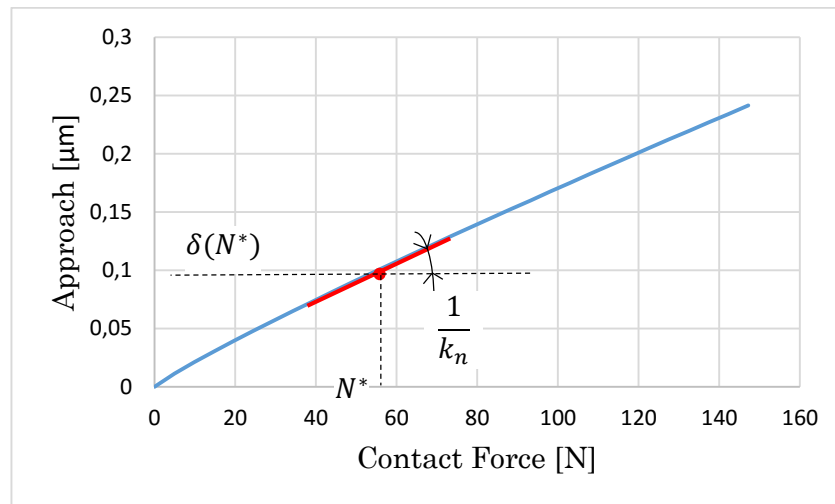


Figure 51. Graphical representation of the normal contact stiffness.

By following this procedure, the normal contact stiffnesses corresponding to the two different values of normal contact forces N_1 (if $m=5\text{kg}$) and N_2 (if $m=15\text{kg}$) are estimated as:

$$\frac{1}{k_{n1}} = \left(\frac{d\delta}{dN} \right)_{N=N_1} = \left(\frac{1}{k} \right)^{\frac{9}{10}} \cdot \frac{9}{10} \cdot N_1^{-\frac{1}{10}} = 1,705 \cdot 10^{-6} \frac{mm}{N} \quad (12.2.2)$$

$$\frac{1}{k_{n2}} = \left(\frac{d\delta}{dN} \right)_{N=N_2} = \left(\frac{1}{k} \right)^{\frac{9}{10}} \cdot \frac{9}{10} \cdot N_2^{-\frac{1}{10}} = 1.921 \cdot 10^{-6} \frac{mm}{N} \quad (12.2.3)$$

It follows that

$$k_{n1} = 5.86 \cdot 10^5 \frac{N}{mm} \quad (12.2.4)$$

$$k_{n2} = 5.21 \cdot 10^5 \frac{N}{mm} \quad (12.2.5)$$

The value of the normal contact stiffness k_n calculated by means of the Hertzian theory was introduced as an input value in MATLAB. Regarding the value of the tangential contact stiffness k_t , it has been tuned directly in MATLAB taking as a reference the experimental results.

12.3 Allowable static stress

It is possible to verify that the stress field generated by the contact forces on each body does not generate a plastic deformation of the structure. Orlov (1980) explains that, as a result of experimental evidence, the maximum equivalent stress σ_{eq} occurs at a certain depth under each surface. In particular, for line contact

$$\sigma_{eq,max} \cong 0.6p_{max} \quad (12.3.1)$$

To avoid yield, it must be verified that

$$\sigma_{eq,max} < R_e \quad (12.3.2)$$

i.e.

$$p_{max} < 1.6R_e \quad (12.3.3)$$

where $R_e = 800MPa$ is the yield strength of the steel and p_{max} is the maximum pressure generated at the contact surface.

The calculation can be done in a conservative way using the value of CF. If (12.3.3) is satisfied there is no need to repeat the proof for the case of N: being its modulus lower than the one of CF, also the resulting stresses will be lower. For the case of a cylindrical contact, by following the Hertzian theory, p_{max} can be computed as

$$p_{max} = \frac{2F}{\pi L b} \quad (12.3.4)$$

where the parameter b is the semi-width of the contact area; it can be calculated as

$$b = \sqrt{\frac{4}{\pi} \cdot \frac{F}{L} \cdot \frac{1}{2(\alpha_x + \beta_x)} \cdot \frac{1 - \nu_1^2}{E_1} \cdot \frac{1 - \nu_2^2}{E_2}} \quad (12.3.5)$$

α_x and β_x are the reciprocals of the curvature radii of the two bodies in contact, E and ν are respectively the Young and Poisson moduli. TABLE XVI summarizes the results obtained for the two values of the dead weights applied to the damper. The contact forces generated are not sufficient to reach the yielding condition.

TABLE XVI

COMPARISON BETWEEN MAXIMUM PRESSURE GENERATED AND YIELD LIMIT

m [kg]	CF [N]	p_{max} [N/mm ²]	$1,6R_e$ [N/mm ²]
5	49.05	112.5	1280
15	147.15	194.8	1280

13 FORCED RESPONSE CALCULATION METHOD

13.1 Bladed disk equilibrium equation

According to Zucca et al. (2012a) and Frrone and Zucca (2011), the balance equation of the FE model of a turbine bladed disk in the time domain is:

$$M\ddot{u}^*(t) + C\dot{u}^*(t) + Ku^*(t) = F_E(t) - F_C(t) \quad (13.1.1)$$

where M , C , K are the mass, damping stiffness matrices of the system respectively, u^* is the displacement vector of the bladed disk, F_E is an engine-order-type harmonic excitation and F_C is the vector of nonlinear forces applied by the blade platforms to the cylindrical underplatform dampers (notice the minus sign).

Being periodical the external excitation, the HBM can be used to compute the solution of the system. Displacement and forces can be expressed with a Fourier series:

$$u^*(t) = u^{*0} + \text{R} \left(\sum_{n=1}^{Nh} u^{*(n)} e^{in\omega t} \right) \quad (13.1.2)$$

$$F_E = F_E^{(0)} + \text{R} \left(\sum_{n=1}^{Nh} F_E^{(n)} e^{in\omega t} \right) \quad (13.1.3)$$

$$F_C = F_C^{(0)} + \text{R} \left(\sum_{n=1}^{Nh} F_C^{(n)} e^{in\omega t} \right) \quad (13.1.4)$$

where Nh is the considered number of harmonics and ω is the frequency of the excitation forces. By substituting equations (13.1.2)-(13.1.3)-(13.1.4) into the general balance

equation (13.1.1), in the frequency domain the initial nonlinear second order differential equations are turned into a set of nonlinear algebraic complex equations

$$D(\omega)^{(n)}u^{*(n)} = F_E^{(n)} - F_C^{(n)} \text{ with } n = 0 \dots Nh \quad (13.1.5)$$

where $D^{(n)} = -(n\omega)^2M + in\omega C + K$ is the n^{th} dynamic stiffness matrix of the bladed disk.

13.2 Underplatform damper equilibrium equation

The FE model of the UPD has to be consistent with the bladed disk one: they must have coincident nodes at the contact interfaces. The differential equilibrium equation of the damper is:

$$M_D \ddot{u}(t) + C_D \dot{u}(t) + K_D u(t) = F_{centr} + F_C(t) \quad (13.2.1)$$

where M_D , C_D and K_D are the mass, damping and stiffness matrices of the damper, u is the damper displacement vector, F_{centr} is the centrifugal force and F_C is the vector of nonlinear forces applied by the platform to the damper (Zucca et al., 2012b).

By following the same procedure carried out for the bladed disk case, the following equilibrium equation in the frequency domain is obtained:

$$D_D(\omega)^{(n)}u^{(n)} = F_{centr} + F_C^{(n)} \text{ with } n = 0 \dots Nh \quad (13.2.2)$$

where $D_D^{(n)} = -(n\omega)^2M_D + in\omega C_D + K_D$ is the n^{th} dynamic stiffness matrix of the damper. In order to solve equations (13.1.5) and (13.2.2), a contact model must be introduced because the contact forces F_C are unknown. In addition, given that the contact forces depend on the relative displacement between damper and blade

platforms, the nature of the algebraic equations (13.1.5) and (13.2.2) obtained in the frequency domain is nonlinear. As a consequence, an iterative method like the Newton-Raphson solver must be used.

13.3 Coordinate systems adopted

It is convenient to identify two main coordinate systems for studying the dynamic behavior of the underplatform damper (see Figure 52). The global coordinate system is shown in black, it has its origin in the damper center of mass and it is used as a reference to write the damper equilibrium equations; the local coordinate system is shown in red, it is defined at each contact node and it is used to analyze the contact forces.

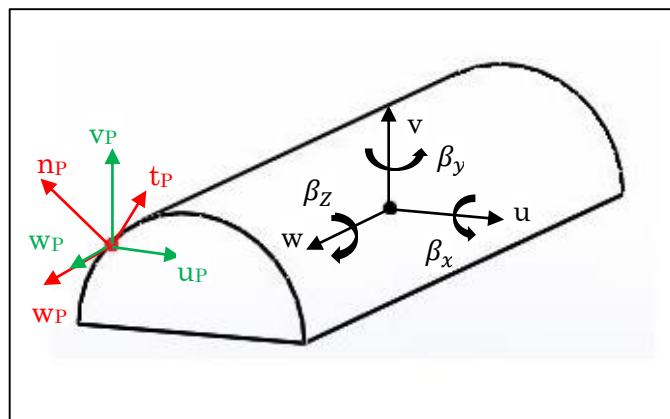


Figure 52. UPD coordinate systems.

To sum up, the damper displacement vector can be represented in three different forms:

- $\mathbf{u} = \{u, v, w, \beta_x, \beta_y, \beta_z\}$ is the displacement vector of the damper barycenter, it is characterized by 6 degrees of freedom, i.e. three rotations and three translations. It is expressed in global coordinates.
- $\mathbf{u}_p = \{u_p, v_p, w_p\}$ is the displacement vector of each contact point of the damper expressed in global coordinates.
- $\mathbf{t}_p = \{t_p, n_p, w_p\}$ is the displacement vector of each contact point of the damper expressed in local coordinates.

The relationship between the two coordinate systems is expressed by the following equations:

$$\mathbf{u}_p = T_s^T \mathbf{u} \quad (13.3.1)$$

$$\mathbf{t}_p = R \mathbf{u}_p \quad (13.3.2)$$

where the transformation matrix T_s allows to go from the center of mass to the contact point P and matrix R rotates the axes from the global to the local configuration. By combining (13.3.1) and (13.3.2) it follows

$$\mathbf{t}_p = R T_s^T \mathbf{u} \quad (13.3.3)$$

In accordance to (13.3.3), once the displacement of the damper barycenter \mathbf{u}_D is known, it is possible to calculate the displacement at each contact point. As an example, for a point belonging to the right damper contact line it holds:

$$\mathbf{t}_{P,right} = \begin{bmatrix} \mathbf{t}_{R,x} & \mathbf{t}_{R,y} & \mathbf{t}_{R,z} \\ \mathbf{n}_{R,x} & \mathbf{n}_{R,y} & \mathbf{n}_{R,z} \\ \mathbf{w}_{R,x} & \mathbf{w}_{R,y} & \mathbf{w}_{R,z} \end{bmatrix} \begin{bmatrix} 1 & 0 & 0 \\ 0 & 1 & 0 \\ 0 & 0 & 1 \\ 0 & -z_p & y_p \\ z_p & 0 & -x_p \\ -y_p & x_p & 0 \end{bmatrix}^T \mathbf{u} \quad (13.3.4)$$

where (x_p, y_p, z_p) are the global coordinates of the contact point considered, with respect to the damper center of mass. The entries of the rotation matrix R are the Cartesian coordinates of the versors t, n, w introduced in Section 8.2. Being (3×3) , (6×3) , (6×1) the dimensions of R , T s and u respectively, the dimension of vector $\mathbf{t}_{p,right}$ is (3×1) .

13.4 Damper free body diagram

The contact forces acting on the damper $\mathbf{T} = \{T, N, W\}$ are calculated through a contact model, which requires as input parameters the values of the contact stiffnesses, the friction coefficient and the imposed platform displacements. The contact forces developed, are different at each contact point, hence the subscript p must be introduced: $\mathbf{T}_p = \{T_p, N_p, W_p\}$. On the other hand, the centrifugal force can be easily calculated because it depends on the dead weight applied on the damper, namely $\mathbf{F}_{centr} = \{0, CF, 0, 0, 0, 0\}$ (see Figure 53).

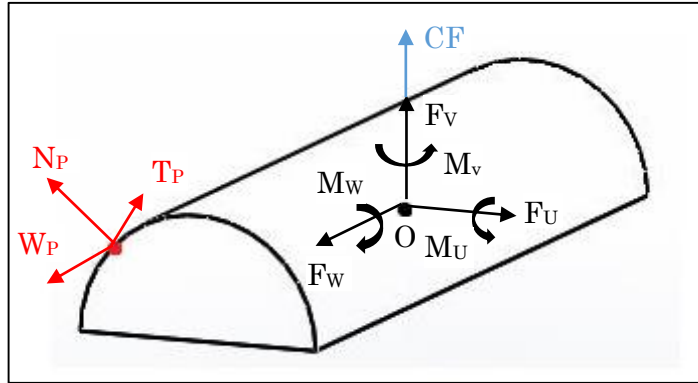


Figure 53. Forces acting on the damper.

The contact forces at each contact point are transformed and summed to obtain the resultant at the mass center $\mathbf{F}_C = \{F_U, F_V, F_W, M_U, M_V, M_W\}$:

$$\mathbf{F}_C = \sum_{p=1}^{N_{cp}} (T S_p R_p^T) \cdot \mathbf{T}_p \quad (13.4.1)$$

where N_{cp} is the number of contact points.

13.5 Simplified damper equilibrium equation

Given the geometry of the turbine bladed disk, the numerical code is a useful tool to properly design the underplatform damper and to optimize its damping capability. At the beginning of the design stage, the damper is treated as a rigid body because its geometry is unknown. As a consequence, the whole mass is concentrated in its barycenter and its stiffness and damping matrices can be neglected.

The damper equilibrium equation with respect to the general coordinate system can be expressed in the time domain as:

$$M\ddot{\mathbf{u}}(t) = \mathbf{F}_C(t) + \mathbf{F}_{centr} \quad (13.5.1)$$

where $\mathbf{u}(t) = \{u(t), v(t), w(t), \beta_x(t), \beta_y(t), \beta_z(t)\}^T$ is the displacement vector of the center of mass, $\mathbf{F}_C(t)$ is the vector of components of the resultant of the contact forces at the mass center, $\mathbf{F}_{centr} = \{0, CF, 0, 0, 0, 0\}$ is the vector of components of the external forces. M is the damper mass matrix, expressed as

$$M = \begin{bmatrix} m_D & 0 & 0 & 0 & 0 & 0 \\ 0 & m_D & 0 & 0 & 0 & 0 \\ 0 & 0 & m_D & 0 & 0 & 0 \\ 0 & 0 & 0 & I_x & 0 & 0 \\ 0 & 0 & 0 & 0 & I_y & 0 \\ 0 & 0 & 0 & 0 & 0 & I_z \end{bmatrix} \quad (13.5.2)$$

where m_D is the damper mass and I_x, I_y, I_z are its moments of inertia.

Forces and displacements can be expressed through Fourier series as follows:

$$\mathbf{u}(t) = \mathbf{u}^0 + \sum_{n=1}^{Nh} \mathbf{u}^{n,C} \cos(n\omega t) + \mathbf{u}^{n,S} \sin(n\omega t) \quad (13.5.3)$$

$$\mathbf{F}_C(\mathbf{u}, t) = \mathbf{F}_C(\mathbf{u})^0 + \sum_{n=1}^{Nh} \mathbf{F}_C(\mathbf{u})^{n,C} \cos(n\omega t) + \mathbf{F}_C(\mathbf{u})^{n,S} \sin(n\omega t) \quad (13.5.4)$$

$$\mathbf{F}_{centr} = \mathbf{F}_{centr}^0 \quad (13.5.5)$$

The centrifugal force is static, hence only the zero order harmonic appears. As a result, the equilibrium equations in the frequency domain become:

$$\mathbf{F}_C^0 + \mathbf{F}_{centr} = 0 \quad (13.5.6)$$

$$-(k\omega)^2 M \mathbf{u}^{k,C} = \mathbf{F}_C(\mathbf{u})^{k,C} \quad \text{with } k = 1, \dots, N_H \quad (13.5.7)$$

$$-(k\omega)^2 M \mathbf{u}^{k,S} = \mathbf{F}_C(\mathbf{u})^{k,S} \quad \text{with } k = 1, \dots, N_H \quad (13.5.8)$$

where N_H is the number of harmonics considered and ω is the frequency of the imposed platform displacement.

13.6 Solution method

The method used to solve the system of nonlinear algebraic equations (13.5.7)-(13.5.8) was proposed by Borrajo et al. (2012a) and by Firrone et al. (2011b) :

1. Make an initial guess of the vectors $\mathbf{u}^0, \mathbf{u}^{k,C}, \mathbf{u}^{k,S}$ with $k=0, \dots, N_H$;
2. Transform the vectors $\mathbf{u}^0, \mathbf{u}^{k,C}, \mathbf{u}^{k,S}$ into the time domain using (13.5.3)
3. $\mathbf{u}(t)$ is defined in the local coordinate system $\mathbf{t}_p(t)$ using (13.3.3);
4. Local displacement vectors $\mathbf{t}_p(t)$ for each contact point and platform displacements are given as input to the contact model;
5. The contact model calculates for each contact point $\mathbf{T}_p(t)$;
6. The resultant of all contact forces on the damper center of mass $\mathbf{F}(t)$ is computed with (13.4.1);
7. The vector of contact forces $\mathbf{F}_C(t)$ is decomposed in its frequency equivalents $\mathbf{F}_C(\mathbf{u})^0, \mathbf{F}_C(\mathbf{u})^{n,C}, \mathbf{F}_C(\mathbf{u})^{n,S}$ with (13.5.4);

8. The residuals are computed as:

$$\begin{aligned}\mathbf{r}^0 &= \mathbf{F}_{centr}^0 + \mathbf{F}_C(\mathbf{u})^0 \\ \mathbf{r}^{n,C} &= (n\omega)^2 M\mathbf{u}^{n,C} + \mathbf{F}_C(\mathbf{u})^{n,C} \\ \mathbf{r}^{n,S} &= (n\omega)^2 M\mathbf{u}^{n,S} + \mathbf{F}_C(\mathbf{u})^{n,S}\end{aligned}$$

9. If the values of the residuals are below a previously defined limit the solution is acceptable, otherwise the procedure is repeated again starting from step 1;

13.7 Jacobian matrix definition

The set of nonlinear equations resulting from the application of the harmonic balance method can be solved with an iterative procedure like the Newton-Raphson method. As an example, it was shown by Borrajo et al. (2012b) that the approximate solution at the i -th step can be estimated as:

$$\mathbf{u}_i = \mathbf{u}_{i-1} - \mathbf{J}_i^{-1} \mathbf{r}_{i-1} \quad (13.7.1)$$

where

- $\mathbf{u}_i = \{\mathbf{u}^0, \mathbf{u}^{1,C}, \mathbf{u}^{1,S}, \dots, \mathbf{u}^{N_H,S}\}'$ is the response vector at the i -th iteration.
- $\mathbf{r}_{i-1} = \{\mathbf{r}^0, \mathbf{r}^{1,C}, \mathbf{r}^{1,S}, \dots, \mathbf{r}^{N_H,S}\}'$ is the residue vector at the i -th iteration.
- \mathbf{J}_i is the Jacobian matrix at the i -th iteration:

$$J_{l,m,i} = \frac{\delta r_{l,i-1}}{\delta u_m} \quad (13.7.2)$$

By examining the expression of the residuals, it is possible to notice that the evaluation of the Jacobian matrix always requires the calculation of the term:

$$\frac{\partial \mathbf{F}_C}{\partial \mathbf{u}} \quad (13.7.3)$$

If the Jacobian matrix is calculated numerically through a finite difference procedure, a significant amount of time is required because the residual is calculated for one degree of freedom at a time, and each contact point has three degrees of freedom. As a result, the computational time increases considerably with the number of contact degrees of freedom (Borrajo et al., 2012c).

Cardona et al. (1991) introduced an alternative method, completely analytical, for the calculation of the Jacobian matrix that dramatically reduces the computational time. In particular, Petrov and Ewins (2003) applied this method to underplatform dampers.

Since the *Octopus* numerical code, once validated, will be used in terms of UPDs design, the computational time must be reduced. In the next chapter, the procedure for the analytical calculation of the Jacobian matrices for both the bladed disk and the UPDs is shown.

14 ANALYTICAL CALCULATION OF THE JACOBIAN MATRIX

14.1 List of symbols used in the chapter

- $\mathbf{t}_D = \{t_D, n_D, w_D\}$ is the vector of components of the displacement of a damper contact point expressed in local coordinates.
- $\mathbf{u} = \{u, v, w, \beta_x, \beta_y, \beta_z\}$ is the displacement vector of the damper barycenter, it is characterized by 6 degrees of freedom, i.e. three rotations and three translations. It is expressed in global coordinates.
- $\mathbf{t}^* = \{t^*, n^*, w^*\}$ is the vector of components of the displacement of a platform contact point expressed in local coordinates.

- $\mathbf{u}^* = \left\{ \begin{matrix} \mathbf{u}^{*Real} \\ \mathbf{u}^{*Imag} \end{matrix} \right\} = \left\{ \begin{matrix} u^{*Real} \\ v^{*Real} \\ w^{*Real} \\ u^{*Imag} \\ v^{*Imag} \\ w^{*Imag} \end{matrix} \right\}_p$ is the vector of components of the displacement of a

platform contact point, expressed in global coordinates.

- $\mathbf{t}_{rel} = \{t_{rel}, n_{rel}, w_{rel}\}$ is the vector of components of the local relative displacements $t_{rel} = t^* - t_D$, $n_{rel} = n^* - n_D$, $w_{rel} = w^* - w_D$ at a given contact point.
- M is the damper mass matrix.
- M_B is the bladed disk mass matrix.
- K_B is the bladed disk stiffness matrix.

- C_B is the bladed disk damping matrix.
- $D_B = -(n\omega)^2 M_B + in\omega C_B + K_B$ is the dynamic stiffness matrix of the blade.
- R rotation matrix. It rotates the reference system from the global to the local configuration.
- T 's transformation matrix. It allows to go from the center of mass to the contact point P of the damper.
- ϕ is the phase shift matrix.
- N_H is the number of harmonics.
- $\mathbf{T}_P = \{T, N, W\}$ is the vector of components of the contact forces acting on the damper at a given point in local coordinates.
- $\mathbf{F}_C = \{F_U, F_V, F_W, M_U, M_V, M_W\}$ is the vector of components of the resultant of the contact forces at the damper mass center, in global coordinates.
- $\mathbf{F}_{centr} = \{0, CF, 0, 0, 0, 0\}$ vector of the external forces acting on the damper barycenter, in global coordinates.

- $\mathbf{F}_{blade} = \begin{Bmatrix} \mathbf{F}_{blade}^R \\ \mathbf{F}_{blade}^{Im} \end{Bmatrix} = \begin{Bmatrix} F_{U,blade}^R \\ F_{V,blade}^R \\ F_{W,blade}^R \\ F_{U,blade}^{Im} \\ F_{V,blade}^{Im} \\ F_{W,blade}^{Im} \end{Bmatrix}$ is the vector of contact forces acting at each

contact point of the blade.

- r is the residual.
- J_B is the Jacobian matrix of the bladed disk.
- J_D is the Jacobian matrix of the underplatform damper.
- $K^* = \frac{\delta \mathbf{T}_P}{\delta(t^* - t_D)}$

- $KK^* =$

K_1^{*RR}	K_1^{*RI}	0	0	0	0
K_1^{*IR}	K_1^{*II}	0	0	0	0
0	0	K_2^{*RR}	K_2^{*RI}	0	0
0	0	K_2^{*IR}	K_2^{*II}	0	0
0	0	0	0	K_3^{*RR}	K_3^{*RI}
0	0	0	0	K_3^{*IR}	K_3^{*II}

- $RR =$

R1	0	0	0	0	0
0	R1	0	0	0	0
0	0	R2	0	0	0
0	0	0	R2	0	0
0	0	0	0	R3	0
0	0	0	0	0	R3

- $TT =$

$Ts, 1$	0	$Ts, 2$	0	$Ts, 3$	0
0	$Ts, 1$	0	$Ts, 2$	0	$Ts, 3$

The damper coordinate systems and the scheme of the contact forces are here recalled to make it easier the understanding of the following sections (see Figure 54 and Figure 55).

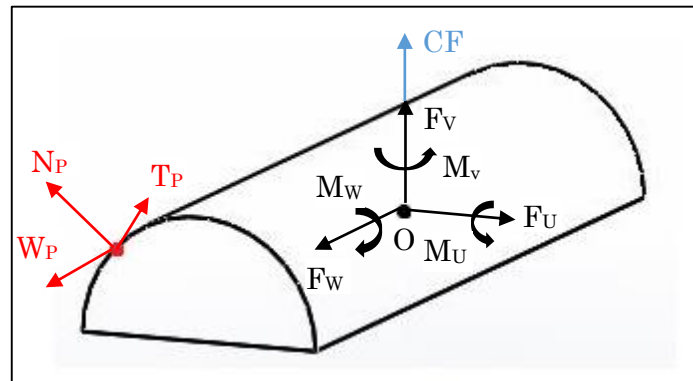


Figure 54. Forces acting on the damper.

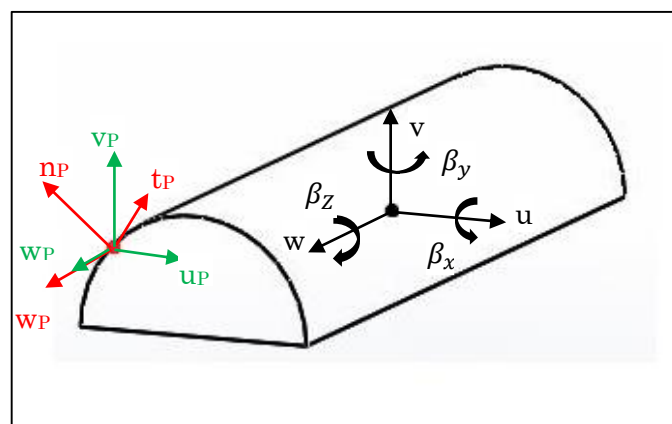


Figure 55. UPD coordinate systems.

14.2 Input of the existing numerical code

The *Octopus* numerical code calculates for each contact point the expression of the derivative of the local contact forces with respect to the local relative displacements between damper and platform:

$$\frac{\delta \mathbf{T}_P}{\delta(\mathbf{t}^* - \mathbf{t}_D)} \quad (14.2.1)$$

where $\mathbf{T}_P = \{T, N, W\}$ is the vector of components of the contact forces acting on the damper at a given point in local coordinates, $\mathbf{t}_D = \{t_D, n_D, w_D\}$ is the vector of components of the displacement of a damper contact point expressed in local coordinates, $\mathbf{t}^* = \{t^*, n^*, w^*\}$ is the vector of components of the displacement of a platform contact point expressed in local coordinates.

Equation (14.2.1) is actually a matrix of dimension $3 \times 2 \times (N_H + 1)$, where $N_H = 1 \dots n$ is the number of harmonics considered. As an example, if $N_H = 2$, the matrix structure becomes:

$\frac{\partial \mathbf{T}_P^0}{\partial \mathbf{t}_{rel}^0}$	$\frac{\partial \mathbf{T}_P^0}{\partial \mathbf{t}_{rel}^1}$	$\frac{\partial \mathbf{T}_P^0}{\partial \mathbf{t}_{rel}^2}$	(14.2.2)
$\frac{\partial \mathbf{T}_P^1}{\partial \mathbf{t}_{rel}^0}$	$\frac{\partial \mathbf{T}_P^1}{\partial \mathbf{t}_{rel}^1}$	$\frac{\partial \mathbf{T}_P^1}{\partial \mathbf{t}_{rel}^2}$	
$\frac{\partial \mathbf{T}_P^2}{\partial \mathbf{t}_{rel}^0}$	$\frac{\partial \mathbf{T}_P^2}{\partial \mathbf{t}_{rel}^1}$	$\frac{\partial \mathbf{T}_P^2}{\partial \mathbf{t}_{rel}^2}$	

where $\mathbf{t}_{rel} = \{t_{rel}, n_{rel}, w_{rel}\}$ is the vector of components of the local relative displacements $t_{rel} = t^* - t_D$, $n_{rel} = n^* - n_D$, $w_{rel} = w^* - w_D$ at a given contact point.

The dimension of each sub-square is 6×6 .

In the particular case of a sticking working condition, the relationship between contact forces and displacements is linear. As a consequence there is no influence between forces and displacements with a different harmonic index and the out-of-diagonal squares of the matrix go to zero

$\frac{\partial T_p^0}{\partial t_{rel}^0}$	0	0
0	$\frac{\partial T_p^1}{\partial t_{rel}^1}$	0
0	0	$\frac{\partial T_p^2}{\partial t_{rel}^2}$

(14.2.3)

The 6x6 sub-matrix associated to the zero harmonic index for both forces and relative displacements has the form

$$\begin{bmatrix}
 \frac{\partial \text{Re} T_p^0}{\partial \text{Re} t_{rel}^0} & \frac{\partial \text{Re} T_p^0}{\partial \text{Im} t_{rel}^0} & \frac{\partial \text{Re} T_p^0}{\partial \text{Re} n_{rel}^0} & \frac{\partial \text{Im} T_p^0}{\partial \text{Re} n_{rel}^0} & \frac{\partial \text{Re} T_p^0}{\partial \text{Re} w_{rel}^0} & \frac{\partial \text{Im} T_p^0}{\partial \text{Re} w_{rel}^0} \\
 \frac{\partial \text{Re} t_{rel}^0}{\partial \text{Re} T_p^0} & \frac{\partial \text{Im} t_{rel}^0}{\partial \text{Re} T_p^0} & \frac{\partial \text{Re} n_{rel}^0}{\partial \text{Re} T_p^0} & \frac{\partial \text{Im} n_{rel}^0}{\partial \text{Re} T_p^0} & \frac{\partial \text{Re} w_{rel}^0}{\partial \text{Re} T_p^0} & \frac{\partial \text{Im} w_{rel}^0}{\partial \text{Re} T_p^0} \\
 \frac{\partial \text{Im} T_p^0}{\partial \text{Re} t_{rel}^0} & \frac{\partial \text{Im} T_p^0}{\partial \text{Im} t_{rel}^0} & \frac{\partial \text{Im} T_p^0}{\partial \text{Re} n_{rel}^0} & \frac{\partial \text{Im} T_p^0}{\partial \text{Im} n_{rel}^0} & \frac{\partial \text{Im} T_p^0}{\partial \text{Re} w_{rel}^0} & \frac{\partial \text{Im} T_p^0}{\partial \text{Im} w_{rel}^0} \\
 \frac{\partial \text{Re} t_{rel}^0}{\partial \text{Im} T_p^0} & \frac{\partial \text{Im} t_{rel}^0}{\partial \text{Im} T_p^0} & \frac{\partial \text{Re} n_{rel}^0}{\partial \text{Im} T_p^0} & \frac{\partial \text{Im} n_{rel}^0}{\partial \text{Im} T_p^0} & \frac{\partial \text{Re} w_{rel}^0}{\partial \text{Im} T_p^0} & \frac{\partial \text{Im} w_{rel}^0}{\partial \text{Im} T_p^0} \\
 \frac{\partial \text{Re} N_p^0}{\partial \text{Re} t_{rel}^0} & \frac{\partial \text{Re} N_p^0}{\partial \text{Im} t_{rel}^0} & \frac{\partial \text{Re} N_p^0}{\partial \text{Re} n_{rel}^0} & \frac{\partial \text{Re} N_p^0}{\partial \text{Im} n_{rel}^0} & \frac{\partial \text{Re} N_p^0}{\partial \text{Re} w_{rel}^0} & \frac{\partial \text{Re} N_p^0}{\partial \text{Im} w_{rel}^0} \\
 \frac{\partial \text{Im} N_p^0}{\partial \text{Re} t_{rel}^0} & \frac{\partial \text{Im} N_p^0}{\partial \text{Im} t_{rel}^0} & \frac{\partial \text{Im} N_p^0}{\partial \text{Re} n_{rel}^0} & \frac{\partial \text{Im} N_p^0}{\partial \text{Im} n_{rel}^0} & \frac{\partial \text{Im} N_p^0}{\partial \text{Re} w_{rel}^0} & \frac{\partial \text{Im} N_p^0}{\partial \text{Im} w_{rel}^0} \\
 \frac{\partial \text{Re} t_{rel}^0}{\partial \text{Re} W_p^0} & \frac{\partial \text{Im} t_{rel}^0}{\partial \text{Re} W_p^0} & \frac{\partial \text{Re} n_{rel}^0}{\partial \text{Re} W_p^0} & \frac{\partial \text{Im} n_{rel}^0}{\partial \text{Re} W_p^0} & \frac{\partial \text{Re} w_{rel}^0}{\partial \text{Re} W_p^0} & \frac{\partial \text{Im} w_{rel}^0}{\partial \text{Re} W_p^0} \\
 \frac{\partial \text{Re} W_p^0}{\partial \text{Re} t_{rel}^0} & \frac{\partial \text{Re} W_p^0}{\partial \text{Im} t_{rel}^0} & \frac{\partial \text{Re} W_p^0}{\partial \text{Re} n_{rel}^0} & \frac{\partial \text{Re} W_p^0}{\partial \text{Im} n_{rel}^0} & \frac{\partial \text{Re} W_p^0}{\partial \text{Re} w_{rel}^0} & \frac{\partial \text{Re} W_p^0}{\partial \text{Im} w_{rel}^0} \\
 \frac{\partial \text{Im} W_p^0}{\partial \text{Re} t_{rel}^0} & \frac{\partial \text{Im} W_p^0}{\partial \text{Im} t_{rel}^0} & \frac{\partial \text{Im} W_p^0}{\partial \text{Re} n_{rel}^0} & \frac{\partial \text{Im} W_p^0}{\partial \text{Im} n_{rel}^0} & \frac{\partial \text{Im} W_p^0}{\partial \text{Re} w_{rel}^0} & \frac{\partial \text{Im} W_p^0}{\partial \text{Im} w_{rel}^0} \\
 \frac{\partial \text{Re} t_{rel}^0}{\partial \text{Im} W_p^0} & \frac{\partial \text{Im} t_{rel}^0}{\partial \text{Im} W_p^0} & \frac{\partial \text{Re} n_{rel}^0}{\partial \text{Im} W_p^0} & \frac{\partial \text{Im} n_{rel}^0}{\partial \text{Im} W_p^0} & \frac{\partial \text{Re} w_{rel}^0}{\partial \text{Im} W_p^0} & \frac{\partial \text{Im} w_{rel}^0}{\partial \text{Im} W_p^0}
 \end{bmatrix}$$
(14.2.4)

14.3 Jacobian matrix of the damper

By definition, the Jacobian matrix is the derivative of the residual with respect to the displacement. The residual for the damper system can be calculated starting from the equilibrium equation as

$$r = -D_D \mathbf{u} + \mathbf{F}_C + \mathbf{F}_{centr} \quad (14.3.1)$$

where \mathbf{F}_C is the resultant on the damper barycenter of the contact forces expressed in global coordinates and $D_D = -(n\omega)^2 M_D$ is the dynamic stiffness matrix of the damper. In particular, being the damper modeled as a rigid body, its damping and stiffness matrices have been neglected. The expression of the damper Jacobian matrix J_D is the following:

$$J_D = \frac{\partial r}{\partial \mathbf{u}} = -D_D + \frac{\partial \mathbf{F}_C}{\partial \mathbf{u}} \quad (14.3.2)$$

notice that, being \mathbf{F}_{centr} a constant force, its derivative is null.

Matrix $\frac{\partial \mathbf{F}_C}{\partial \mathbf{u}}$ can be obtained starting from matrix $\frac{\partial \mathbf{T}_p}{\partial \mathbf{t}_D}$ and applying the following transformation:

$$\frac{\partial \mathbf{F}_C}{\partial \mathbf{u}} = \sum_{p=1}^{N_{cp}} T_{S_P} R_P^T \left(\frac{\partial \mathbf{T}}{\partial \mathbf{t}_D} \right)_p R_P T_{S_P}^T \quad (14.3.3)$$

as a consequence, the expression of $\frac{\partial \mathbf{T}_p}{\partial \mathbf{t}_D}$ has to be found at each contact point.

First of all, matrix $\frac{\partial \mathbf{T}_p}{\partial \mathbf{t}_D}$ can be expressed as a function of the input matrix calculated by the *Octopus* numerical code as

$$\frac{\partial \mathbf{T}_p}{\partial (\mathbf{t}_D)} = \frac{\partial \mathbf{T}_p}{\partial (\mathbf{t}^* - \mathbf{t}_D)} \frac{\partial (\mathbf{t}^* - \mathbf{t}_D)}{\partial \mathbf{t}_D} \quad (14.3.4)$$

The displacement of the blade platform \mathbf{t}^* is seen by the damper as a constant external excitation; for this reason, it follows that

$$\frac{\partial(\mathbf{t}^* - \mathbf{t}_D)}{\partial \mathbf{t}_D} = -1 \quad (14.3.5)$$

hence

$$\frac{\partial \mathbf{T}_p}{\partial(\mathbf{t}_D)} = - \frac{\partial \mathbf{T}_p}{\partial(\mathbf{t}^* - \mathbf{t}_D)} \quad (14.3.6)$$

It is convenient to redefine equation (14.3.6) as a local Jacobian matrix J_{local} , which has to be calculated for each contact point, namely

$$J_{local} = \frac{\partial \mathbf{T}_p}{\partial \mathbf{t}_{D,p}} \quad (14.3.7)$$

The contact forces developed at a given point (subscript p) can be written as

$$d\mathbf{T}_p = J_{local} \cdot d\mathbf{t}_{D,p} \quad (14.3.8)$$

By recalling (13.4.1), it follows that

$$d\mathbf{F}_C = \sum_{p=1}^{N_{cp}} (T S_p R_p^T) \cdot d\mathbf{T}_p \quad (14.3.9)$$

Introducing (14.3.8) it follows

$$d\mathbf{F}_C = \sum_{p=1}^{N_{cp}} (T S_p R_p^T) J_{local} \cdot d\mathbf{t}_{D,p} \quad (14.3.10)$$

The local displacement $d\mathbf{t}_{D,p}$ can be expressed as a function of \mathbf{u} through the rotation matrix R and the transformation matrix T , namely $d\mathbf{t}_{D,p} = R_p T S_p^T d\mathbf{u}$.

therefore

$$d\mathbf{F}_C = \sum_{p=1}^{N_{cp}} (T_{S_P} R_P^T) J_{local} \cdot R_P T_{S_P}^T d\mathbf{u} \quad (14.3.11)$$

Being \mathbf{u} the displacement of the damper center of mass, it can be collected out of the summation and used to divide the term $d\mathbf{F}_C$:

$$\frac{\delta\mathbf{F}_C}{\delta\mathbf{u}} = \sum_{p=1}^{N_{cp}} (T_{S_P} R_P^T) J_{local} \cdot R_P T_{S_P}^T \quad (14.3.12)$$

Finally, the expression of the damper Jacobian matrix is

$$J_D = -D_D + \frac{\partial\mathbf{F}_C}{\partial\mathbf{u}} = -D_D + \sum_{p=1}^{N_{cp}} T_{S_P} R_P^T \cdot J_{local} \cdot R_P T_{S_P}^T \quad (14.3.13)$$

The dimension of J_D is $6*2*(N_H+1)$. The underplatform damper is not directly excited by a periodical external excitation, but by a composition of imposed platform displacements at the contact points; as a consequence more harmonic indexes have been considered. It has been demonstrated that for the Octopus test rig, 5 harmonics are sufficient to guarantee an accurate damper calculation.

14.4 **Jacobian matrix of the blade**

By definition, the Jacobian matrix is the derivative of the residual with respect to the displacement.

The residual for the blade system can be calculated starting from the equilibrium equation as

$$r = -D_B \mathbf{u}^* + \mathbf{F}_E + \mathbf{F}_{blade} \quad (14.4.1)$$

where \mathbf{F}_{blade} is the vector of contact forces acting at each contact point of the blade expressed in global coordinates and $D_B = -(n\omega)^2 M_B + in\omega C_B + K_B$ is the dynamic stiffness matrix of the blade. The expression of the blade Jacobian matrix J_B is:

$$J_B = \frac{\partial r}{\partial \mathbf{u}^*} = -D_B + \frac{\partial \mathbf{F}_{blade}}{\partial \mathbf{u}^*} \quad (14.4.2)$$

notice that, being \mathbf{F}_E independent from \mathbf{u}^* , its derivative is null.

The starting point of the calculation is the matrix computed for each contact point by the *Octopus* numerical code

$$\frac{\partial \mathbf{T}_p}{\partial (\mathbf{t}^* - \mathbf{t}_D)} \quad (14.4.3)$$

As in the case of the damper Jacobian matrix, in order to calculate $\frac{\partial \mathbf{F}_{blade}}{\partial \mathbf{u}^*}$, it would be useful to isolate the term

$$\frac{\partial \mathbf{T}_p}{\partial (\mathbf{t}^*)} \quad (14.4.4)$$

however, it must be noticed that

$$\frac{\partial \mathbf{T}_p}{\partial (\mathbf{t}^* - \mathbf{t}_D)} \neq \frac{\partial \mathbf{T}_p}{\partial (\mathbf{t}^*)} \quad (14.4.5)$$

The main reason why the term at the left side is different from the right one is that, being \mathbf{t}_D a function of \mathbf{t}^* , i.e. $\mathbf{t}_D = f(\mathbf{t}^*)$, the derivative of \mathbf{t}_D with respect to \mathbf{t}^* is not zero, hence

$$\frac{\partial (\mathbf{t}^* - \mathbf{t}_D)}{\partial \mathbf{t}^*} \neq 1 \quad (14.4.6)$$

The physical explanation of this inequality is that the contact forces developed at a given contact point depend not only on the local displacement at that point but on the displacement of the entire platform.

In order to find the expression of the blade Jacobian matrix J_B , by neglecting the external forces \mathbf{F}_E , the residual can be rewritten as

$$r = -D_B \mathbf{u}^* + \mathbf{F}_{blade} = \frac{\partial r}{\partial \mathbf{u}^*} \mathbf{u}^* = J_B \mathbf{u}^* \quad (14.4.7)$$

hence it is enough to express the contact forces \mathbf{F}_{blade} as a function of \mathbf{u}^* .

By recalling the concept of phase shift between contact forces introduced in Section 1.4, the relationship between the forces acting on two adjacent blades is

$$\mathbf{F}_{blade} = \phi^T \mathbf{F}_{blade}^{ad} \quad (14.4.8)$$

By taking into account only the harmonics 0 and 1, \mathbf{F}_{blade}^{ad} at a given contact point can be calculated as

$$\mathbf{F}_{blade}^{ad} = \begin{Bmatrix} \mathbf{F}_{blade}^{ad(0)} \\ \mathbf{F}_{blade}^{ad(1)} \end{Bmatrix} = \begin{bmatrix} \mathbf{R}^T \mathbf{K}^{*(0-0)} & \mathbf{R}^T \mathbf{K}^{*(0-1)} \\ \mathbf{R}^T \mathbf{K}^{*(1-0)} & \mathbf{R}^T \mathbf{K}^{*(1-1)} \end{bmatrix} \begin{Bmatrix} \mathbf{0} - \mathbf{t}_d^{(0)} \\ \mathbf{t}^{*(1)} - \mathbf{t}_d^{(1)} \end{Bmatrix} \quad (14.4.9)$$

where

$$\mathbf{K}^* = \frac{\partial \mathbf{T}_P}{\partial (\mathbf{t}^* - \mathbf{t}_D)} \quad (14.4.10)$$

The matrix \mathbf{K}^* has the dimension of a stiffness. The additional superscript of the form (number-number) refers to the harmonic order of force and displacement respectively. As an example, $\mathbf{K}^{*(1-0)}$ is related to the harmonic 1 of the force and to harmonic 0 of the displacement.

Hence, the harmonic components of \mathbf{F}_{blade}^{ad} are

$$\begin{Bmatrix} \mathbf{F}_{blade}^{ad(0)} \\ \mathbf{F}_{blade}^{ad(1)} \end{Bmatrix} = \begin{Bmatrix} -R^T K^{*(0-0)} \mathbf{t}_D^{(0)} + R^T K^{*(0-1)} (\mathbf{t}^{*(1)} - \mathbf{t}_D^{(1)}) \\ -R^T K^{*(1-0)} \mathbf{t}_D^{(0)} + R^T K^{*(1-1)} (\mathbf{t}^{*(1)} - \mathbf{t}_D^{(1)}) \end{Bmatrix} \quad (14.4.11)$$

It must be noticed that since the blade responds mainly to the fundamental harmonic (first order), only $\mathbf{F}_{blade}^{ad(1)}$ is taken into account. As a consequence, \mathbf{F}_{blade} can be rewritten as

$$\mathbf{F}_{blade}^{(1)} = \phi^T (-R^T K^{*(1-0)} \mathbf{t}_D^{(0)} + R^T K^{*(1-1)} \mathbf{t}^{*(1)} - R^T K^{*(1-1)} \mathbf{t}_D^{(1)}) \quad (14.4.12)$$

For simplicity, $\mathbf{F}_{blade}^{(1)}$ can be divided into the three components \mathbf{F}_1 , \mathbf{F}_2 and \mathbf{F}_3 :

$$\mathbf{F}_{blade}^{(1)} = \phi^T (-\mathbf{F}_3 + \mathbf{F}_1 - \mathbf{F}_2) \quad (14.4.13)$$

where $\mathbf{F}_1 = R^T K^{*(1-1)} \mathbf{t}^{*(1)}$, $\mathbf{F}_2 = R^T K^{*(1-1)} \mathbf{t}_D^{(1)}$ and $\mathbf{F}_3 = R^T K^{*(1-0)} \mathbf{t}_D^{(0)}$. In order to find the expression of the Jacobian matrix, each of them has to be expressed as a function of \mathbf{u}^* .

Starting from \mathbf{F}_1 it follows

$$\mathbf{F}_1 = R^T K^{*(1-1)} \mathbf{t}^{*(1)} = R^T K^{*(1-1)} R \mathbf{u}^{*,ad,(1)} = R^T K^{*(1-1)} R \phi \mathbf{u}^{*(1)} \quad (14.4.14)$$

Regarding \mathbf{F}_2 and \mathbf{F}_3 , the procedure is shown step by step for \mathbf{F}_2 only, because the case of \mathbf{F}_3 is analogous. In order to find the final expression of \mathbf{F}_2 , \mathbf{t}_D has to be written at first as a function of \mathbf{u}

$$\mathbf{F}_2 = R^T K^{*(1-1)} \mathbf{t}_D^{(1)} = R^T K^{*(1-1)} R T_S^T \mathbf{u}^{(1)} \quad (14.4.15)$$

Now \mathbf{u} has to be written as a function of \mathbf{u}^* . In order to fulfill this requirement, the starting point is the damper equilibrium equation

$$M \ddot{\mathbf{u}}(t) = \mathbf{F}_c(t) + \mathbf{F}_{centr} \quad (14.4.16)$$

Given that the blade directly undergoes a harmonic external excitation, only the harmonic number 1 terms (the fundamental harmonic) are taken into account. Hence the equilibrium equation can be expressed in the frequency domain as

$$-(\omega)^2 M \mathbf{u} = \mathbf{F}_c^{(1)} \quad (14.4.17)$$

It must be noticed that the centrifugal force, being static, is null when the harmonic index is different from zero. The contact force $\mathbf{F}_c^{(1)}$ can be rewritten as

$$\mathbf{F}_c^{(1)} = \frac{\partial \mathbf{F}_c^{(1)}}{\partial (\mathbf{u}^{*,ad} - \mathbf{u})} (\mathbf{u}^{*,ad} - \mathbf{u}) \quad (14.4.18)$$

hence

$$\left(-\omega^2 M - \frac{\partial \mathbf{F}_c^{(1)}}{\partial \mathbf{u}} \right) \mathbf{u} = - \frac{\partial \mathbf{F}_c^{(1)}}{\partial \mathbf{u}} \mathbf{u}^{*,ad} \quad (14.4.19)$$

Recalling equation (14.3.12) it follows

$$\left(\omega^2 M + \sum_{i=1}^{N_{CP}} T_{S_i} R_i^T \left(\frac{\partial \mathbf{T}}{\partial \mathbf{t}_D} \right)_i R_i T_{S_i}^T \right) \mathbf{u} = \sum_{i=1}^{N_{CP}} T_{S_i} R_i^T \left(\frac{\partial \mathbf{T}}{\partial \mathbf{t}_D} \right)_i R_i \mathbf{u}_i^{*,ad} \quad (14.4.20)$$

where $T_{S_i}^T \mathbf{u}_i^{*,ad} = \mathbf{u}_i^{*,ad}$.

The summation can be expressed in matrix form as

$$\omega^2 M \mathbf{u} + T T R R^T K K^* R R T^T \mathbf{u} = T T R R^T K K^* R R \mathbf{u}^{*,ad} \quad (14.4.21)$$

where, in an exemplifying case of three contact points it holds

$$T T = \begin{array}{|c|c|c|c|c|c|} \hline T_{S,1} & 0 & T_{S,2} & 0 & T_{S,3} & 0 \\ \hline 0 & T_{S,1} & 0 & T_{S,2} & 0 & T_{S,3} \\ \hline \end{array} \quad (14.4.22)$$

$$\mathbf{RR} = \begin{array}{|c|c|c|c|c|c|}
 \hline
 \mathbf{R1} & 0 & 0 & 0 & 0 & 0 \\
 \hline
 0 & \mathbf{R1} & 0 & 0 & 0 & 0 \\
 \hline
 0 & 0 & \mathbf{R2} & 0 & 0 & 0 \\
 \hline
 0 & 0 & 0 & \mathbf{R2} & 0 & 0 \\
 \hline
 0 & 0 & 0 & 0 & \mathbf{R3} & 0 \\
 \hline
 0 & 0 & 0 & 0 & 0 & \mathbf{R3} \\
 \hline
 \end{array} \tag{14.4.23}$$

$$\mathbf{KK}^* = \begin{array}{|c|c|c|c|c|c|}
 \hline
 K_1^{RR} & K_1^{RI} & 0 & 0 & 0 & 0 \\
 \hline
 K_1^{IR} & K_1^{II} & 0 & 0 & 0 & 0 \\
 \hline
 0 & 0 & K_2^{RR} & K_2^{RI} & 0 & 0 \\
 \hline
 0 & 0 & K_2^{IR} & K_2^{II} & 0 & 0 \\
 \hline
 0 & 0 & 0 & 0 & K_3^{RR} & K_3^{RI} \\
 \hline
 0 & 0 & 0 & 0 & K_3^{IR} & K_3^{II} \\
 \hline
 \end{array} \tag{14.4.24}$$

where a generic submatrix of \mathbf{RR} has dimension (3×3) , a submatrix of \mathbf{TT} has dimension (6×3) and a submatrix of \mathbf{KK}^* has dimension (3×3) .

By introducing the new parameter $A = \omega^2 M + TTRR^T KK^* RRTT^T$, with $B = \text{inv}(A)$, the final expression of \mathbf{u} as a function of \mathbf{u}^* can be found starting from

$$\mathbf{u} = BTTRR^T KK^* RRTT^T \mathbf{u}^* \tag{14.4.25}$$

In detail, introducing the harmonic components of the matrices B and K it follows that

$$\begin{Bmatrix} \mathbf{u}^{(0)} \\ \mathbf{u}^{(1)} \end{Bmatrix} = \begin{bmatrix} \mathbf{B}^{(0-0)} & \mathbf{B}^{(0-1)} \\ \mathbf{B}^{(1-0)} & \mathbf{B}^{(1-1)} \end{bmatrix} \begin{bmatrix} TTRR^T KK^{*(0-0)} RR & TTRR^T KK^{*(0-1)} RR \\ TTRR^T KK^{*(1-0)} RR & TTRR^T KK^{*(1-1)} RR \end{bmatrix} \begin{Bmatrix} 0 \\ \phi \cdot \mathbf{u}^{(1)*} \end{Bmatrix} \quad (14.4.26)$$

hence

$$\mathbf{u}^{(1)} = B^{(1-0)} TTRR^T KK^{*(0-1)} RR \phi \mathbf{u}^{*(1)} + B^{(1-1)} TTRR^T KK^{*(1-1)} RR \phi \mathbf{u}^{*(1)} \quad (14.4.27)$$

$$\mathbf{u}^{(0)} = B^{(0-0)} TTRR^T KK^{*(0-1)} RR \phi \mathbf{u}^{*(1)} + B^{(0-1)} TTRR^T KK^{*(1-1)} RR \phi \mathbf{u}^{*(1)} \quad (14.4.28)$$

The final expressions of \mathbf{F}_2 and \mathbf{F}_3 for all contact points is:

$$\begin{aligned} \mathbf{F}_2 = & RR^T KK^{*(1-1)} RRTT^T (B^{(1-0)} TTRR^T KK^{*(0-1)} RR \phi \\ & + B^{(1-1)} TTRR^T KK^{*(1-1)} RR \phi) \mathbf{u}^{*(1)} \end{aligned} \quad (14.4.29)$$

$$\begin{aligned} \mathbf{F}_3 = & RR^T KK^{*(1-0)} RRTT^T (B^{(0-0)} TTRR^T KK^{*(0-1)} RR \phi \\ & + B^{(0-1)} TTRR^T KK^{*(1-1)} RR \phi) \mathbf{u}^{*(1)} \end{aligned} \quad (14.4.30)$$

Consequently, the residual (F_E excluded) can be computed as a function of $\mathbf{u}^{*(1)}$

$$\begin{aligned} r = & -D_B \mathbf{u}^{*(1)} + \phi^T \left(- \left(RR^T KK^{*(1-0)} RRTT^T (B^{(0-0)} TTRR^T KK^{*(0-1)} RR \phi \right. \right. \\ & + B^{(0-1)} TTRR^T KK^{*(1-1)} RR \phi) \mathbf{u}^{*(1)} \\ & + RR^T KK^{*(1-1)} RR \phi \mathbf{u}^{*(1)} \\ & - \left(RR^T KK^{*(1-1)} RRTT^T (B^{(1-0)} TTRR^T KK^{*(0-1)} RR \phi \right. \\ & \left. \left. + B^{(1-1)} TTRR^T KK^{*(1-1)} RR \phi) \mathbf{u}^{*(1)} \right) \right) \end{aligned} \quad (14.4.31)$$

The final expression of the blade Jacobian matrix is

$$\begin{aligned}
J_B = -D_B + \phi^T & \left(- \left(RR^T KK^{*(1-0)} RRTT^T (B^{(0-0)} TTRR^T KK^{*(0-1)} RR\phi \right. \right. \\
& \left. \left. + B^{(0-1)} TTRR^T KK^{*(1-1)} RR\phi \right) \right) + RR^T KK^{*(1-1)} RR\phi \\
& - \left(RR^T KK^{*(1-1)} RRTT^T (B^{(1-0)} TTRR^T KK^{*(0-1)} RR\phi \right. \\
& \left. \left. + B^{(1-1)} TTRR^T KK^{*(1-1)} RR\phi \right) \right)
\end{aligned} \tag{14.4.32}$$

14.5 Saving in computational time achieved with the implementation of the analytical Jacobian matrices

The analytical calculation of the Jacobian matrix for both the blade and the damper has been implemented on the *Octopus* numerical code achieving significant reduction of the computational time. The saving in time has been measured both in the sticking and in the slipping working conditions of the UPDs.

- When the damper is stuck between the platforms, the relationship between contact force and displacement is linear. As a result, the computational time required by the numerical code to calculate the forced response is reduced with respect to a general nonlinear working condition. The measurement has been carried out for the frequency range [160;140] with a unit step of 0.05Hz, i.e. 401 discrete points have been calculated (see Figure 56). Before the introduction of the analytical Jacobian matrices, the average time required for the previously described operation was more than 12 hours. On the contrary, the optimized version of the numerical code requires only 1500 seconds, i.e. 25 minutes.

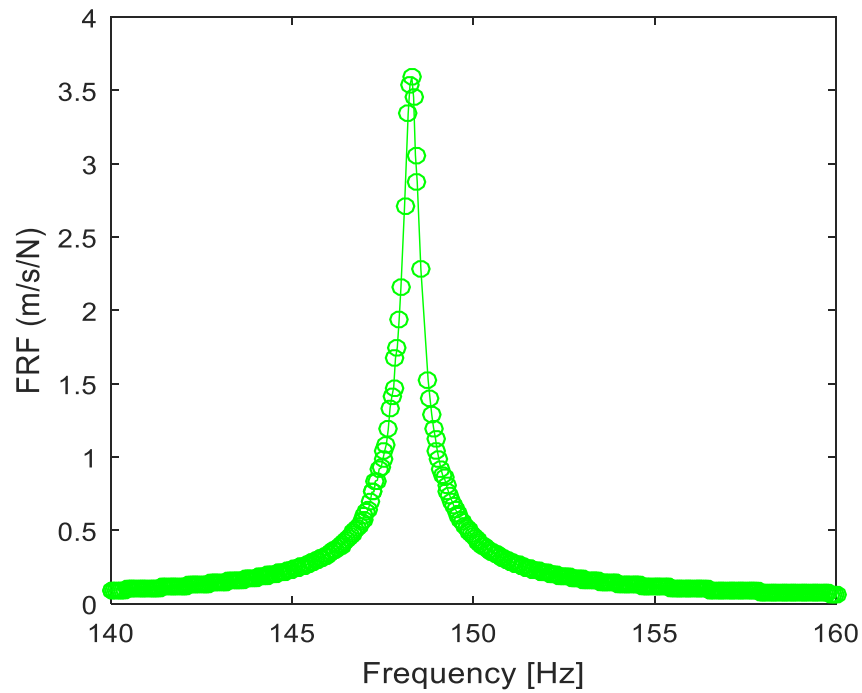


Figure 56. FRF in the sticking condition calculated with the analytical Jacobian matrices, ND=2.

- When a general nonlinear case is analyzed, the computational time required to calculate the nonlinear forced response of the bladed disk is definitely higher. By keeping the same frequency step and interval as the previous case, it can be noticed that with the introduction of the analytical Jacobian matrices, the original computational time of around 36 hours was reduced to 6000 seconds, i.e. 1 hour and 40 minutes.

15 COMPARISON BETWEEN NUMERICAL AND EXPERIMENTAL RESULTS

15.1 Validation of the Octopus numerical code

Before performing the calculation of the numerical nonlinear forced response of the bladed disk it is important to summarize the two fundamental improvements made on the *Octopus* numerical code:

- Extraction of the mass and stiffness matrices of the bladed disk in cyclic symmetry for each nodal diameter.
- Analytical calculation of the Jacobian matrices for both the underplatform damper and the bladed disk.

The optimization of the computational time made it reasonable to choose a frequency step of the order of 10^{-2} Hz, i.e. to obtain a well-defined and precise nonlinear FRF. In the following figures, the numerical results are compared with the envelope of the maximum mobility values of the 24 blades at each frequency. It has already been explained in Section 2.5 that the number of experimental envelopes is two (see blue and red lines) because two different measurements were performed in order to analyze the repeatability of the results.

The numerical FRFs have been calculated for different values of the excitation force in case of $ND = 2$ (see Figure 57, Figure 58, Figure 59 and Figure 60).

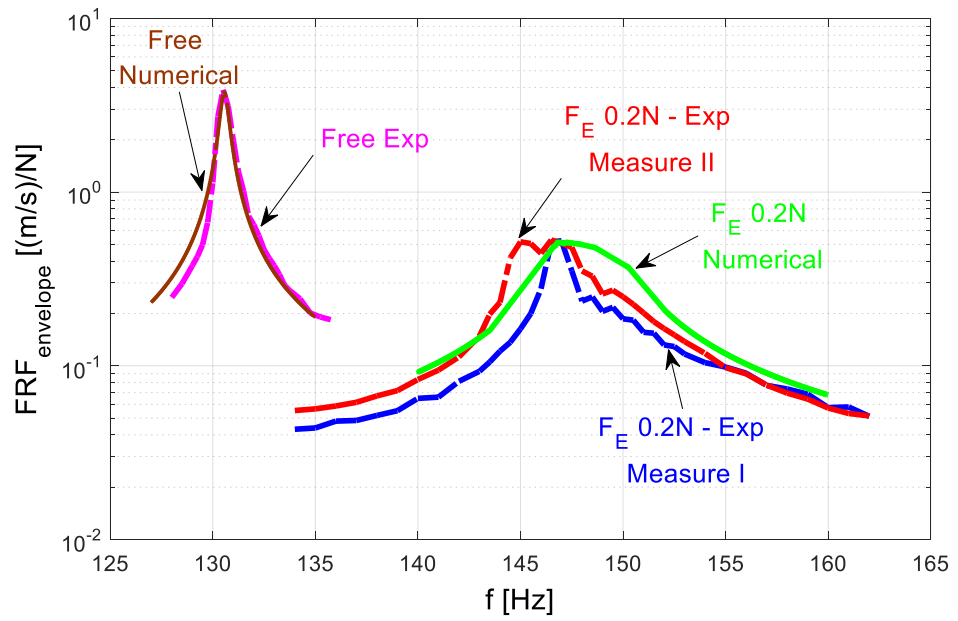


Figure 57. Comparison between experimental and numerical FRFs;

$$ND = 2, F_E = 0.2N, F_{centr} = 15kg.$$

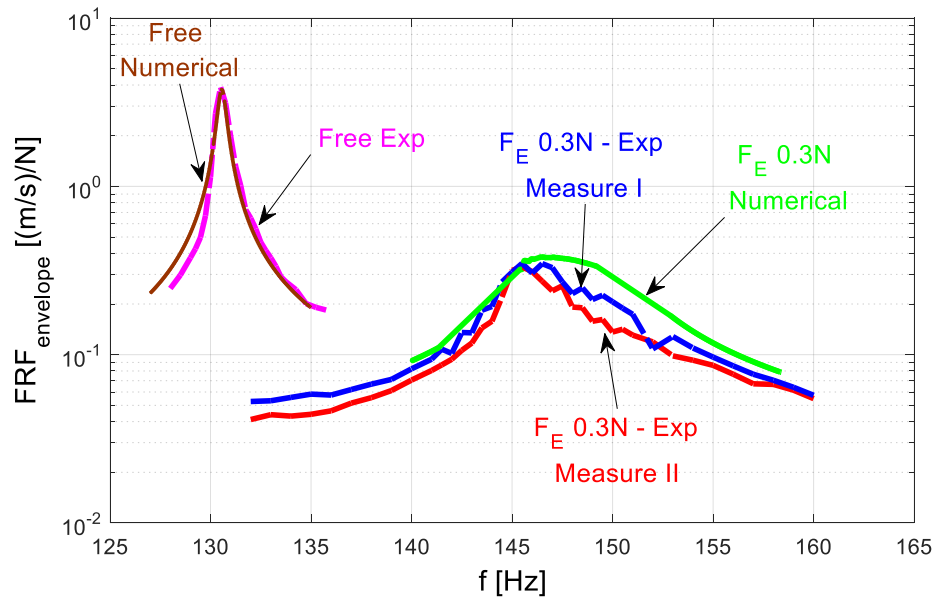


Figure 58. Comparison between experimental and numerical FRFs;

$$ND = 2, F_E = 0.3N, F_{centr} = 15kg.$$

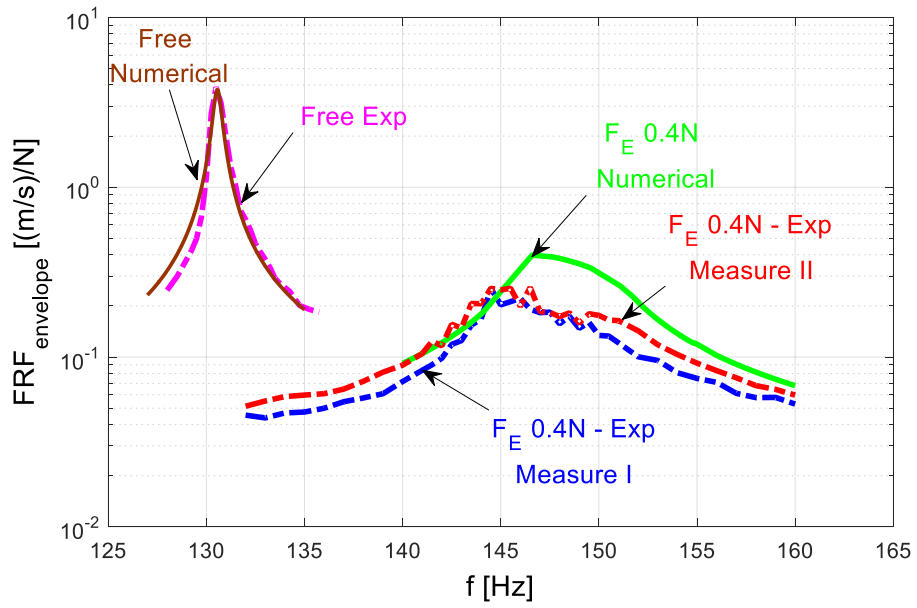


Figure 59. Comparison between experimental and numerical FRFs;
 $ND = 2, F_E = 0.4N, F_{centr} = 15kg.$

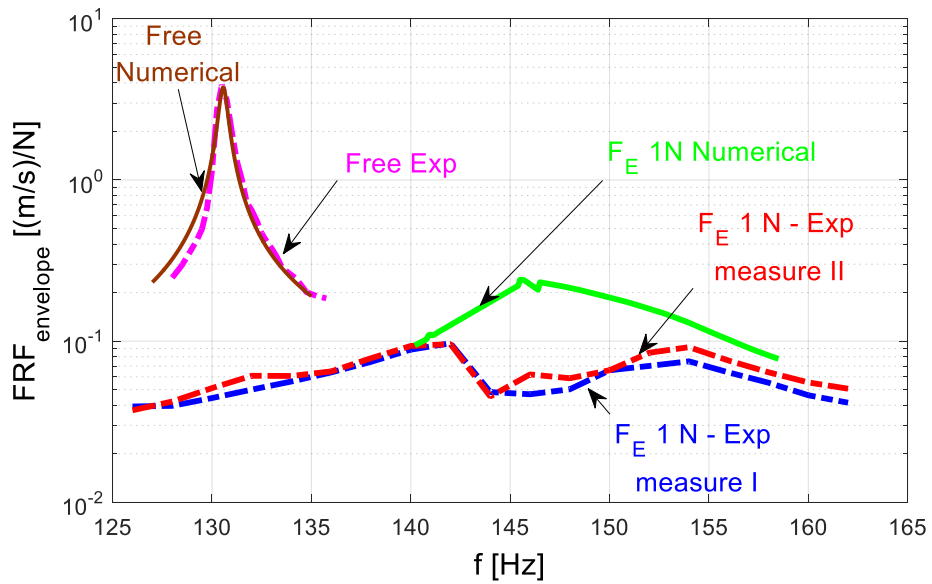


Figure 60. Comparison between experimental and numerical FRFs;
 $ND = 2, F_E = 1N, F_{centr} = 15kg.$

Finally, the numerical FRFs are plotted in the same graph in Figure 61.

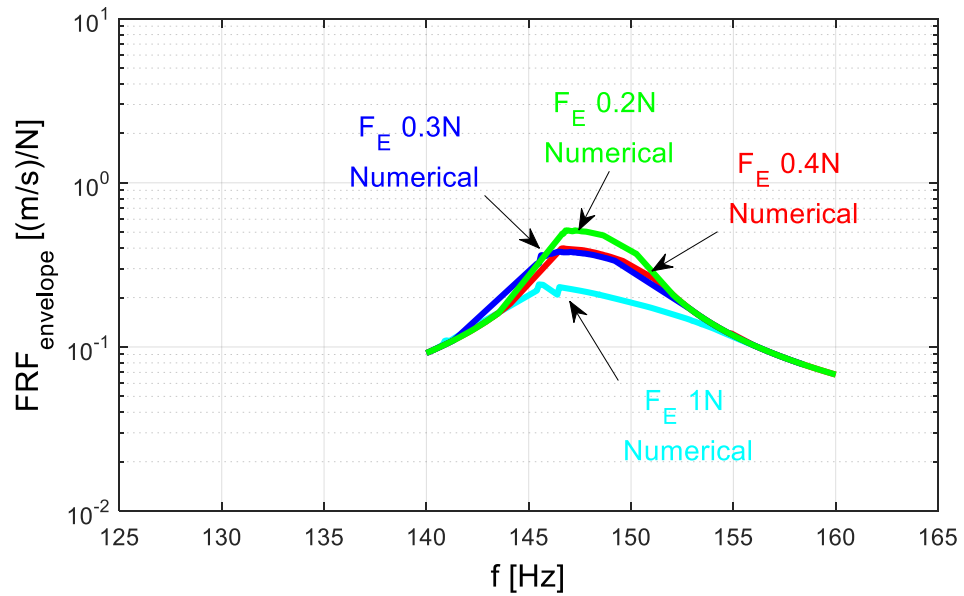


Figure 61. Comparison between numerical FRFs.

The values of the numerical natural frequencies match with the experimental ones because the FE model of the disk in Ansys was properly tuned, as described in Section 5.2.

The value of the normal contact stiffness k_n has been calculated analytically as shown in Chapter 12

$$k_n = 5.21 \cdot 10^5 \frac{N}{mm} \quad (15.1.1)$$

Moreover, the value of normal contact stiffness at each contact point was then obtained by dividing k_n by the number of contact nodes.

$$(k_n)_p = \frac{k_n}{N_{cp}} \quad (15.1.2)$$

where N_{cp} is the number of contact points on one blade platform.

The value of the tangential contact stiffness k_t was calculated performing a tuning operation of the numerical stick FRF with respect to the experimental one ($F_{ext} = 0.1N$).

$$k_t = 1.17 \cdot 10^5 \frac{N}{mm} \quad (15.1.3)$$

The modal damping was evaluated through the *Half-Power Bandwidth Method* (see Appendix A).

As a result of the comparison between numerical and experimental FRFs, it is evident that they match with good approximation. In particular, as shown in Figure 59 and in Figure 60, it can happen that the numerical FRF is located slightly above the experimental one: in this case the result is still acceptable because the numerical code identifies a conservative solution (with higher vibrational amplitude). Therefore the numerical code has been validated.

16 CONCLUSION

16.1 Concluding remarks

The starting point of this thesis was a first version of a numerical code, developed on MATLAB at Politecnico di Torino, for the calculation of the forced response of the *Octopus* bladed disk equipped with cylindrical underplatform dampers.

Given that the numerical code is aimed at the design of underplatform dampers, three requirements had to be satisfied:

- 1) In order to examine the whole dynamic of the bladed disk, a procedure able to extract the mass and stiffness matrices of the disk FE model in cyclic symmetry had to be applied in Ansys.
- 2) During the design stage, it is necessary to run the numerical code many times in order to identify both the best contact condition and the optimum mass value of the UPD. For this reason, the code had to be upgraded in order to calculate the forced response in a reasonable computational time.
- 3) The numerical code had to be validated by comparing numerical and experimental results.

The main contributions of this thesis can be summarized as follows:

- 1) The new reduction procedure performed in Ansys, allowed to take into account the whole disk dynamic: the numerical natural frequencies calculated on MATLAB for each nodal diameter were in accordance with the ones of the tuned FE model of the blisk.
- 2) The analytical calculation of the Jacobian matrices for both the blades and the UPDs allowed to achieve a noticeable reduction of the computational time. In particular, for the calculation of one FRF in the sticking condition the average computational time decreased from 12 hours, to only 1500 seconds (25 minutes). In case of the calculation of a FRF corresponding to a general nonlinear working condition, the computational time decreased from 36 hours to 6000 seconds (1 hour and 40 minutes).
- 3) The numerical code was validated by comparing some numerical results with already existing experimental data obtained in 2011 at the LAQ AERMEC laboratory of *Politecnico di Torino*.

The main limitation of the *Octopus* numerical code is represented by the set of contact parameters required as input, i.e. the values of normal and tangential contact stiffnesses, the friction coefficients and the structural damping of the disk. The values

of these contact parameters must be determined experimentally through purposely designed test rigs.

As a result of the optimizations performed, the *Octopus* numerical code represents at the moment a powerful tool for the design of underplatform dampers.

APPENDICES

Appendix A

THE HALF-POWER BANDWIDTH METHOD

In order to estimate the structural damping of a given structure, the starting point is the FRF of the system (see Figure 62). At first, the amplitude corresponding to the resonance condition A is divided by $\sqrt{2}$, then the identified interval $[f_1; f_2]$ is divided by the value of the natural frequency f doubled.

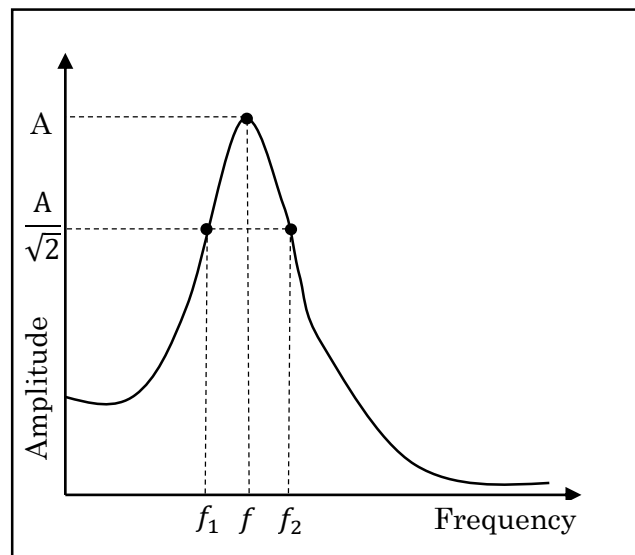


Figure 62. Application of the half power bandwidth method.

The value of the structural damping ζ is

$$\zeta = \frac{f_1 - f_2}{2f}$$

Appendix B

PARAMETERS USED IN THE FUNCTION EQUILIBRIUM_DAMPER_J

- $q0_tn = \begin{bmatrix} t_{D,1}^0 & \dots & \dots & \dots & t_{D,ncp}^0 \\ n_{D,1}^0 & \dots & \dots & \dots & n_{D,ncp}^0 \\ w_{D,1}^0 & \dots & \dots & \dots & w_{D,ncp}^0 \end{bmatrix}$

This matrix has dimension $(3 \times ncp)$, where ncp is the number of contact points at the right or left contact line. Its components are the zero-order harmonics of the local displacements of the damper at each contact point.

- $q_tn = \begin{bmatrix} t_{D,1}^1 & \dots & \dots & \dots & t_{D,ncp}^1 \\ n_{D,1}^1 & \dots & \dots & \dots & n_{D,ncp}^1 \\ w_{D,1}^1 & \dots & \dots & \dots & w_{D,ncp}^1 \\ \dots & \dots & \dots & \dots & \dots \\ \dots & \dots & \dots & \dots & \dots \\ \dots & \dots & \dots & \dots & \dots \\ t_{D,1}^{Nh} & \dots & \dots & \dots & t_{D,ncp}^{Nh} \\ n_{D,1}^{Nh} & \dots & \dots & \dots & n_{D,ncp}^{Nh} \\ w_{D,1}^{Nh} & \dots & \dots & \dots & w_{D,ncp}^{Nh} \end{bmatrix}$

This matrix has dimension $(3 \times Nh \times ncp)$, where Nh is the number of harmonics, ncp is the number of contact points at the right or left contact line. Its components are the harmonics from order 1 to Nh of the local displacements of the damper at each contact point.

Appendix B (continued)

$$\bullet \quad MD_{tl} = \begin{bmatrix} t_{D,1}^0 & \dots & \dots & \dots & t_{D,ncp}^0 \\ t_{D,1}^1 & \dots & \dots & \dots & t_{D,ncp}^1 \\ \dots & \dots & \dots & \dots & \dots \\ \dots & \dots & \dots & \dots & \dots \\ \dots & \dots & \dots & \dots & \dots \\ t_{D,1}^{Nh} & \dots & \dots & \dots & t_{D,ncp}^{Nh} \end{bmatrix}$$

This matrix has dimension $((Nh+1) \times ncp)$, where Nh is the number of harmonics, ncp is the number of contact points at the right or left contact line. Its components are the harmonics from order 0 to Nh of the tangential local displacements of the damper at each contact point. Matrices MD_{nl} and MD_{wl} have the same structure.

$$\bullet \quad uLstar = \begin{bmatrix} t_{P,1}^1 & \dots & \dots & \dots & t_{P,ncp}^1 \\ n_{P,1}^1 & \dots & \dots & \dots & n_{P,ncp}^1 \\ w_{P,1}^1 & \dots & \dots & \dots & w_{P,ncp}^1 \end{bmatrix}$$

This matrix has dimension $(3 \times ncp)$, where ncp is the number of contact points at the right or left contact line. Its components are the harmonics of order 1 of the tangential local displacements of the platform at each contact point. Matrix $uRstar$ has the same structure.

Appendix B (continued)

$$\bullet \quad Utl = \begin{bmatrix} t_{D,1}^0 & \dots & \dots & \dots & t_{D,ncp}^0 \\ t_{D,1}^1 - t_{P,1}^1 & \dots & \dots & \dots & t_{D,ncp}^1 - t_{P,ncp}^1 \\ t_{D,1}^2 & \dots & \dots & \dots & t_{D,ncp}^2 \\ \dots & \dots & \dots & \dots & \dots \\ t_{D,1}^{Nh} & \dots & \dots & \dots & t_{D,ncp}^{Nh} \end{bmatrix}$$

This matrix has dimension $((Nh+1) \times ncp)$, where ncp is the number of contact points at the left contact line. Its components are the differences between damper and platform displacements for each harmonic order at each contact point. Matrices Vl , Uwl , Utr , Vr , Uwr have the same structure.

$$\bullet \quad Tl = \begin{bmatrix} T_1^0 & \dots & \dots & \dots & T_{ncp}^0 \\ T_1^1 & \dots & \dots & \dots & T_{ncp1}^1 \\ \dots & \dots & \dots & \dots & \dots \\ \dots & \dots & \dots & \dots & \dots \\ T_1^{Nh} & \dots & \dots & \dots & T_{ncp}^{Nh} \end{bmatrix}$$

This matrix has dimension $((Nh+1) \times ncp)$, where ncp is the number of contact points at the left contact line. Its components are the tangential friction forces for each harmonic order developed at each left contact point. Matrices Nl , Wl , Tr , Nr , Wr have the same structure.

Appendix B (continued)

$$\bullet \quad FattL = \begin{bmatrix} T_1^0 & \dots & \dots & \dots & T_{ncp}^0 \\ N_1^0 & \dots & \dots & \dots & N_{ncp}^0 \\ W_1^0 & \dots & \dots & \dots & W_{ncp}^0 \\ \dots & \dots & \dots & \dots & \dots \\ \dots & \dots & \dots & \dots & \dots \\ T_1^{Nh} & \dots & \dots & \dots & T_{ncp}^{Nh} \\ N_1^{Nh} & \dots & \dots & \dots & N_{ncp}^{Nh} \\ W_1^{Nh} & \dots & \dots & \dots & W_{ncp}^{Nh} \end{bmatrix}$$

This matrix has dimension $(3^*(Nh+1) \times ncp)$, where ncp is the number of contact points at the left contact line. Its components are the friction forces for each harmonic order developed at each left contact point. Matrix $FattR$ has the same structure.

Appendix C

CORRESPONDENCE BETWEEN VARIABLES NAME IN THE THESIS AND IN THE NUMERICAL CODE

The left-hand side of each equation represents a parameter as it is named in this thesis, the right-hand side shows the correspondent name used in the numerical code.

- $\frac{\delta T}{\delta(t^* - t_D)} = dfnl_du_L \text{ or } dfnl_du_R$

- $t^* = uLstar \text{ or } uRstar$

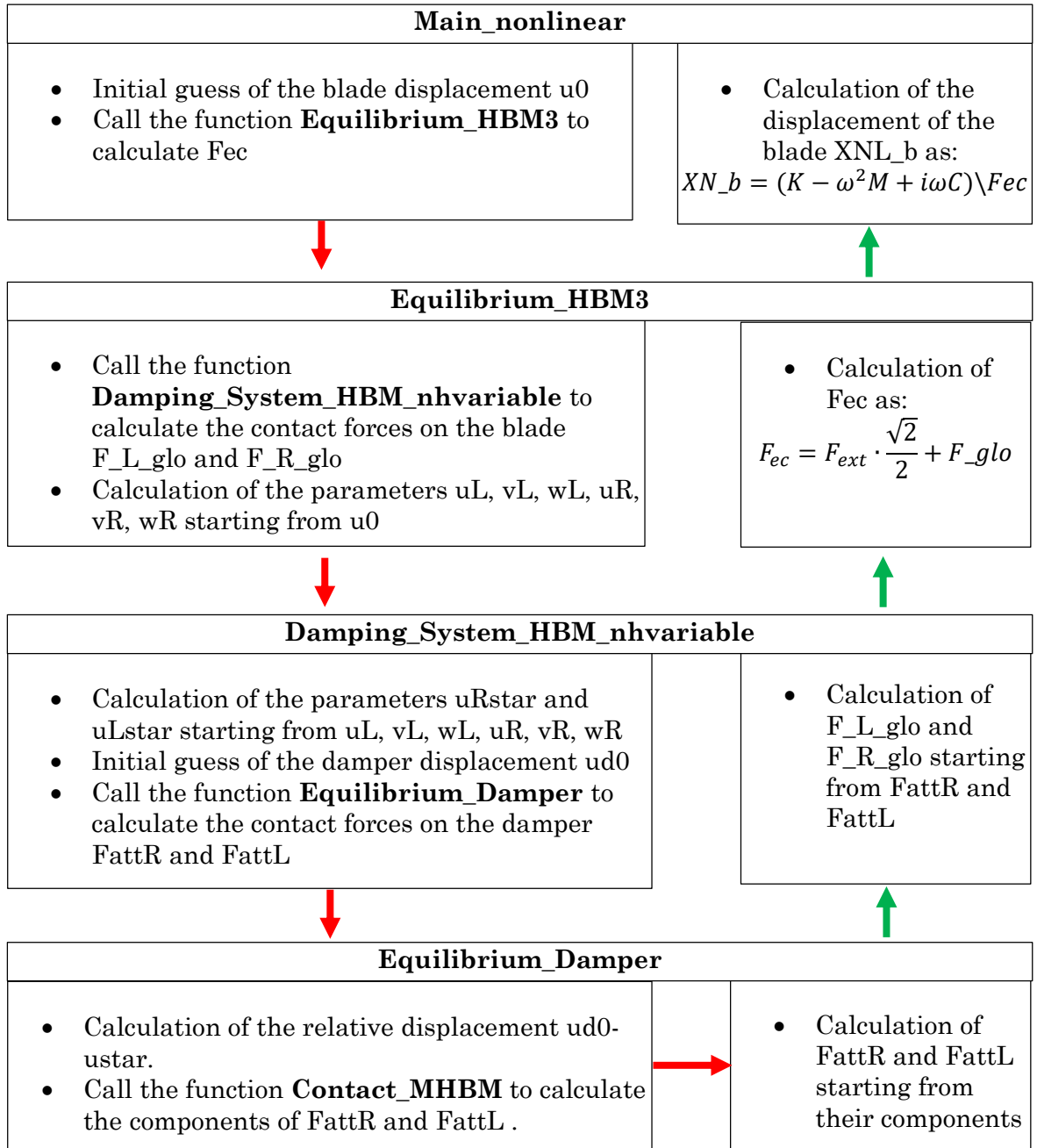
- $t_D = q0_tn \text{ and } q_tn$

- $F_E = F_{ext}$

- $F_{centr} = F_c$

Appendix D

ALGORITHM FOR THE CALCULATION OF THE BLADE FORCED RESPONSE



CITED LITERATURE

- ANSYS Mechanical APDL Theory Reference, ANSYS Inc.; 594-596, 765: 2013
- Baraa, A.S., Chatelet, E., Baguet, S., Jacquet-Richardet, G.: Dissipated energy and boundary condition effects associated to dry friction on the dynamics of vibrating structures. *Mechanism and Machine Theory* 46; 479-491:2011
- Berruti, T., Firrone, C.M., Gola, M.M.: A Test Rig for Noncontact Traveling Wave Excitation of a Bladed Disk With Underplatform Dampers. *Journal of Engineering for Gas Turbines and Power* 133; 1-7: 2011
- Berruti, T.: A test rig for the investigation of the dynamic response of a bladed disk with underplatform dampers. *Mechanics Research Communications* 37; 582:2010
- Berruti T., Goglio, L., Filippi, S., Gola, M.M.: A Test Rig for Frictionally Damped Bladed Segments. *Journal of Engineering for Gas Turbines and Power* 124; 388-394: 2002
- Berruti, T., Gola, M.M., Zucca, S.: Underplatform Damper Performance with Turbine Blades. *Proceedings of NATO AVT-121 Symposium on Evaluation, Control and Prevention of High Cycle Fatigue in Gas Turbine Engines*; October 3-7, 2005
- Borrajo, J.M., Zucca, S., Gola, M.M.: Analytical formulation of the Jacobian matrix for non-linear calculation of the forced response of turbine blade assemblies with wedge friction dampers. *Journal of Nonlinear Mechanics* 41; 1118-1127: 2006
- Brändlein, J.: Ball and Roller Bearings: Theory, Design, and Application. West Sussex, John Wiley & Sons, 1999.
- Cardona, A., Coune, T., Lerusse, A.: A multi-harmonic method for nonlinear vibration analysis. *International Journal for numerical methods in engineering* 37; 1593-1608: 1994
- Castanier, M.P., Pierre, C.: Modeling and Analysis of Mistuned Bladed Disk Vibration: Status and Emerging Directions. *Journal of Propulsion and Power* 22; 385: 2006
- Cigeroglu, E., An, N., Menq, C-H.: Forced Response Prediction of Constrained and Unconstrained Structures Coupled Through Frictional Contacts. *Journal of Engineering for Gas Turbines and Power* 131; 22505: 2009
- Firrone, C.M., Zucca, S.: Modeling Friction Contacts in Structural Dynamics and its Application to Turbine Bladed Disks. *Numerical Analysis – Theory and Application* 14; 301-334: 2011
- Firrone, C.M., Zucca, S., Gola M.M.: The effect of underplatform dampers on the forced response of bladed disks by a coupled static/dynamic harmonic balance method, *International Journal of Non-Linear Mechanics* 46; 363-375: 2011

- Firrone, C.M., Berruti, T.: Non Contact Measurement System with Electromagnets for Vibration Tests on Bladed Disks. *Applied Measurement Systems* 5; 78-80-82:2012
- Firrone, C.M., Berruti, T.M., Gola, M.M.: On Force Control of an Engine Order-Type Excitation Applied to a bladed disk with underplatform dampers. *Journal of Vibration and Acoustics* 135; 041103: 2013
- Harris, T.: Rolling Bearing analysis. New York, John Wiley & Sons, 1991.
- Hassan, M.: Vibratory Analysis of Turbomachinery Blades. Master's thesis, Rensselaer Polytechnic Institute, Hartford, 2008
- Jaiswal, B.L., Bhawe, S.K.: Experimental Evaluation of Damping in a Bladed Disk Model. *Journal of Sound and Vibration* 177; 111-120:1994
- Jin-Gyun, K., Phill-Seung, L.: An enhanced Craig-Bampton method. *International Journal for numerical methods in engineering* 103; 79-93: 2014
- Jones, K.W., Cross, C.J.: Travelling Wave Excitation System for Bladed Disks. *Journal of propulsion and power* 19; 135-141: 2003
- Koh, K-H., Griffin, J.H.: Dynamic Behavior of Spherical Friction Dampers and its Implication to Damper Contact Stiffness. *Journal of Engineering for Gas Turbines and Power* 129; 511-521: 2007
- Orlov, P.: Fundamentals of Machine Design. Moscow, Mir, 1977/1980.
- Orris, R., Petyt., M.: A finite element study of harmonic wave propagation in periodic structures. *Journal of Sound and Vibration* 33; 223-236: 1974
- Panning, L., Popp, K., Sextro, W., Gotting, F., Kayser, A., Wolter, I.: Asymmetrical Underplatform Dampers in Gas Turbine Bladings: Theory and Application. *In proceedings of ASME Turbo Expo* 6; 269-280: 2004
- Petrov, E. P., Ewins, D. J.: Analytical Formulation of Friction Interface Elements for Analysis on Nonlinear Multi-Harmonic Vibrations of Bladed Disks. *Journal of Turbomachinery*;125; 364-371:2003
- Petrov, E.P., Ewins, D.J.: Advanced Modeling of Underplatform Friction Dampers for Analysis of Bladed Disk Vibration. *Journal of Turbomachinery* 129; 143-150: 2007
- Seinturier, E.: Forced response computation for bladed disks industrial practices and advanced methods. *Turbomeca (SAFRAN)*; 7:2007
- Sever, I.A., Petrov, E.P., Ewins, D.J.: Experimental and Numerical Investigation of Rotating Bladed Disk Forced Response using Underplatform Friction Dampers. *Journal of Engineering for Gas Turbines and Power* 130; 42503: 2008
- Szwedowicz, J., Visser, R., Sextro, W., Masserey, P.A.: On Nonlinear Forced Vibration of Shrouded Turbine Blades. *Journal of Turbomachinery* 130; 11002: 2008
- Thomas, D.: Standing waves in rotationally periodic structures. *Journal of Sound and Vibration* 37; 288-290: 1974

- Thomas, D.: Dynamic of rotationally periodic structures. *Int. Journal for Numerical Methods in Engineering* 37; 81-102: 1979
- Yang, B.D., Menq, C.H.: Characterization of 3D contact kinematics and prediction of resonant response of structures having 3D frictional constraint. *Journal of Sound and Vibration* 217; 909-925:1998
- Zucca, S., Borrajo, J., Gola, M.M.: Forced Response of Bladed Disks in Cyclic Symmetry with Underplatform Dampers. *ASME Turbo Expo 2006: Power for Land, Sea and Air* 5; 921-929: 2006
- Zucca, S., Firrone, C.M., Gola, M.M.: Modeling underplatform dampers for turbine blades: a refined approach in the frequency domain. *Journal of Vibration and Control* 19; 1087-1102: 2012

VITA

- NAME: Emanuele Grossi
- EDUCATION: M.S., Mechanical Engineering, University of Illinois at Chicago, Illinois, USA, 2014-2016.
- Honors College student at Alta Scuola Politecnica, Polytechnic of Turin and Polytechnic of Milan, Turin, Milan, Italy, 2014-2016.
- B.S., Mechanical Engineering, Polytechnic of Turin, Turin, Italy, 2011-2014, Full marks with honour.
- Honors College student at Collegio Carlo Alberto, Polytechnic of Turin and University of Turin, Turin, Italy, 2011-2013.
- HONORS: Graduate College Scholarship, Polytechnic of Turin, Turin, Italy, 2015
- Italian Finalist of the International Championship of Mathematical Games, Bocconi University, Milan, Italy, 2011
- Honorable Mention at the Italian Mathematics Olympics, Cesenatico, Italy, 2011